Microscope
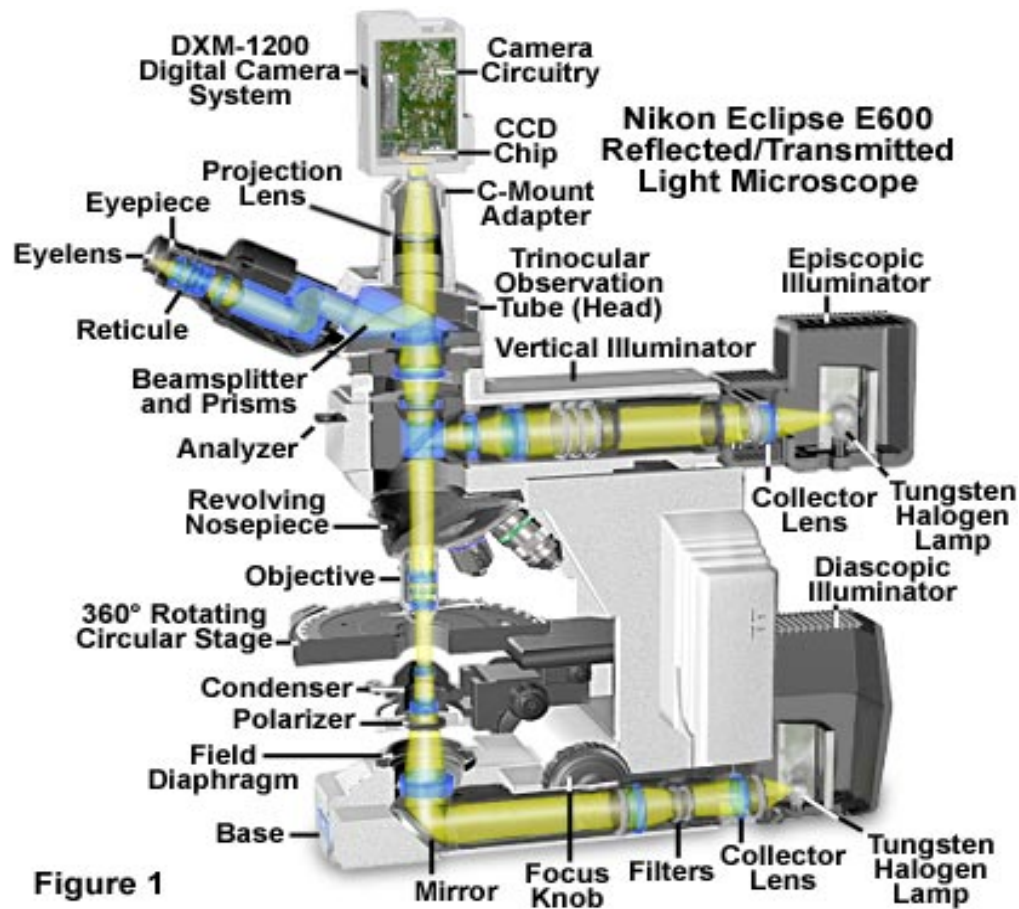

Figure 1

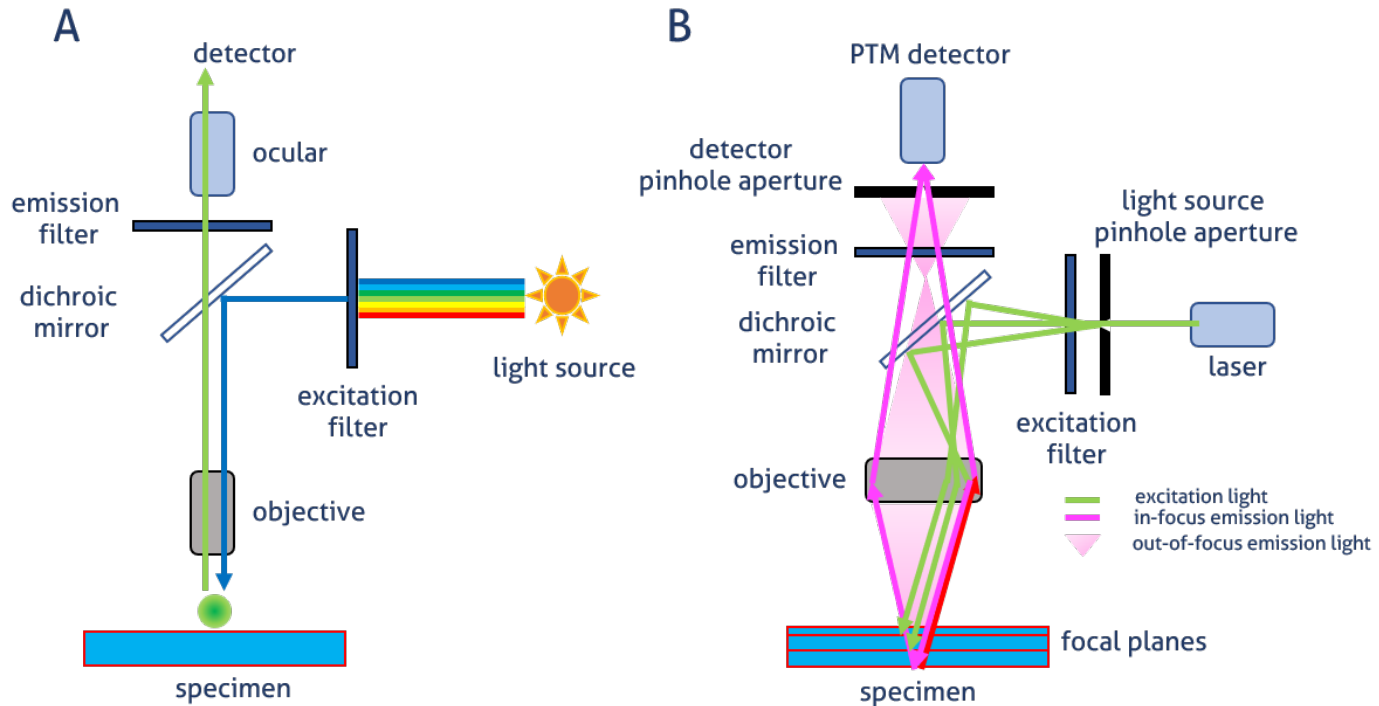Nikon Eclipse E600 Reflected/Transmitted Light Microscope

Diffraction Limit

$$d = \lambda/(2n \sin \alpha)$$

$$, k_0 = 2NA/\lambda_{em}$$
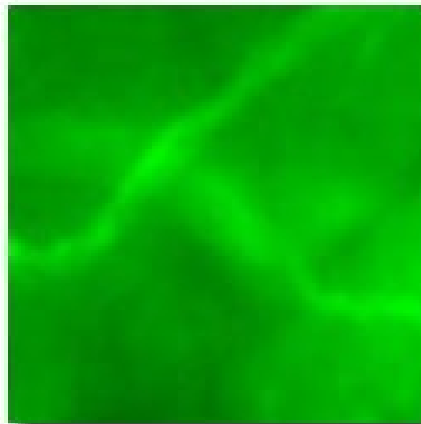

Intensity Distributions
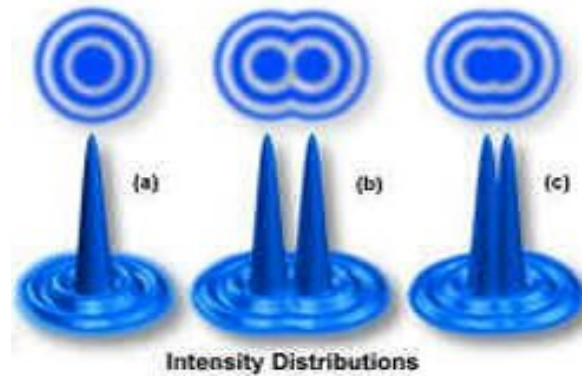
Confocal vs Wide Field

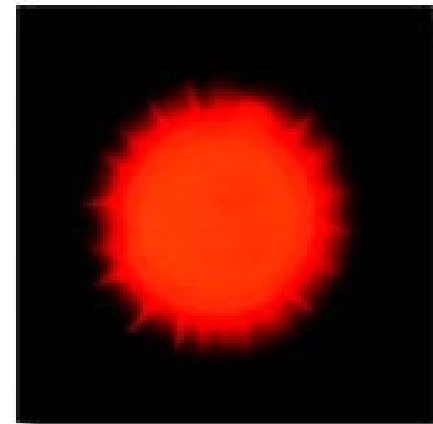# Confocal vs Wide Field

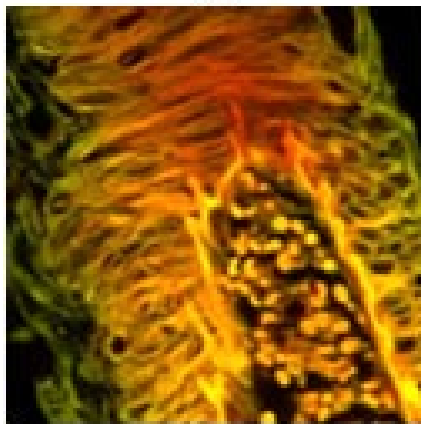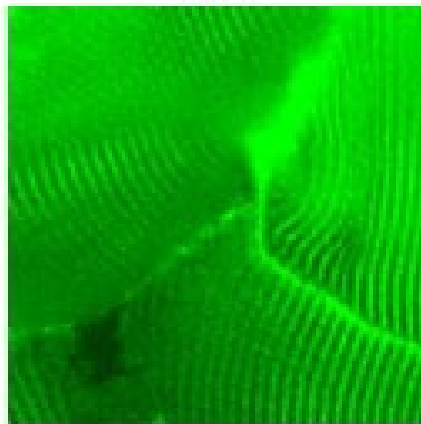Confocal and Widefield Fluorescence Microscopy

(a)   (b)   (c)
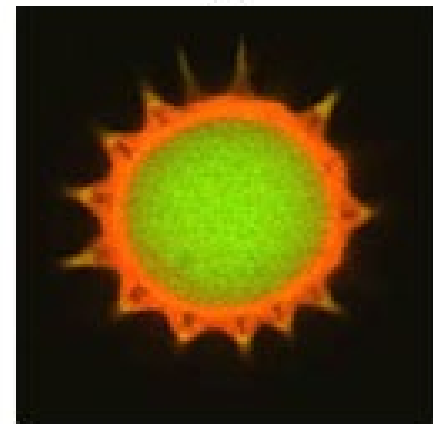
(d)   (e)   (f)

Figure 1

The Nobel Prize in Chemistry 2014

Photo: Matt Staley/HHMI

Eric Betzig

Prize share: 1/3

Photo: Wikimedia Commons, CC-BY-SA-3.0

Stefan W. Hell

Prize share: 1/3

Photo: K. Lowder via Wikimedia Commons, CC-BY-SA-3.0

William E. Moerner

Prize share: 1/3

Super-Resolution Microscopy
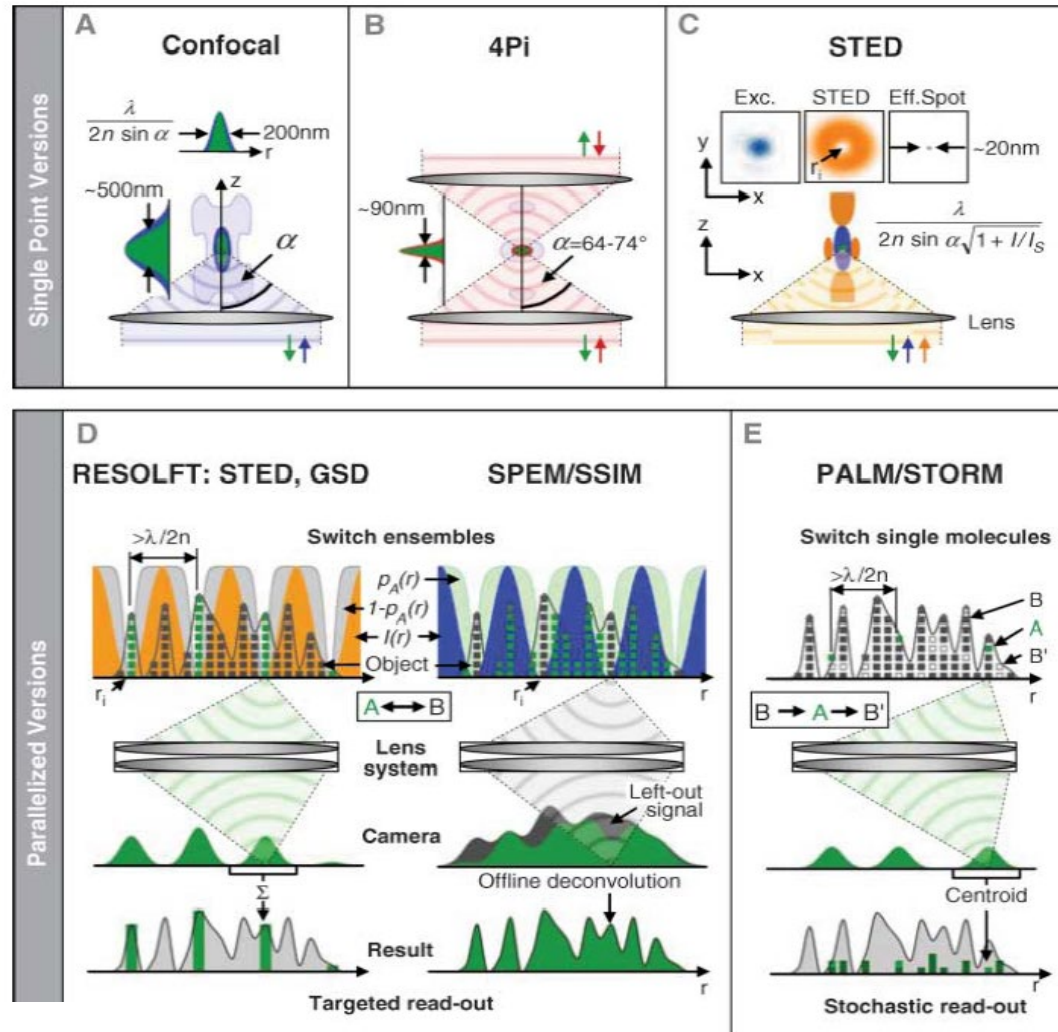
Localization

$$I(x, y) = I_{\text{background}} + A.$$

$$\exp\left\{-{}^1\!/_2\left[\left(\frac{x - x_0}{s_x}\right)^2 + \left(\frac{y - y_0}{s_y}\right)^2\right]\right\},$$

$$\sigma^\mu_{x,y}$$

$$= \sqrt{\frac{s^2_{x,y}}{N_{\text{photons}}} + \frac{a^2}{12.N_{\text{photons}}} + \frac{8.\pi.s^4_{x,y}.b^2}{a^2.N_{\text{photons}}}},$$

Photoactivation localization microscopy (PALM)

Diffraction-limited system:

Lateral resolution $\Delta xy \approx 0.61\, \lambda$ / N.A.
≈ 200 nm

Axis resolution $\Delta z \approx 2\lambda$ / N.A.^{2}
≈ 450 nm

Mean-squared position error:

$$\left(\sigma_{x,y}^2\right)_m \approx \frac{s^2 + a^2/12}{N_m} + \frac{4\sqrt{\pi}\, s^3 b_m^2}{a N_m^2}$$
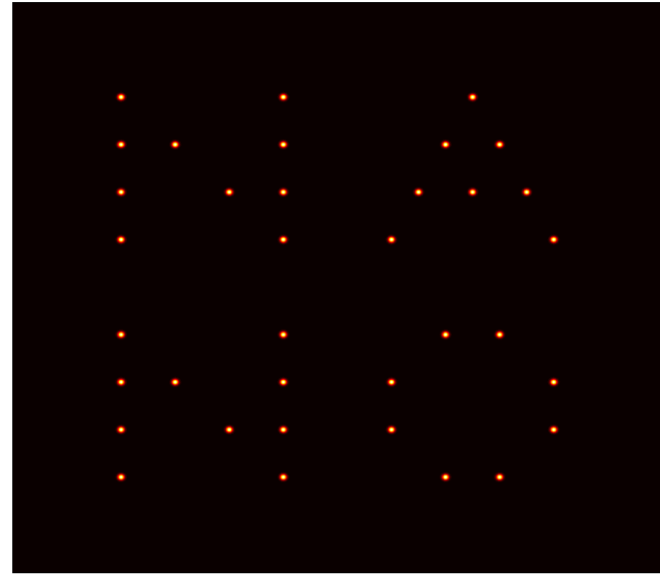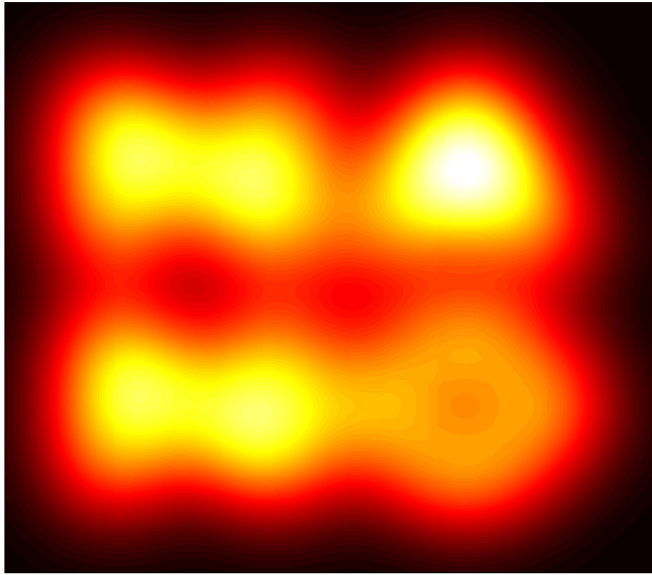
s is the standard deviation of the PSF.
a is the pixel size in the image
N_m is the total number of photons measured from molecule m
b_m is the number of background photons collected in the fitting window

Russell E. Thompson, Daniel R. Larson, and Watt W. Webb, **Biophysical Journal** 82, 2775 (2002).
Eric Betzig, et al., **Science** 313, 1642 (2006).

Imaging Intracellular Fluorescent Proteins at Nanometer Resolution
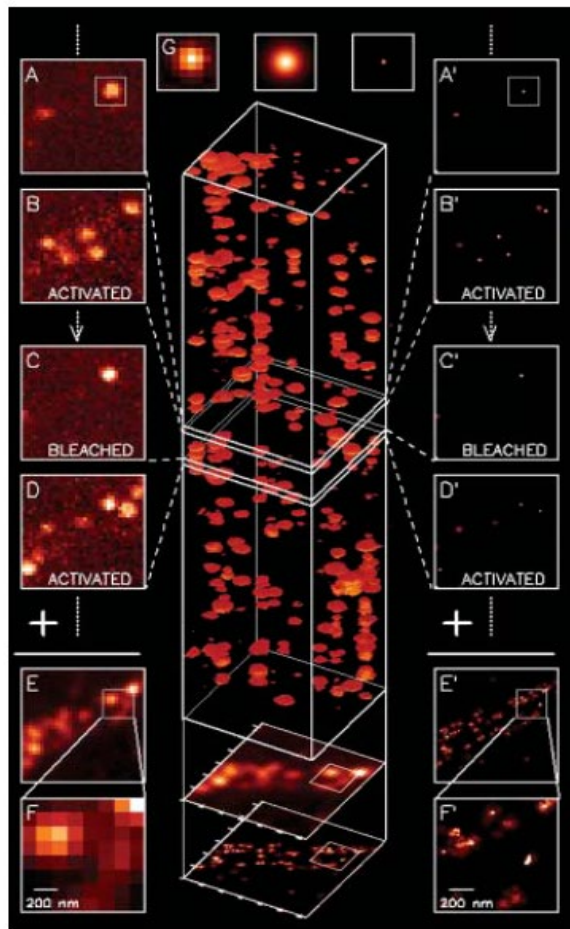
$$(\sigma_{x,y}{}^2)_m \approx \frac{s^2 + a^2/12}{N_m} + \frac{4\sqrt{\pi}\,s^3 b_m{}^2}{aN_m{}^2}$$
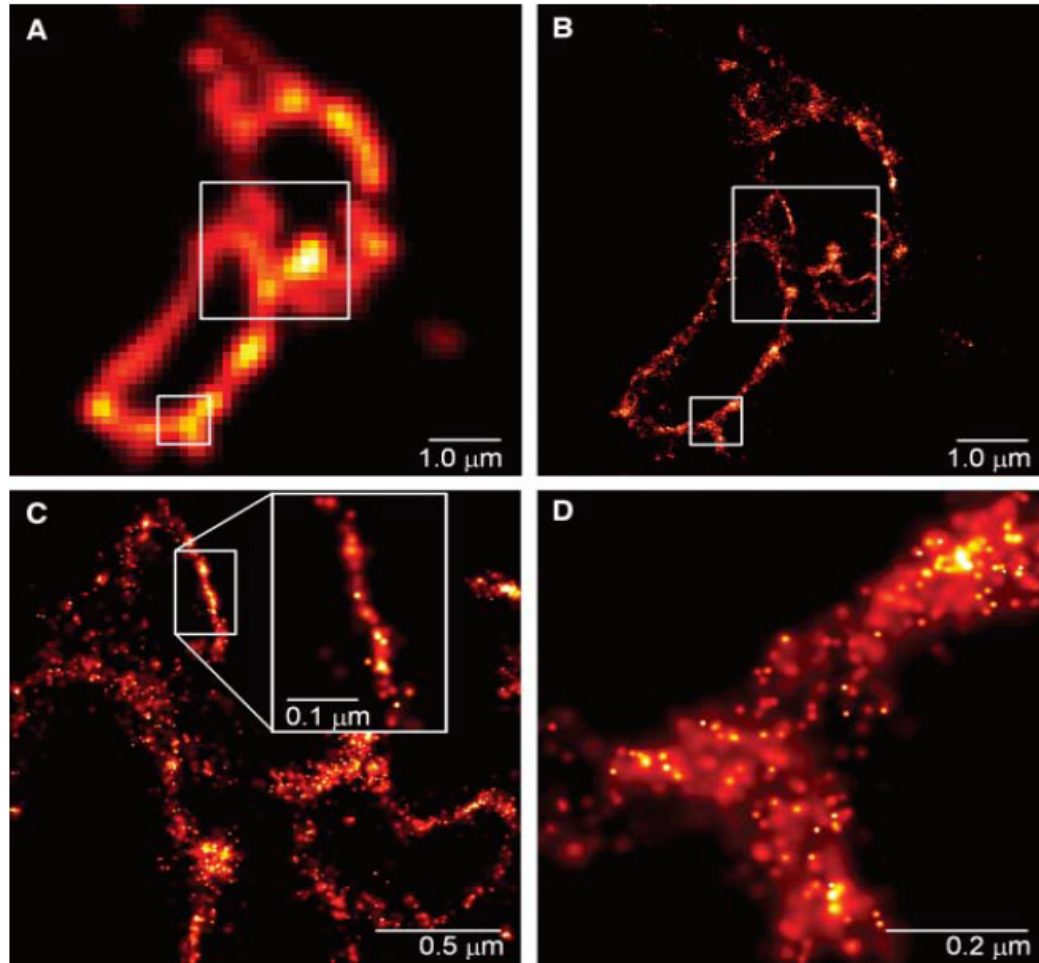
Fig. 2. Comparative summed-molecule TIRF (**A**) and PALM (**B**) images of the same region within a cryo-prepared thin section from a COS-7 cell expressing the lysosomal transmembrane protein CD63 tagged with the PA-FP Kaede. The larger boxed region in (B), when viewed at higher magnification (**C**) reveals smaller associated membranes that may represent interacting lysosomes or late endosomes that are not resolvable by TIRF. In a region where the section is nearly orthogonal to the lysosomal membrane, the most highly localized molecules fall on a line of width ~10 nm (inset). In an obliquely cut region [(**D**), from the smaller boxed region in (B)], the distribution of CD63 within the membrane plane can be discerned.
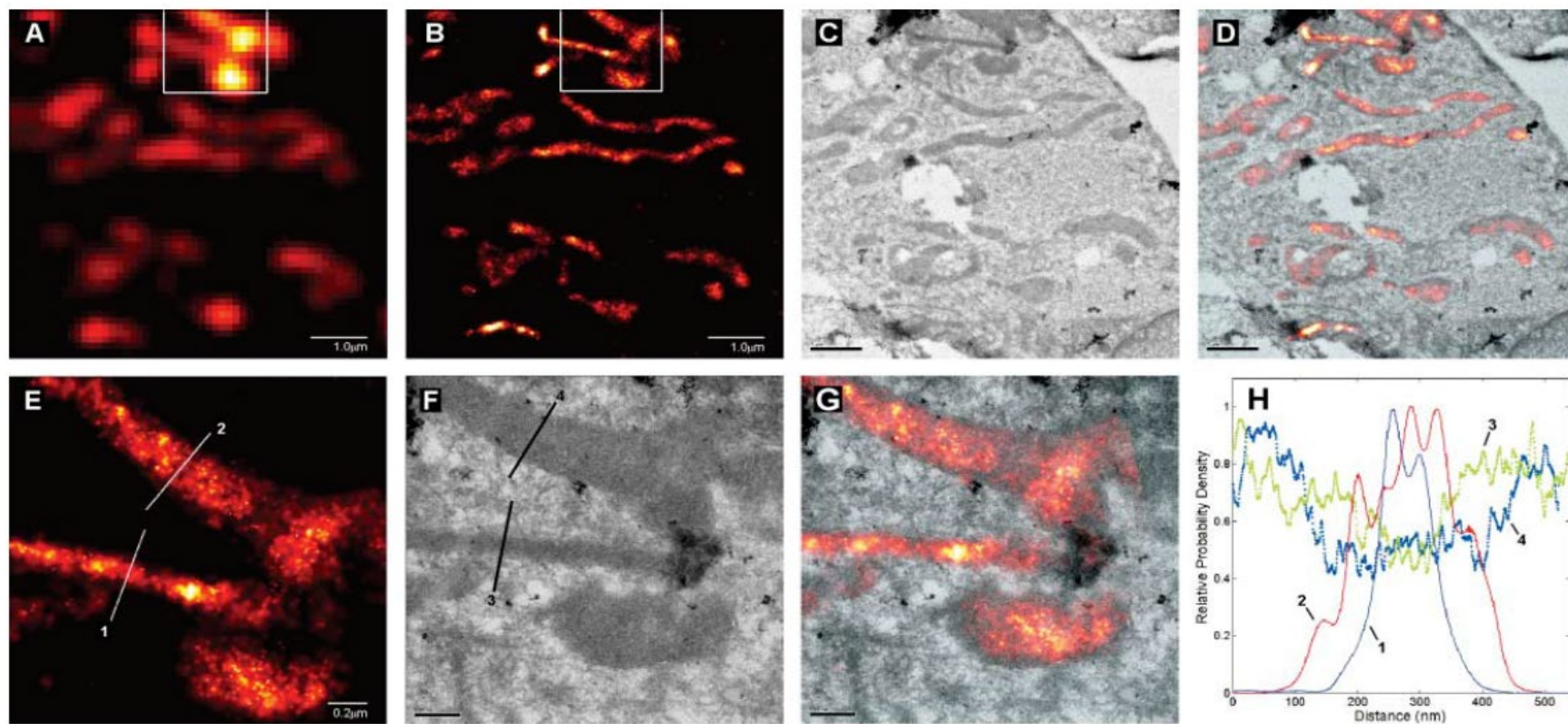
Fig. 3. Comparative summed-molecule TIRF (**A**), PALM (**B**), TEM (**C**), and PALM/TEM overlay (**D**) images of mitochondria in a cryo-prepared thin section from a COS-7 cell expressing dEosFP-tagged cytochrome-C oxidase import sequence. Higher magnification PALM (**E**), TEM (**F**), and overlay (**G**) images within the box in (B) reveal that these matrix reporter molecules extend up to, but not into, the ~20-nm outer mitochondrial membrane. The molecular distribution across two mitochondria along lines 1 and 2 in PALM image (E) are compared in (**H**) to the TEM signal along lines 3 and 4 in (F) across the same mitochondria. Scale bars: 1.0 μm in (A) to (D); 0.2 μm in (E) to (G).

Sub-diffraction-limit imaging by stochastic optical reconstruction microscopy (STORM)

Michael J Rust[1,5], Mark Bates[2,5] & Xiaowei Zhuang[1,3,4]
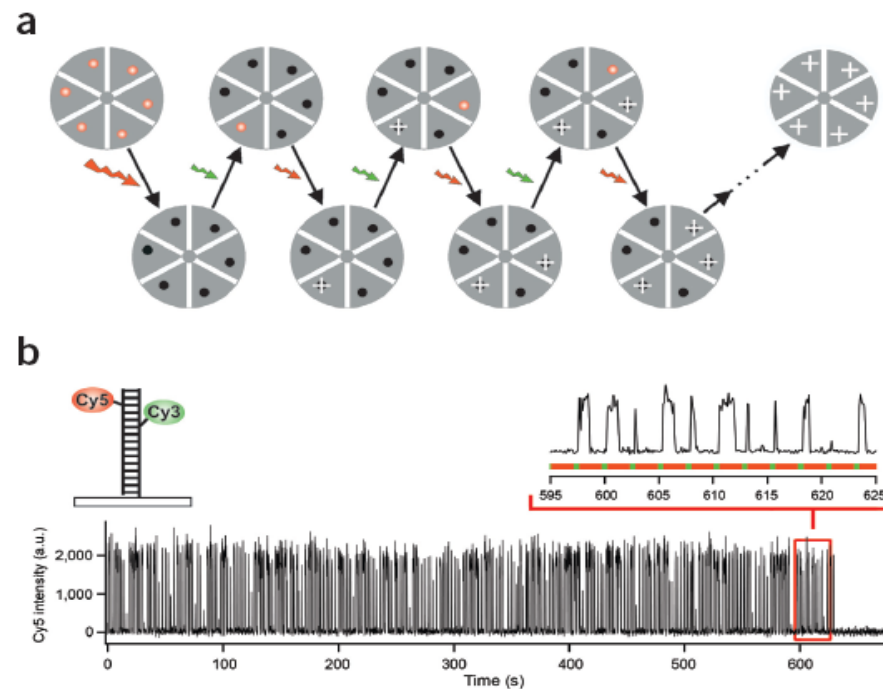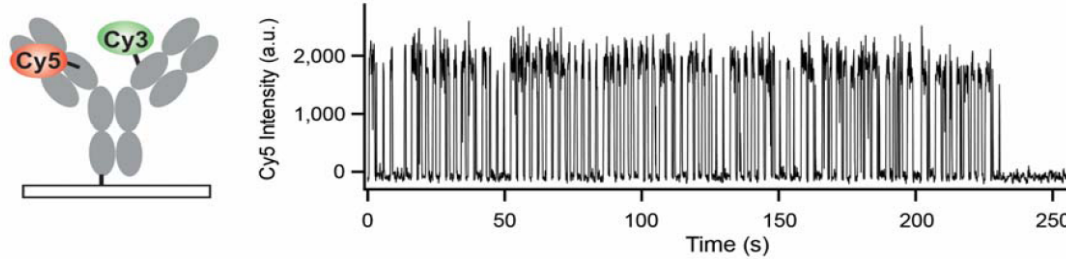
: 2.2 : 1 for Cy3 and 0.1 : 1 for Cy5

Goat anti-mouse secondary antibody labeled with the cyanine switch exhibits photoswitching behavior similar to switch-labeled DNA. The antibody was labeled with Cy3 and Cy5 (as described in **Supplementary Methods** online) and bound to a quartz slide coated with unlabeled mouse anti-transferrin primary antibody. The trace shows the Cy5 fluorescence intensity detected from a single labeled antibody as it switches on and off until permanent photobleaching occurs after 230 seconds. A red laser (633 nm, 30 W/cm^2) is used to excite fluorescence from Cy5 and to switch Cy5 to the dark state. A green laser (532 nm, 1 W/cm^2) is used to switch the Cy5 back to the fluorescent state. The sample was excited with a sequence of alternating green and red laser pulses (0.5 s green followed by 2 s red).

$$I(x, y) = A + I_0 e^{\left[-(x'/a)^2 - (y'/b)^2\right]/2}$$

$$x' = (x - x_0)\cos\theta - (y - y_0)\sin\theta$$
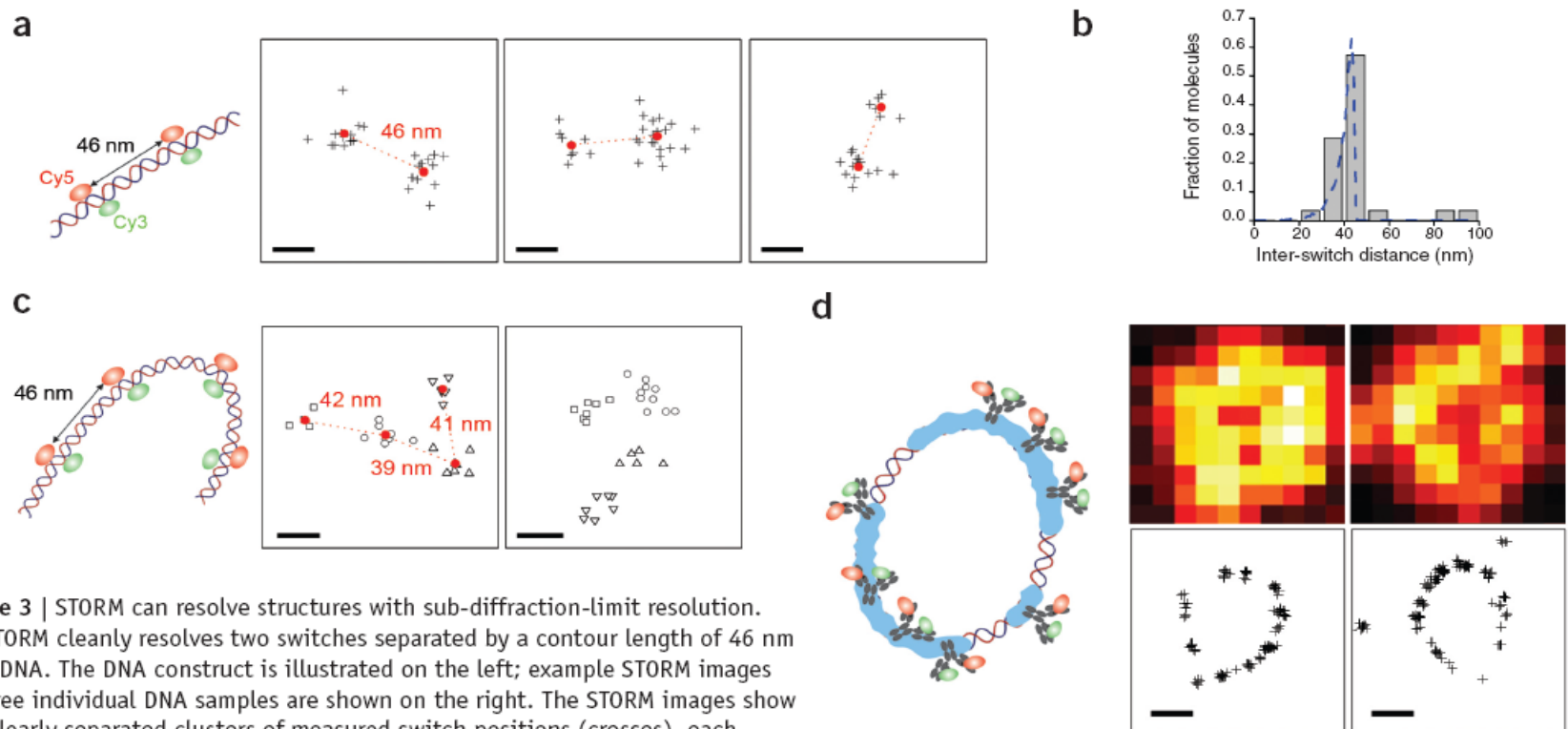$$y' = (x - x_0)\sin\theta + (y - y_0)\cos\theta$$

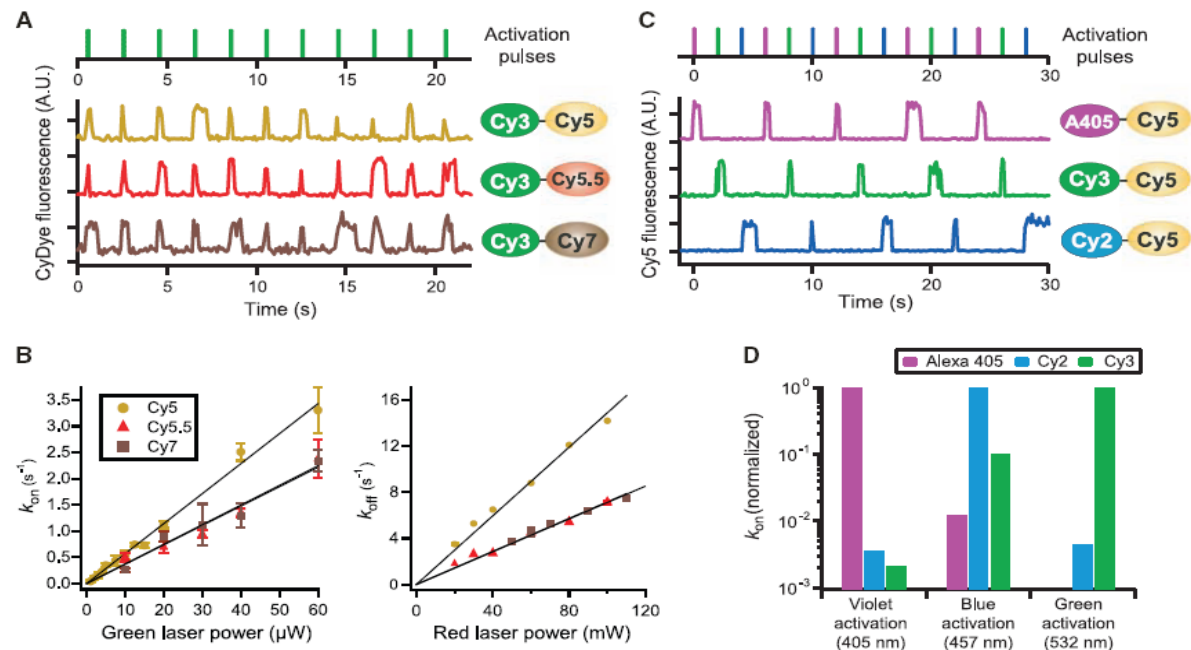**Figure 3 | STORM can resolve structures with sub-diffraction-limit resolution.**
(**a**) STORM cleanly resolves two switches separated by a contour length of 46 nm on dsDNA. The DNA construct is illustrated on the left; example STORM images of three individual DNA samples are shown on the right. The STORM images show two clearly separated clusters of measured switch positions (crosses), each corresponding to a single switch. The center-of-mass position of each cluster is marked by a red dot. The inter-switch distances are 46 nm, 44 nm and 34 nm for these three examples. Scale bars, 20 nm. (**b**) Comparison between the inter-switch distances measured using STORM (columns) and the predicted distance distribution considering the flexibility of DNA (dashed line). (**c**) STORM images of four switches attached to a dsDNA, pair-wise separated by a contour length of 46 nm. The measured switch positions are clustered by an automated algorithm and different clusters are indicated by different symbols. Scale bars, 20 nm. (**d**) STORM images of RecA-coated circular plasmid DNA. Indirect immunofluorescence images with switch-labeled secondary antibody taken by a total internal reflection microscope (top); the reconstructed STORM images of the same filaments (bottom). Scale bars, 300 nm.

# Multicolor Super-Resolution Imaging with Photo-Switchable Fluorescent Probes

Fig. 1. Photo-switchable probes constructed from activator-reporter pairs. (**A**) Spectrally distinct reporters exhibit photo-switching behavior. The lower panel shows the fluorescence time traces of three photo-switchable reporters Cy5 (dark yellow line), Cy5.5 (red line), and Cy7 (brown line), each paired with a Cy3 dye as the activator on a DNA construct. The upper panel shows the green laser pulses (532 nm) used to activate the reporters. The red laser (657 nm) was continuously on, serving to excite fluorescence from the reporters and to switch them to the dark state. Traces were shifted relative to each other for clarity. (**B**) Switching rate constants k_{on} and k_{off} of the Cy3-Cy5, Cy3-Cy5.5, and Cy3-Cy7 pairs as a function of green and red laser power. Error bars indicate SEM from about three data sets. The laser power to intensity calibration may vary between different samples because of moderate differences in the laser spot size at the sample. (**C**) The same reporter can be activated by spectrally distinct activators. The lower panel shows the fluorescence time traces of Cy5 paired with three different activators, Alexa 405 (magenta line), Cy2 (blue line), and Cy3 (green line). The upper panel shows the violet (405 nm, magenta line), blue (457 nm, blue line), and green (532 nm, green line) activation pulses. (**D**) Normalized activation rate constants of the three dye pairs at three activation wavelengths: 405, 457, and 532 nm. The k_{on} values of Alexa 405-Cy5, Cy2-Cy5, and Cy3-Cy5 were used for normalization at 405, 457, and 532 nm, respectively. The absolute activation rates were rapid for each pair at its corresponding optimal wavelength, with values of 10 s^{-1} or greater at only a few hundred μW of laser power. The activation rate of the Alexa 405-Cy5 pair by the 532-nm laser was too small to be measured reliably.

Fig. 2. Three-color STORM imaging of a model DNA sample. (**A**) Three-color STORM image of three different DNA constructs labeled with Alexa 405-Cy5, Cy2-Cy5, or Cy3-Cy5 mixed at a high surface density on a microscope slide. The image was plotted by rendering each localization as a Gaussian peak, the width of which was scaled with the theoretical localization accuracy given by the number of photons detected (26). Each colored spot in this image represents a cluster of localizations from a single DNA molecule. A conventional fluorescence image of the same area is shown in fig. S3 for comparison. (**B** and **C**) Higher-magnification views of the boxed regions in (A) show several examples of closely spaced DNA molecules. Each localization was plotted as a cross, colored according to the following code: If the molecule was activated by a 405-, 457-, or 532-nm laser pulse, the color of the cross was assigned as blue, green, or red, respectively. (**D**) The localization distributions of the blue, green, or red clusters. The two-dimensional histograms of localizations were generated by aligning multiple (50 to 60) clusters by their center of mass. The histograms were fit to a Gaussian profile to determine their FWHM.
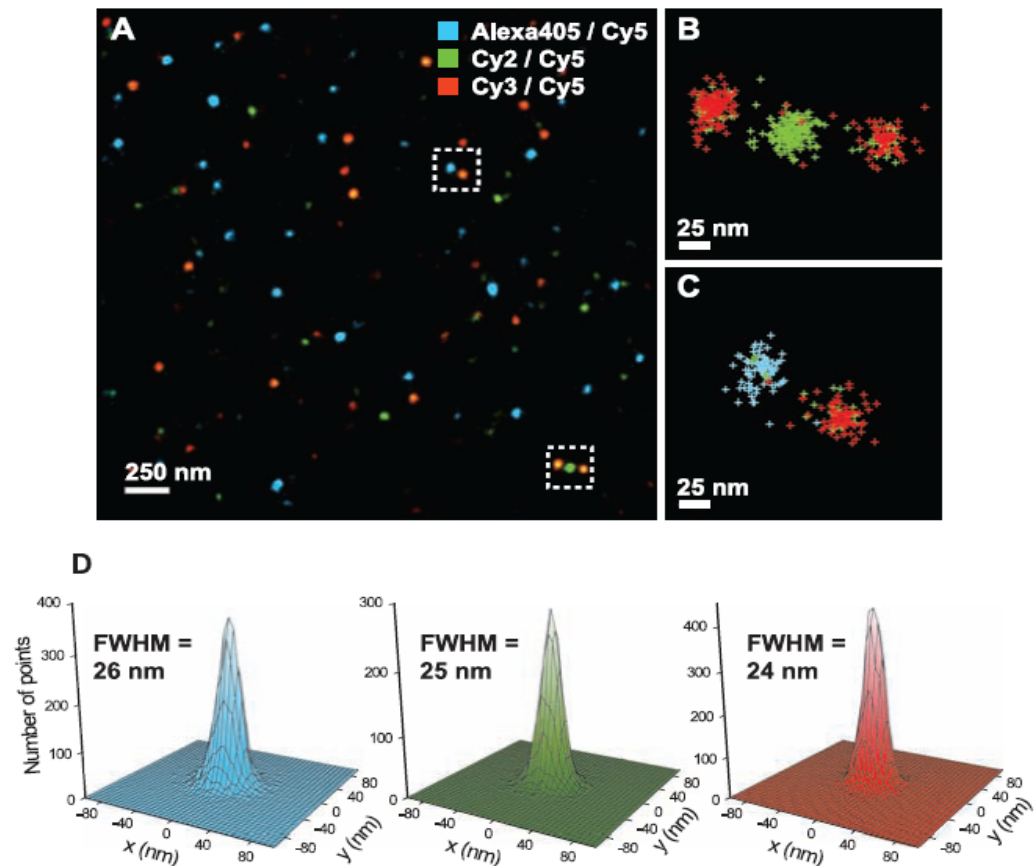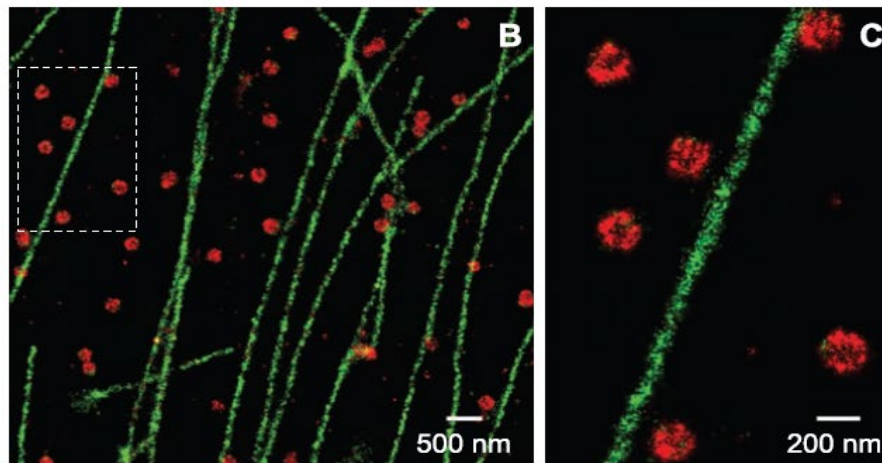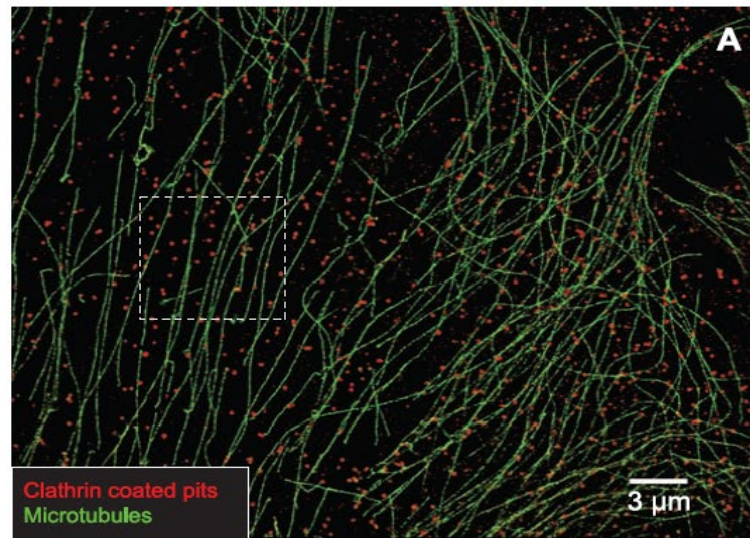
Fig. 4. Two-color STORM imaging of microtubules and CCPs in a mammalian cell. (**A**) STORM image of a large area of a BS-C-1 cell. The secondary antibodies used for microtubule staining were labeled with Cy2 and Alexa 647, and those for clathrin were labeled with Cy3 and Alexa 647. The 457- and 532-nm laser pulses were used to selectively activate the two pairs. Each localization was false colored according to the following code: green for 457-nm activation and red for 532-nm activation. (**B**) STORM image corresponding to the boxed region in (A) shown at a higher magnification. (**C**) Further magnified view of the boxed region in (B).

Three-Dimensional Super-Resolution Imaging by Stochastic Optical Reconstruction Microscopy

Fig. 1. The scheme of 3D STORM. (**A**) Three-dimensional localization of individual fluorophores. The simplified optical diagram illustrates the principle of determining the z coordinate of a fluorescent object from the ellipticity of its image by introducing a cylindrical lens into the imaging path. The right panel shows images of a fluorophore at various z positions. EMCCD, electron-multiplying charge-coupled device. (**B**) Calibration curve of image widths w_x and w_y as a function of z obtained from single Alexa 647 molecules. Each data point represents the average value obtained from six molecules. The data were fit to a defocusing function (red curve) as described in (27). (**C**) Three-dimensional localization distribution of single molecules. Each molecule gives a cluster of localizations due to repetitive activation of the same molecule. Localizations from 145 clusters were aligned by their center of mass to generate the overall 3D presentation of the localization distribution (left panel). Histograms of the distribution in x, y, and z (right panels) were fit to a Gaussian function, yielding standard deviations of 9 nm in x, 11 nm in y, and 22 nm in z.
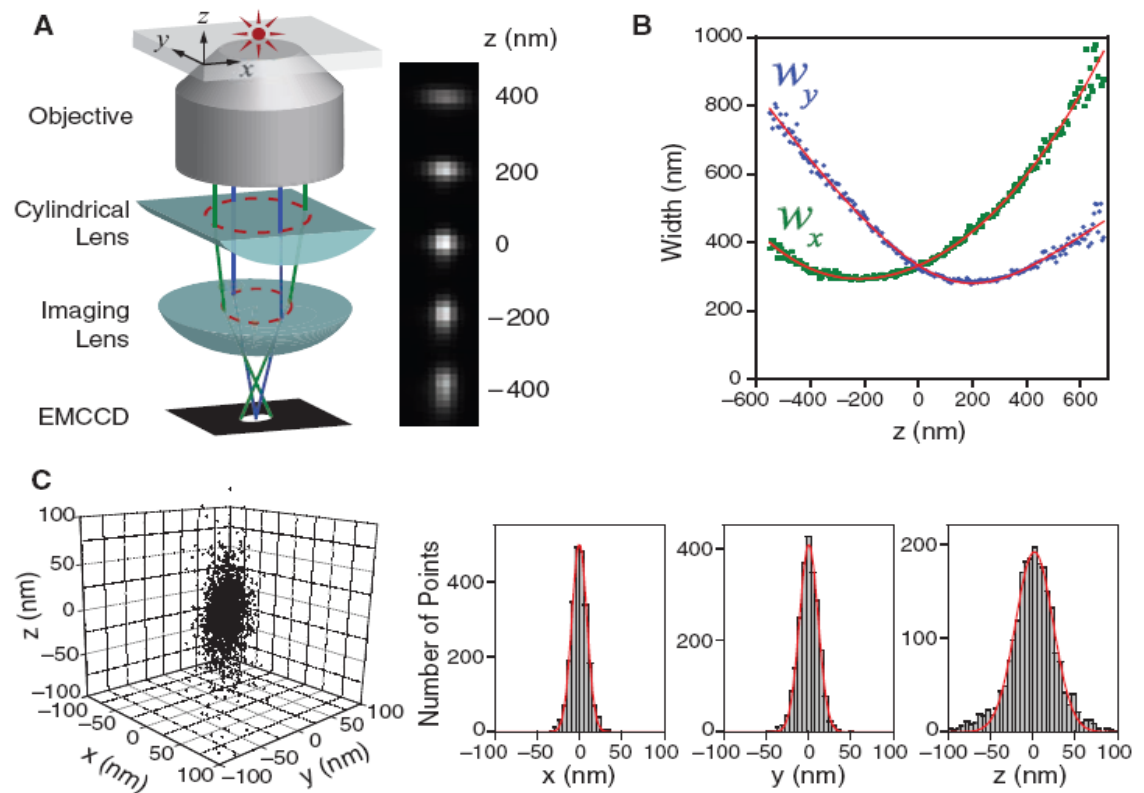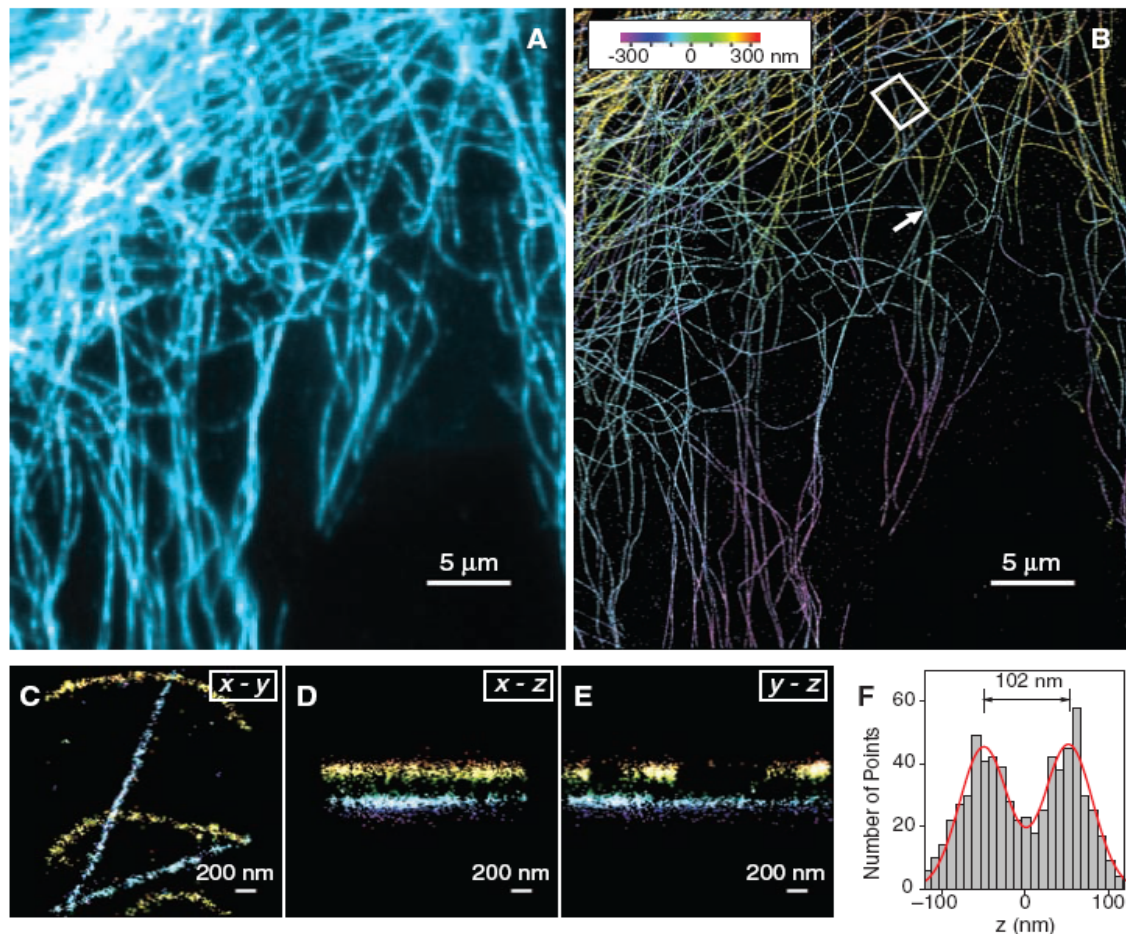
Fig. 2. Three-dimensional STORM imaging of microtubules in a cell. (**A**) Conventional indirect immunofluorescence image of microtubules in a large area of a BS-C-1 cell. (**B**) The 3D STORM image of the same area, with the *z*-position information color-coded according to the color scale bar. Each localization is depicted in the STORM image as a Gaussian peak, the width of which is determined by the number of photons detected (*5*). (**C** to **E**) The *x-y*, *x-z*, and *y-z* cross sections of a small region of the cell outlined by the white box in (B), showing five microtubule filaments. Movie S1 shows the 3D representation of this region, with the viewing angle rotated to show different perspectives (*27*). (**F**) The *z* profile of two microtubules crossing in the *x-y* projection but separated by 102 nm in *z*, from a region indicated by the arrow in (B). The histogram shows the distribution of *z* coordinates of the localizations, fit to two Gaussians with identical widths (FWHM = 66 nm) and a separation of 102 nm (red curve). The apparent width of 66 nm agrees quantitatively with the convolution of our imaging resolution in *z* (represented by a Gaussian function with FWHM of 55 nm) and the previously measured width of antibody-coated microtubules (represented by a uniform distribution with a width of 56 nm) (*5*).
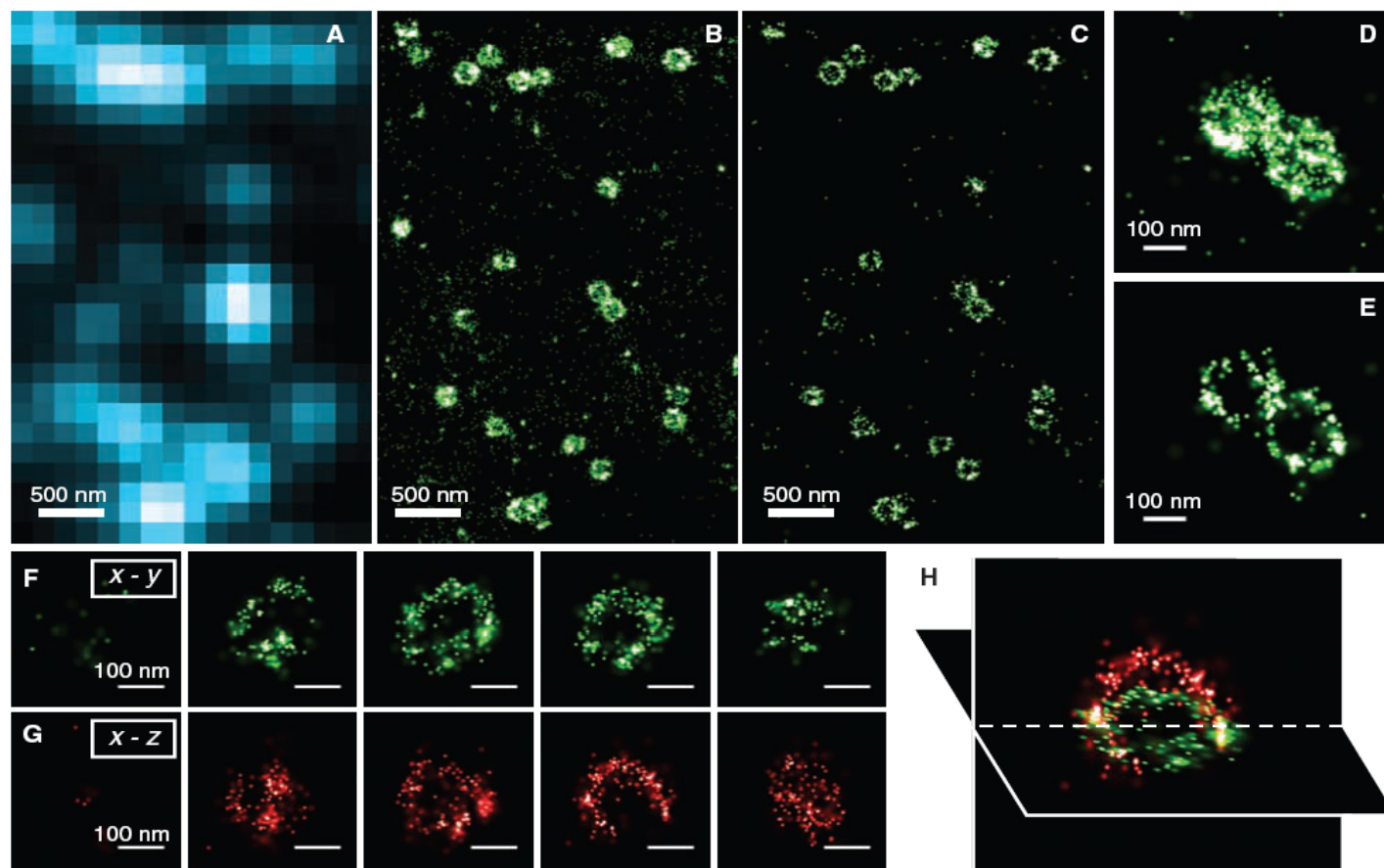
Fig. 3. Three-dimensional STORM imaging of clathrin-coated pits in a cell. (**A**) Conventional direct immunofluorescence image of clathrin in a region of a BS-C-1 cell. (**B**) The 2D STORM image of the same area, with all localizations at different z positions included. (**C**) An x-y cross section (50 nm thick in z) of the same area, showing the ring-like structure of the periphery of the CCPs at the plasma membrane. (**D** and **E**) Magnified view of two nearby CCPs in 2D STORM (D) and their x-y cross section (100 nm thick) in the 3D image (E). (**F** to **H**) Serial x-y cross sections (each 50 nm thick in z) (F) and x-z cross sections (each 50 nm thick in y) (G) of a CCP, and an x-y and x-z cross section presented in 3D perspective (H), showing the half-spherical cage-like structure of the pit.

Rapid communication

Ground-state-depletion fluorscence microscopy: a concept for breaking the diffraction resolution limit

S.W. Hell, M. Kroug

Department of Medical Physics, University of Turku, and Centre for Biotechnology, P.O. Box 123, FIN-20521 Turku, Finland
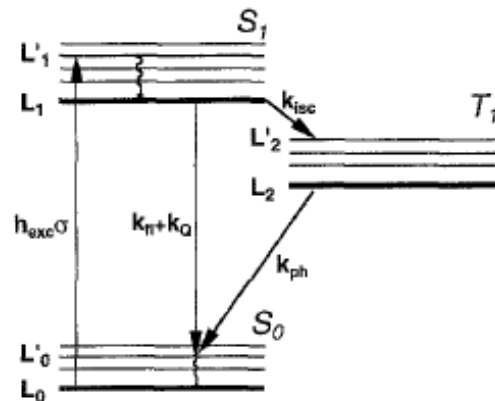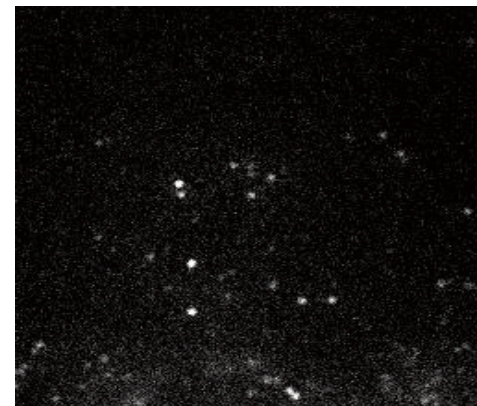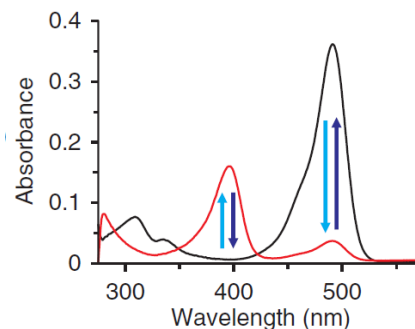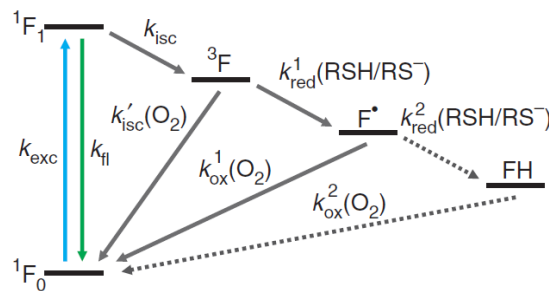(Fax: +358-21/633-8000, E-mail: STEFAN.HELL@utu.fi)

Fig. 1. Energy states of a typical dye: S_0 is the ground state, S_1 is the first singlet state, and T_1 the first triplet state

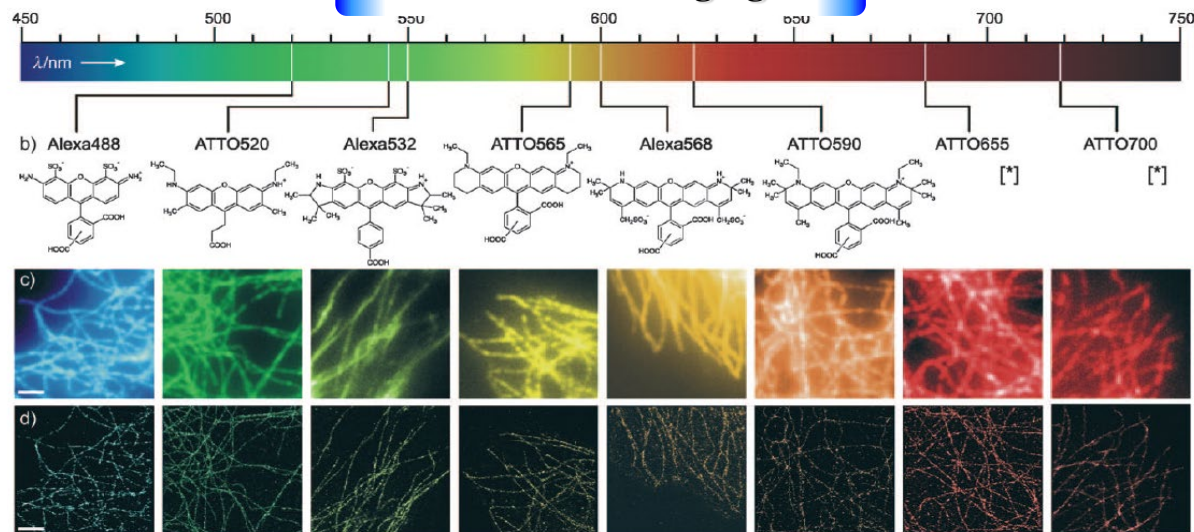# Direct stochastic optical reconstruction microscopy (dSTORM)

Reversible photoswitching mechanism of standard fluorophores
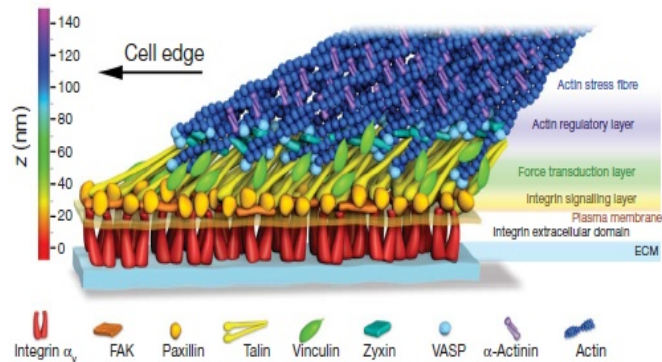

Localization imaging concept

Multicolor imaging

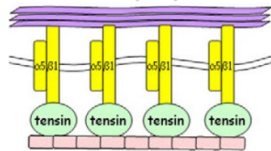Angew. Chem. Int. Ed. 2008, 2009, Nature protocols 2011
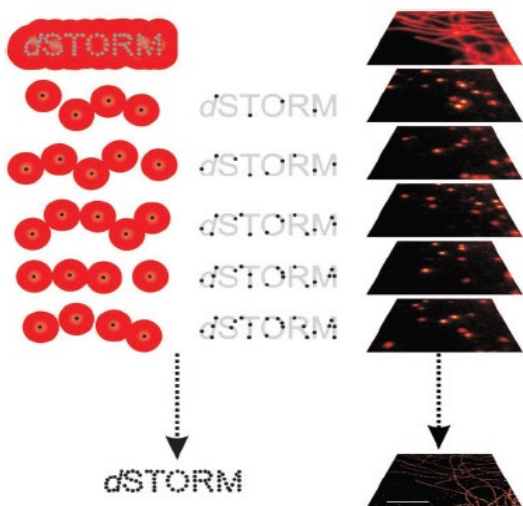
Multicolor superresolution fluorescence imaging
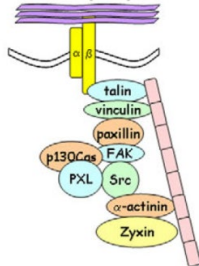
Objective

1. Characteristic distance between focal adhesion complexes.
2. Cross-correlation between different focal adhesion complexes.
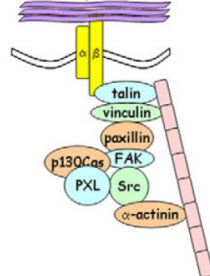3. Number of focal adhesion complexes at different adhesion types.

J. Cell Sci. (2010).
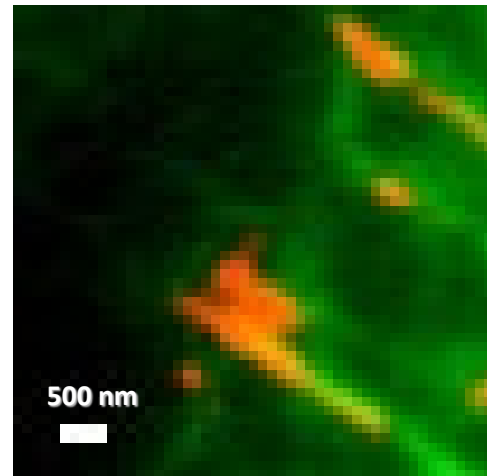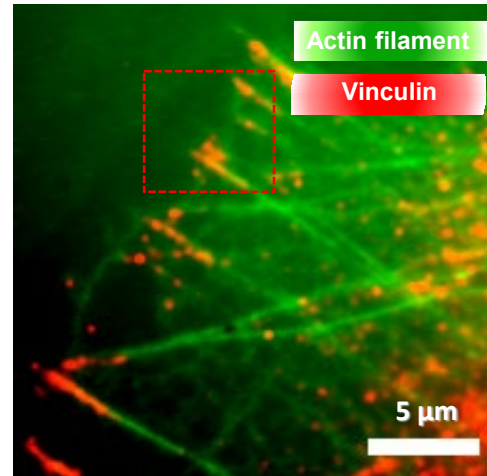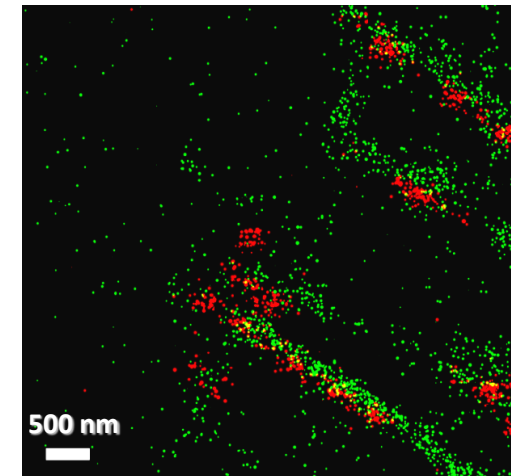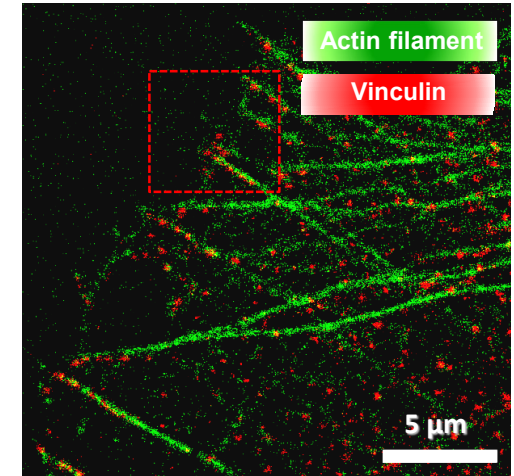
4 Pi

Schematic of the 4Pi microscope
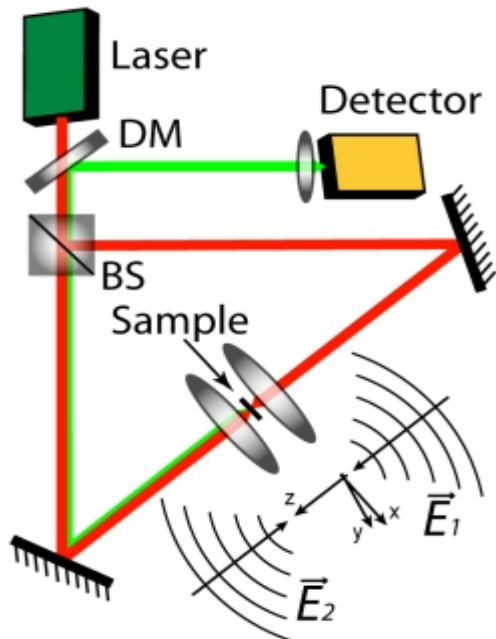
Laser
DM
Detector
BS
Sample
$\vec{E}_1$
$\vec{E}_2$

Theoretical and Computational Biophysics Group
Beckman Institute
University of Illinois at Urbana-Champaign

a
$\vec{E}_1$
$\vec{E}_2$

b
PSF (arb. u.)
x (μm)

c
PSF (arb. u.)
z (μm)

d
500 nm

e
30°
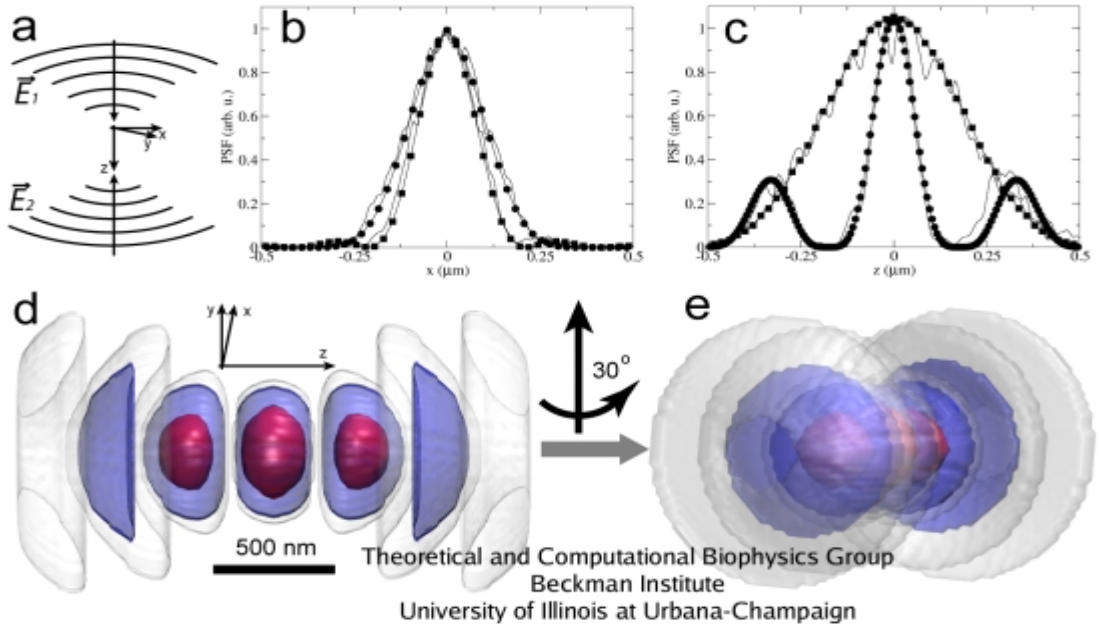
Theoretical and Computational Biophysics Group
Beckman Institute
University of Illinois at Urbana-Champaign
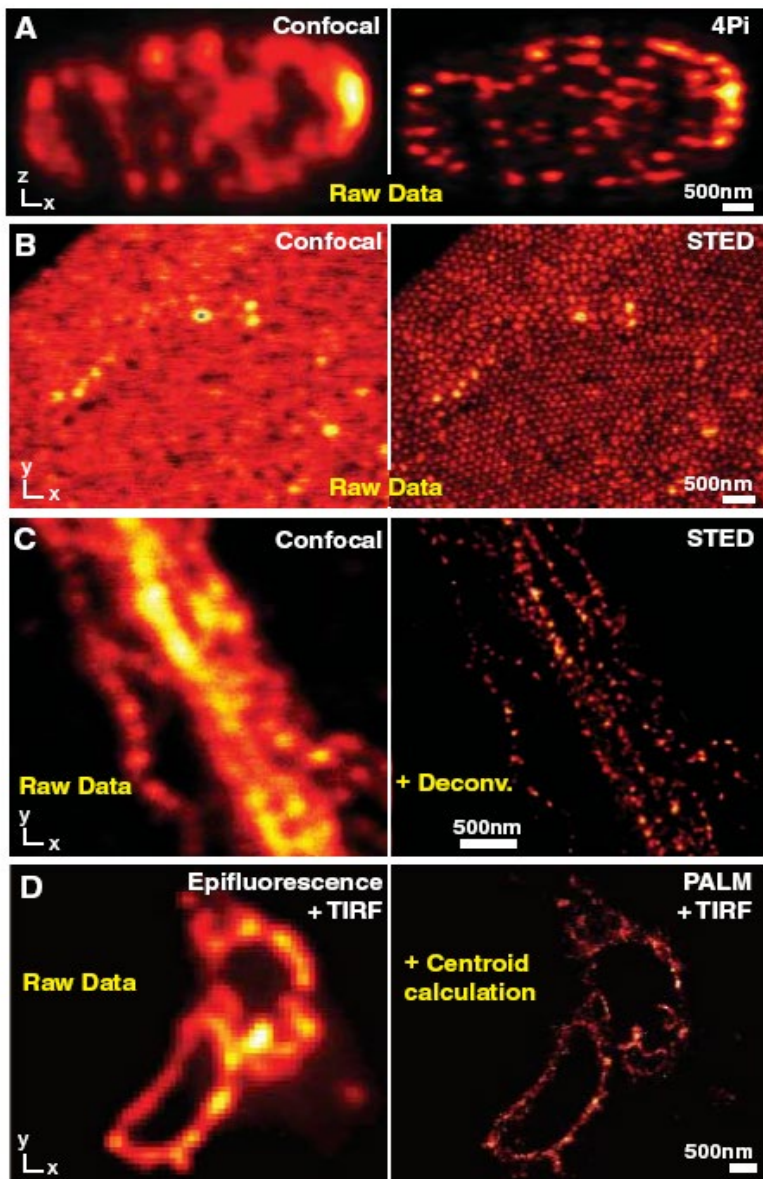
Fig. 4. Side-by-side comparisons. (**A**) Confocal versus 4Pi axial (*xz*) image of microtubules in a neuron: 4Pi image displays 140-nm *z* resolution; lens of $\alpha = 74°$ and with two-photon excitation at 800 nm. The plain 4Pi image is due to a narrow solitary peak without lobes; mathematical lobe-removal is not required. (**B**) Unlike the confocal reference, the STED image reveals the spatial order of self-assembled fused silica nanobeads containing a fluorescence core (45). (**C**) Neurofilaments in human neuroblastoma recorded in the confocal mode (left) and with STED after nonlinear deconvolution (right) displaying a focal plane resolution of 20 to 30 nm (39). (**D**) Epifluorescence versus PALM recording of a cryoprepared section from a mammalian cell expressing a lysosomal transmembrane protein tagged with a photoswitchable protein; both images were recorded with a TIRF setup. PALM resolution ranges between 20 and 60 nm, whereas individual protein localizations can be 2 nm (12).

STED microscopy

a)

Avalanche Photodiode

λ/2 Phaseplate

Fluorescence 645 – 715 nm

STED 761 nm

Δt

Excitation 558 nm

100 X
1.4 Oil

b) STED

04 nm

97 nm

c) confocal

244 nm

490 nm

a

y
x

0 — 775
Counts / 0.15 ms

b

r

y
x

0 — 204
Counts / 0.15 ms

c

y
x

d

y
x

e

Confocal

34 nm

Counts / 0.15 ms

Counts / 0.15 ms

CW STED

400

200

80

40

0   200   400
r (nm)
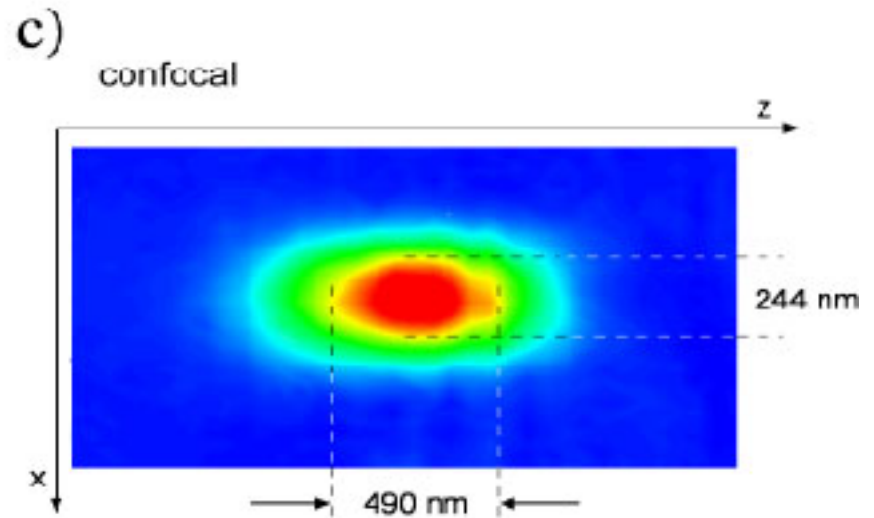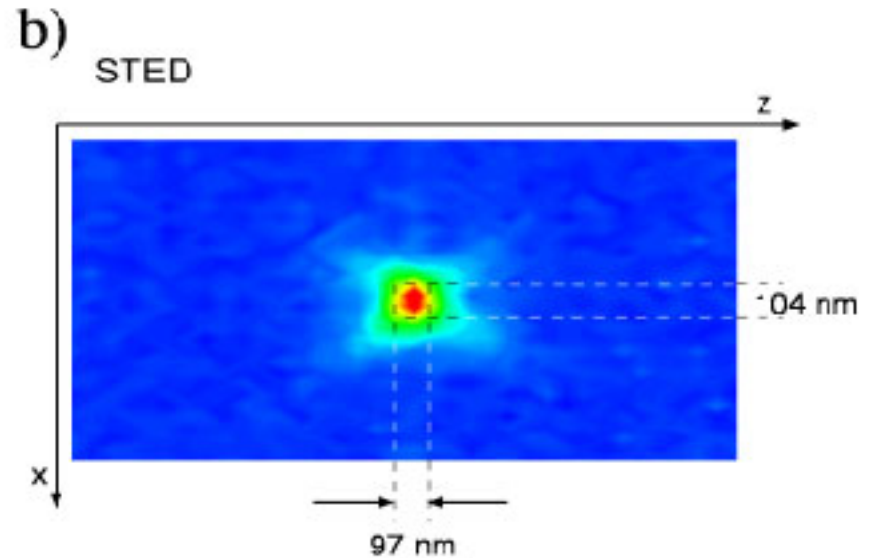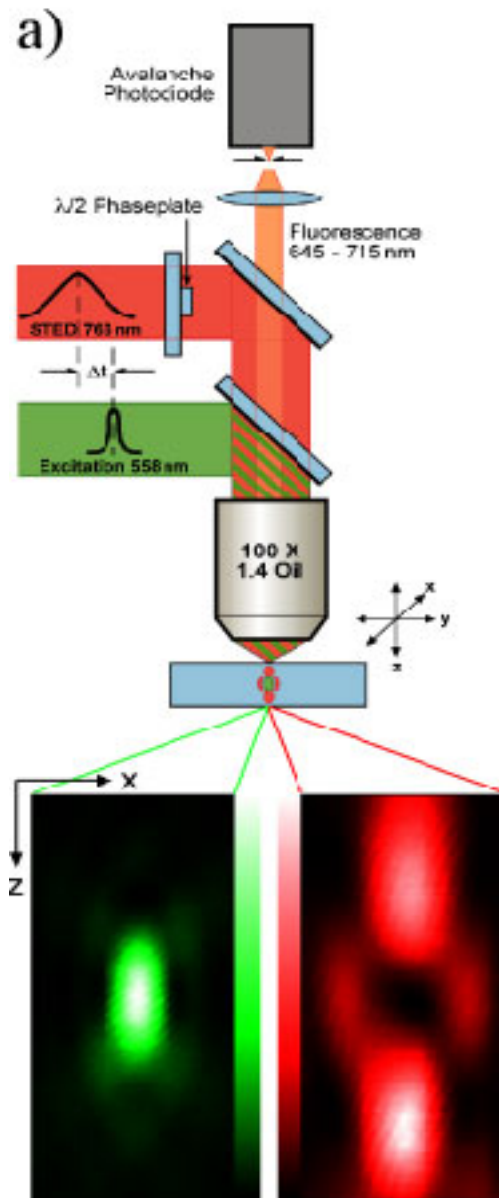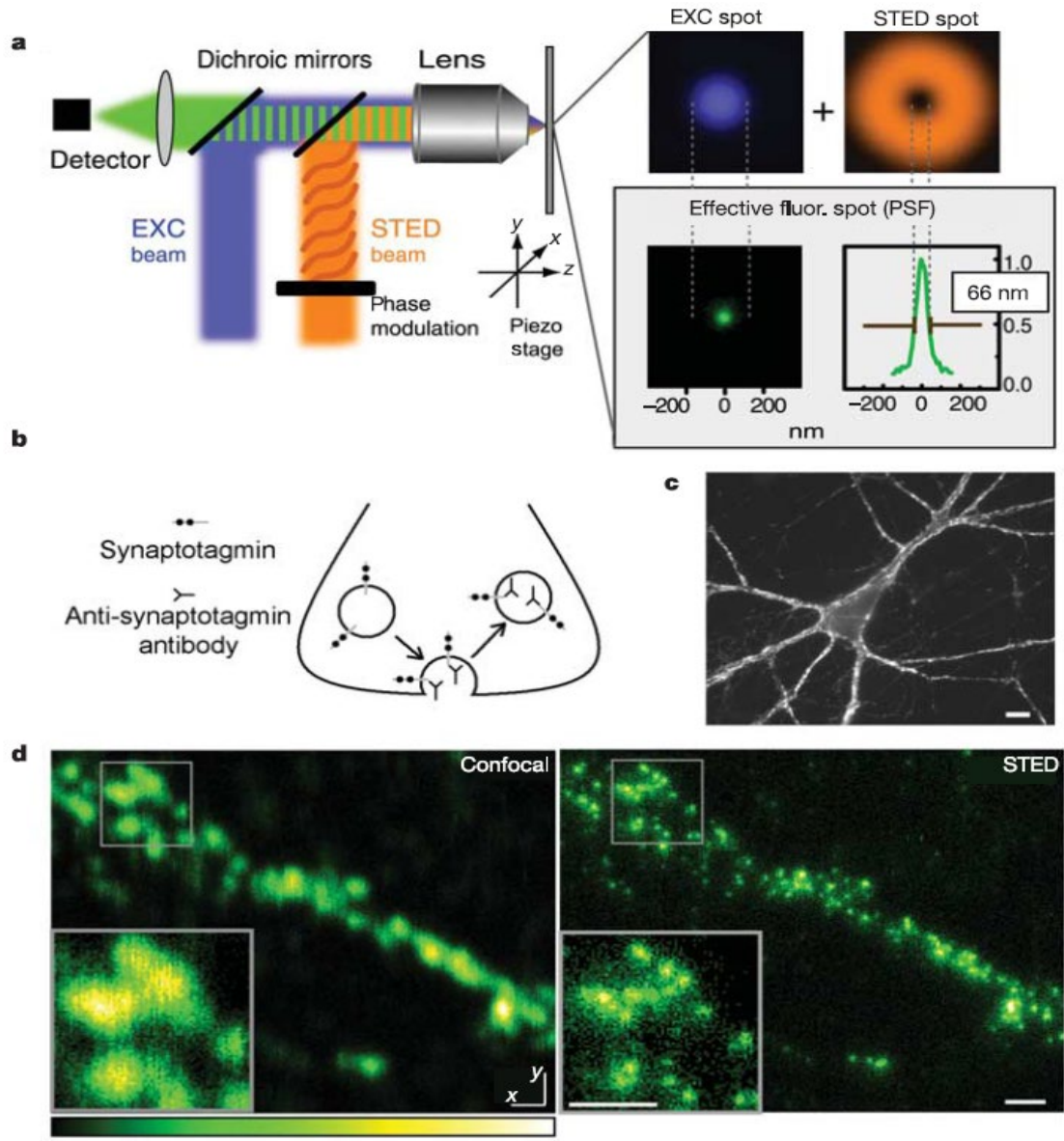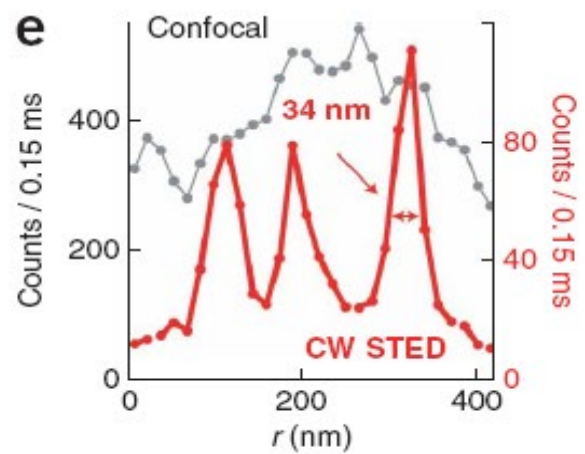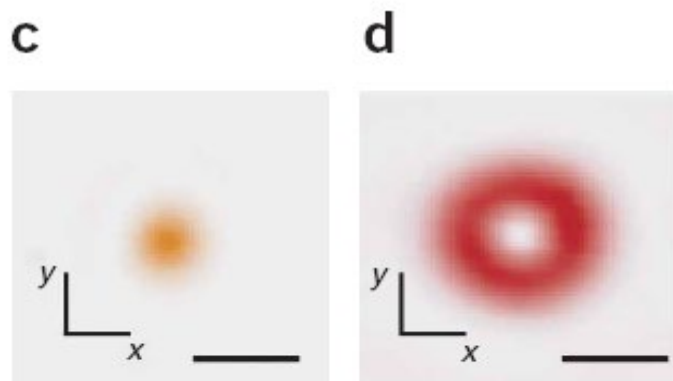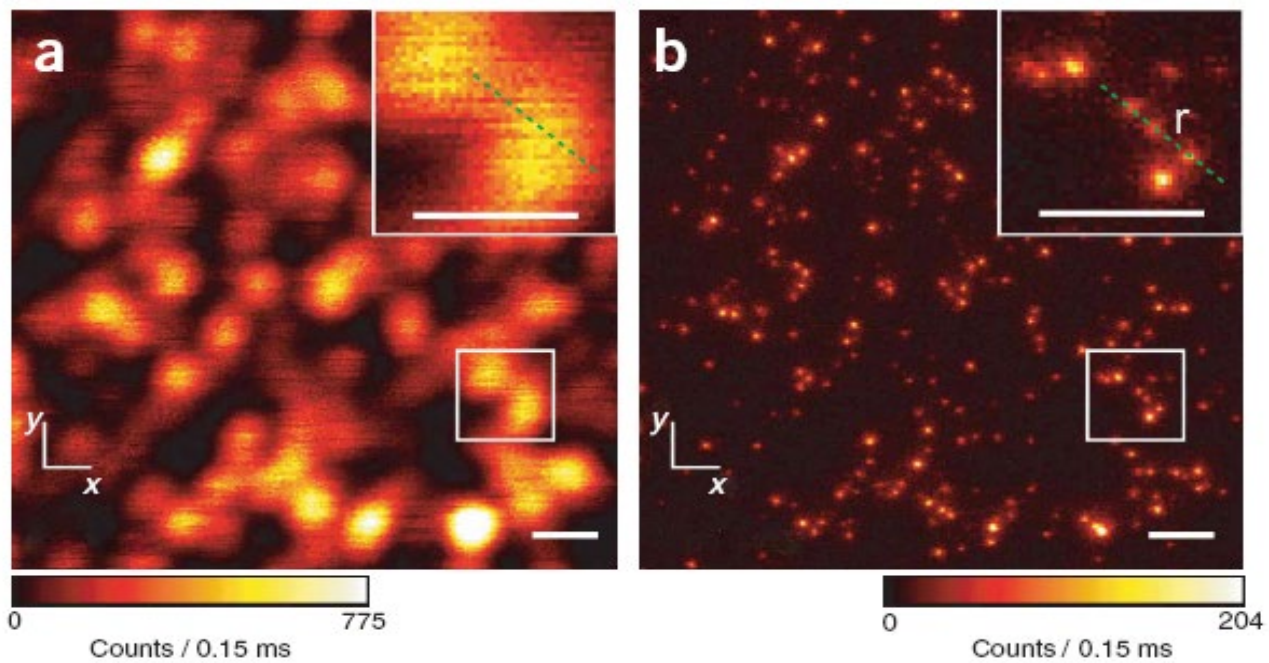
Nanometer resolution imaging and tracking of fluorescent molecules with minimal photon fluxes

Francisco Balzarotti,[1]*† Yvan Eilers,[1]* Klaus C. Gwosch,[1]* Arvid H. Gynnå,[2] Volker Westphal,[1] Fernando D. Stefani,[3,4] Johan Elf,[2] Stefan W. Hell[1,5,6]†

MINFLUX nanoscopy delivers 3D multicolor nanometer resolution in cells

minimal photon flux
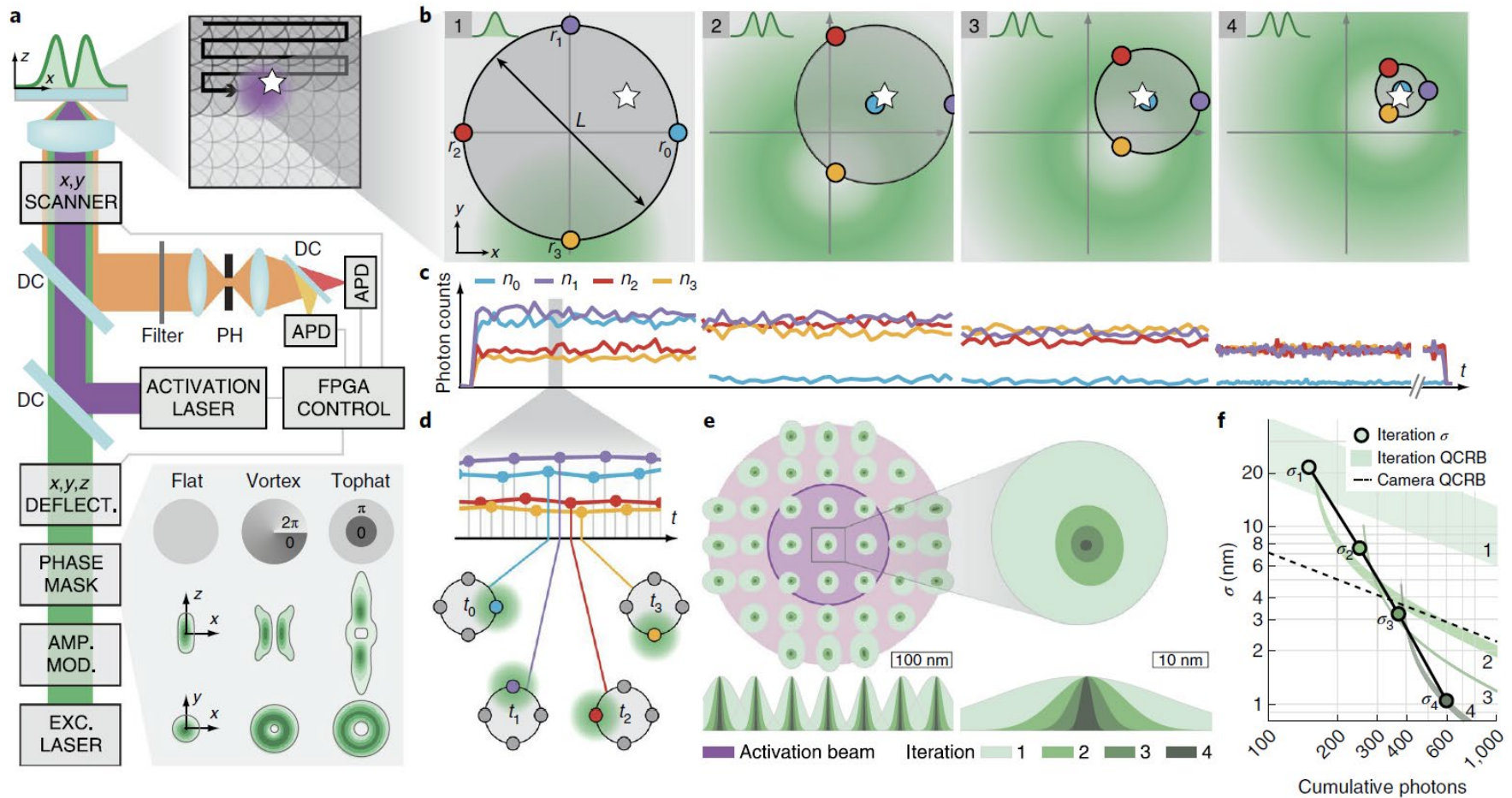
Operation Principle of MINFLUX

Illumination Pattern: MINFLUX uses a donut-shaped laser beam, which has a zero-intensity dark spot at its center. This unique configuration is crucial for the method's high-resolution capability.
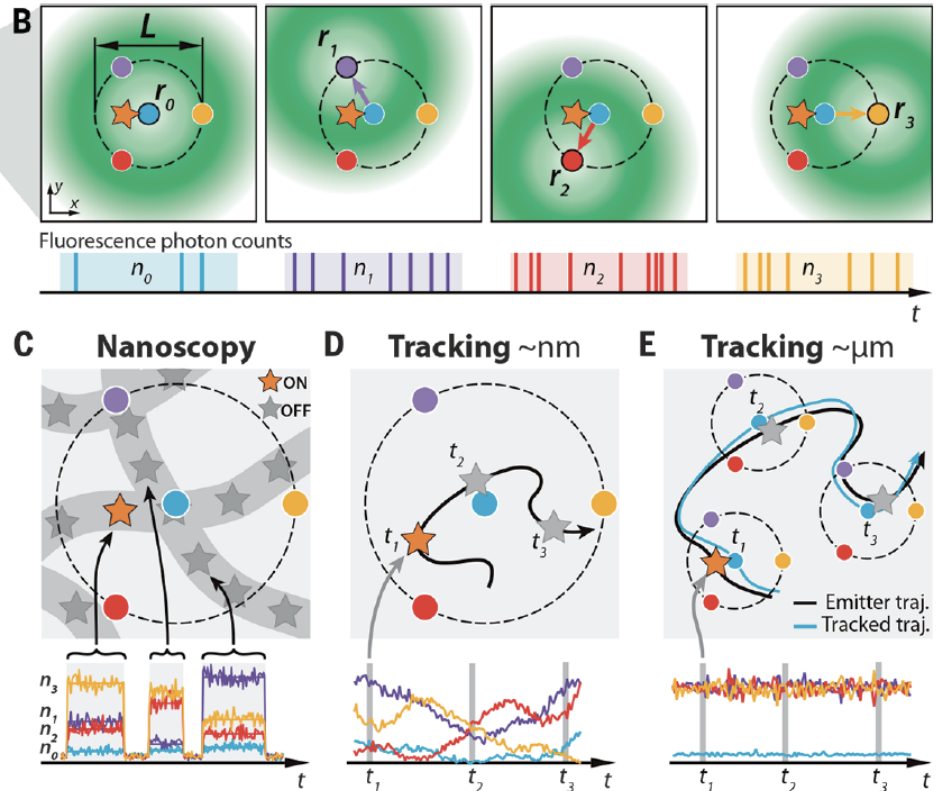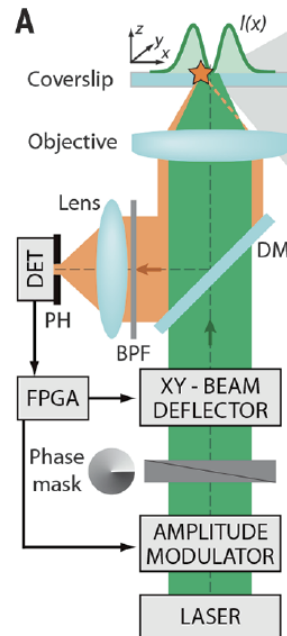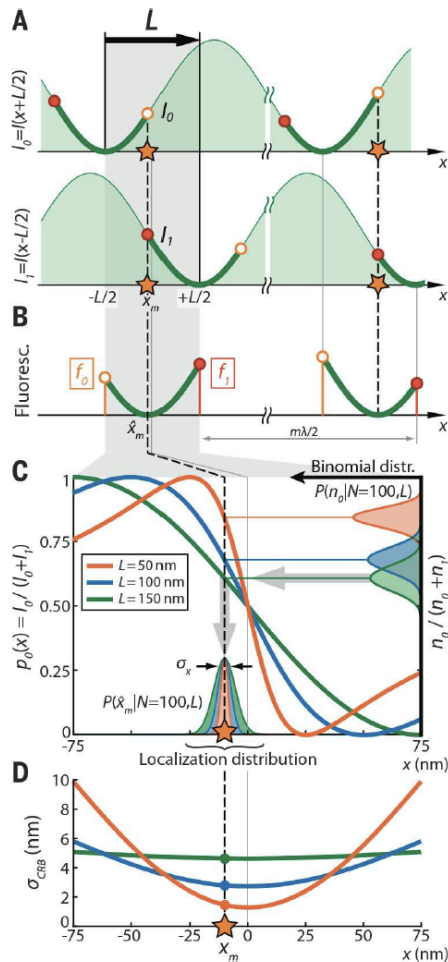
Positioning the Dark Spot: The central idea is to position this dark spot near the fluorescent molecule of interest. The precise localization is achieved by detecting where the photons are emitted relative to this dark spot.

Photon Emission: As the fluorescent molecule emits photons, the position of the dark spot is adjusted based on where these photons are detected. The goal is to center the dark spot as close as possible to the actual position of the molecule.

Iterative Refinement: The process involves iterative adjustments of the dark spot's position. With each iteration, the system collects data on photon emissions, refining the estimated position of the fluorophore.

Efficient Use of Photons: By focusing the interrogation to the vicinity of the dark spot and iteratively narrowing down the position, MINFLUX significantly reduces the number of photons needed to achieve localization. This efficiency helps in reducing photobleaching and photo-toxicity, which are common issues in super-resolution microscopy.

High Localization Precision: The iterative process, combined with the unique illumination pattern, allows MINFLUX to achieve localization precisions in the range of sub-nanometers, surpassing the capabilities of many existing super-resolution techniques.

a

b

Median 0.9 nm

Median 0.9 nm

σ_x (nm)

σ_y (nm)

c

3σ

2σ

σ

$\sigma = 0.9$ nm

d

Resolution (nm)

2.8 nm

1/7

Spatial frequency (nm^{-1})

e

(1)

(2)

(3)

f

(1)

(2)

(3)

a

b

1	2	3	4	5
xy localization	*z* localization	*xyz* localization	*xyz* localization	*xyz* localization

c

d

e

$\sigma_z^{(i)}$
$CRB_z^{(i)}$

$CRB_z^{(ast)}$
$QCRB_z^{(2\pi)}$
$QCRB_z^{(4\pi)}$

Axial precision σ_z (nm)

Cumulative photons

f

Axial position (nm)

(1) (2) (3) (4)

g

(1)
(2)
(3)
(4)

h

3σ
2σ
σ

$\sigma_{xy} = 2.4$ nm
$\sigma_z = 1.7$ nm

i

Median 2.6 nm
Median 2.6 nm
Median 1.8 nm

Bin counts

σ_x (nm)
σ_y (nm)
σ_z (nm)

a

~11 nm

~10 nm

CF660C

Alexa Fluor 647

b

c

y
x

z
x

d

Bin counts

CF660C

Alexa Fluor 647

−0.4 −0.2 0 0.2
Spectral splitting (PCA)

e

Bin counts

10.2 nm   11.3 nm

1.3 nm   1.5 nm   1.8 nm

−15 −10 −5 0 5 10
Profile *xy* (nm)

f

Bin counts

WGA
(CF680)

Nup96
(Alexa Fluor 647)

−0.5 0 0.5
Spectral splitting (PCA)

g

Bin counts

46 nm

−50 0 50
Relative position *z* (nm)

MINFLUX dissects the unimpeded walking of kinesin-1

Jan O. Wirth[1]†, Lukas Scheiderer[1]†, Tobias Engelhardt[1]‡, Johann Engelhardt[1],
Jessica Matthias[1]‡, Stefan W. Hell[1,2]*
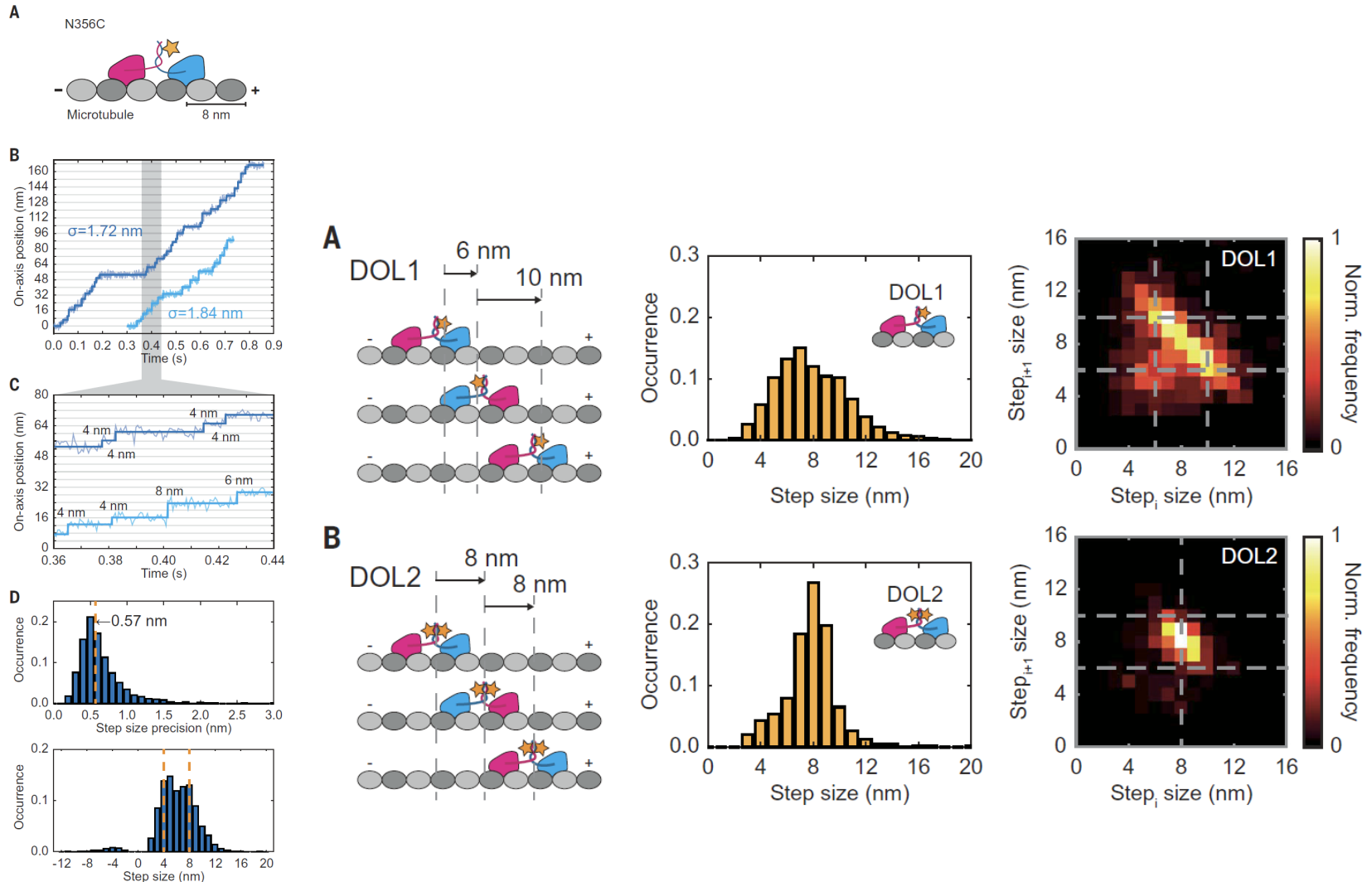
STED Microscopy:

Depletion Beam: STED uses a donut-shaped depletion beam that surrounds a central excitation spot. This depletion beam effectively "turns off" fluorescence by stimulating the emission of photons from the excited state to the ground state, excluding the central spot where the fluorescence remains active.
Resolution Enhancement: By reducing the effective volume of fluorescence, STED can achieve a much higher resolution than conventional confocal microscopy. The resolution is limited by the intensity of the STED beam—the higher the intensity, the greater the resolution.

MINFLUX:

Photon-efficient Localization: MINFLUX uses a donut-shaped illumination pattern similar to STED but for a different purpose. Instead of depleting fluorescence, the zero-intensity center of the beam is used to pinpoint the location of fluorescent molecules with minimal photon emission.
Iterative Positioning: The core of MINFLUX is the iterative positioning of the dark spot near the fluorophore and detecting where photons are emitted. This process minimizes the number of photons needed for high-precision localization, leading to extremely high resolution with less photobleaching compared to other methods.

Key Differences

STED achieves high resolution by physically restricting the fluorescence emission area, which can require high laser intensities and may lead to photobleaching.
MINFLUX achieves similar or better resolutions by optimizing the photon budget and reducing the area needed for scanning to localize molecules, which is significantly photon-efficient and reduces photodamage.

STED involves complex and expensive setup due to the high-power lasers required for the depletion beam and the need for precise alignment of the excitation and depletion beams.
MINFLUX, while also complex, primarily focuses on the innovative use of photon detection and spatial manipulation, potentially allowing for more straightforward adaptations in existing fluorescence microscopy setups.

STED is widely used for imaging structures at the nanoscale within biological tissues and cells, particularly useful in neuroscience and cell biology where high-resolution images of dense molecular complexes are needed.
MINFLUX is particularly advantageous for tracking single-molecule dynamics with high temporal resolution and minimal photobleaching, making it ideal for live-cell imaging and dynamic molecular studies.

SHORT COMMUNICATION

Surpassing the lateral resolution limit by a factor of two using structured illumination microscopy

M. G. L. GUSTAFSSON

Department of Biochemistry and Biophysics, University of California San Francisco,
San Francisco, California 94143-0448, U.S.A.
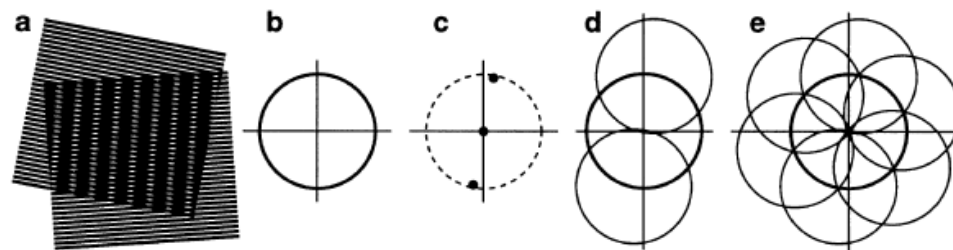
Fig. 1. Concept of resolution enhancement by structured illumination. (a) If two line patterns are superposed (multiplied), their product will contain moiré fringes (seen here as the apparent vertical stripes in the overlap region). (b) A conventional microscope is limited by diffraction. The set of low-resolution information that it can detect defines a circular 'observable region' of reciprocal space. (c) A sinusoidally striped illumination pattern has only three Fourier components. The possible positions of the two side components are limited by the same circle that defines the observable region (dashed). If the sample is illuminated with such structured light, moiré fringes will appear which represent information that has changed position in reciprocal space. The amounts of that movement correspond to the three Fourier components of the illumination. The observable region will thus contain, in addition to the normal information, moved information that originates in two offset regions (d). From a sequence of such images with different orientation and phase of the pattern, it is possible to recover information from an area twice the size of the normally observable region, corresponding to twice the normal resolution (e).
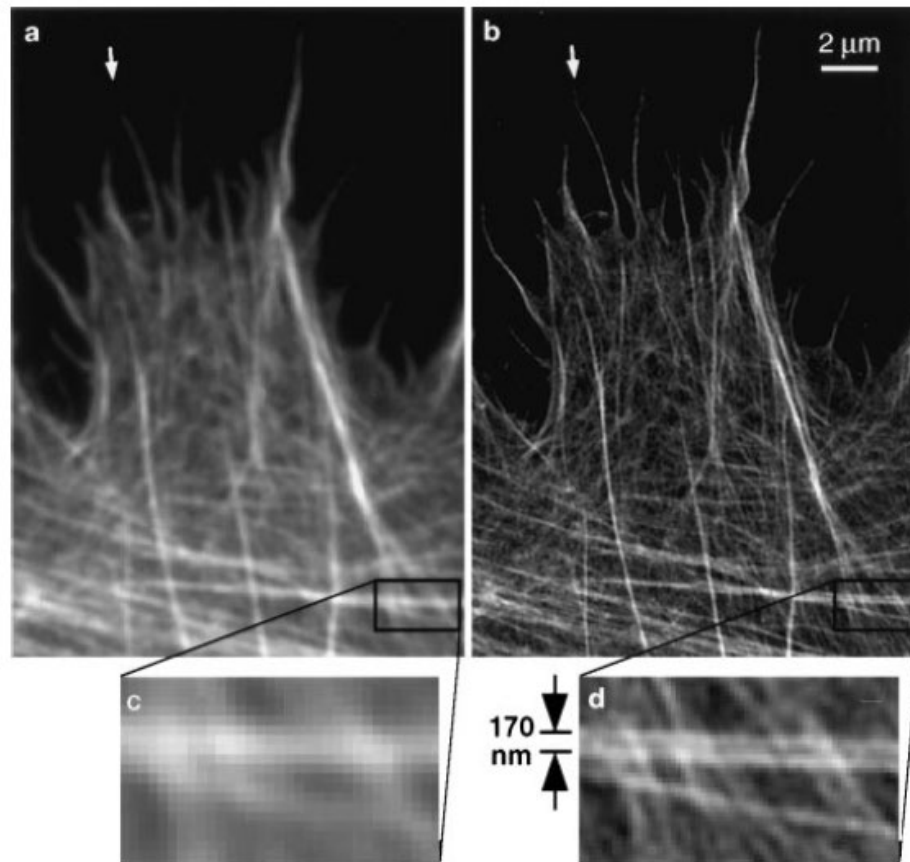
Fig. 4. The actin cytoskeleton at the edge of a HeLa cell, as imaged by (a, c) conventional and (b, d) structured illumination microscopy. (c, d) Enlargements of the boxed areas in (a) and (b), respectively. Fibres separated by less than the resolution limit of the conventional microscope are well resolved using structured illumination (d). The apparent widths (FWHM) of the finest protruding fibres [small arrows in (a, b)] are lowered to 110–120 nm in (b), compared to 280–300 nm in (a).

Nonlinear structured-illumination microscopy: Wide-field fluorescence imaging with theoretically unlimited resolution
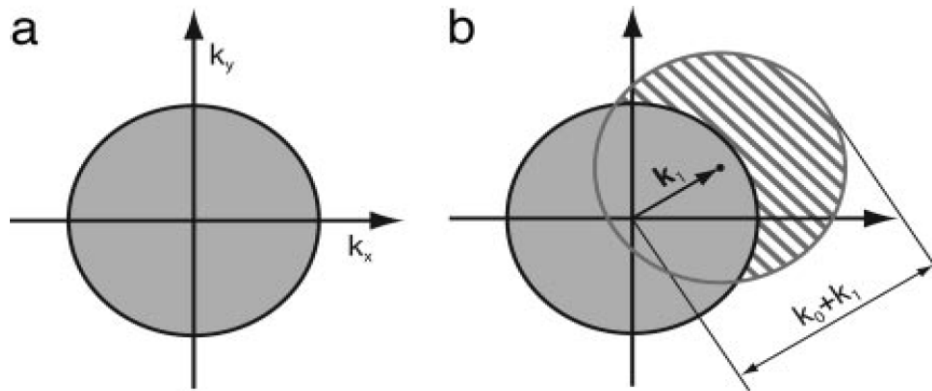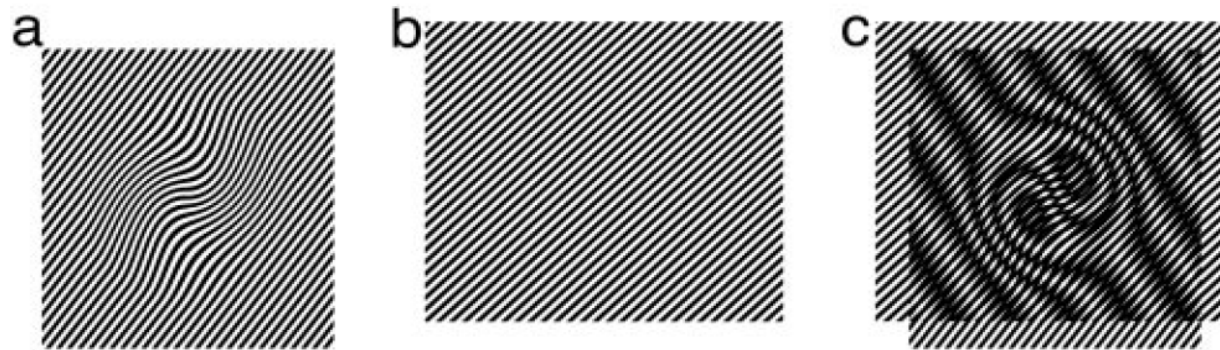
Fig. 2. Structured-illumination concept. (a) The set of sample spatial frequencies that can be observed by the conventional microscope defines a circular observable region of radius k_0 in frequency space. (b) If the excitation light contains a spatial frequency k_1, a new set of information becomes visible in the form of moiré fringes (hatched circle). This region has the same shape as the normal observable region but is centered at k_1. The maximum spatial frequency that can be detected (in this direction) is $k_0 + k_1$.

a

b

c

a

b

c

d

e
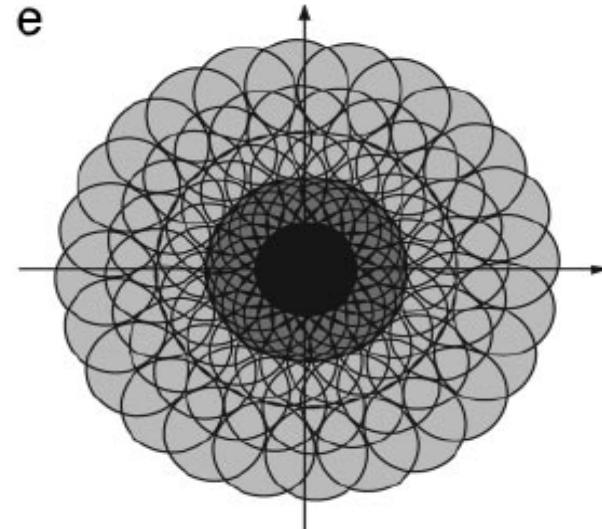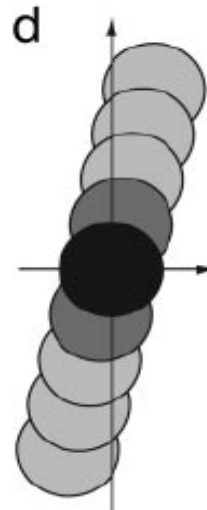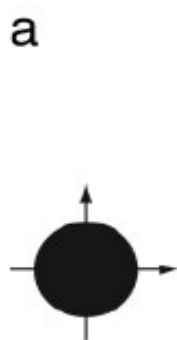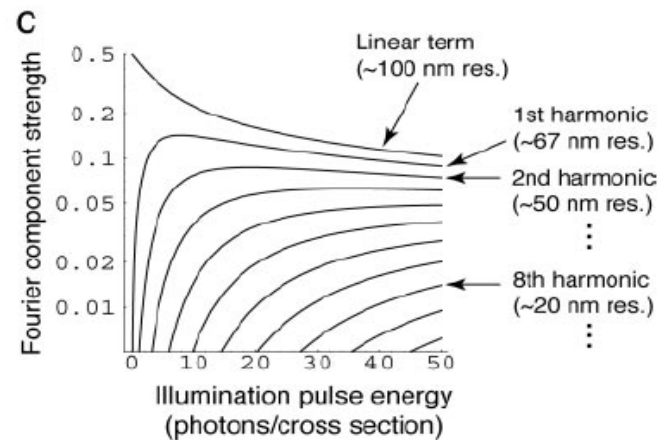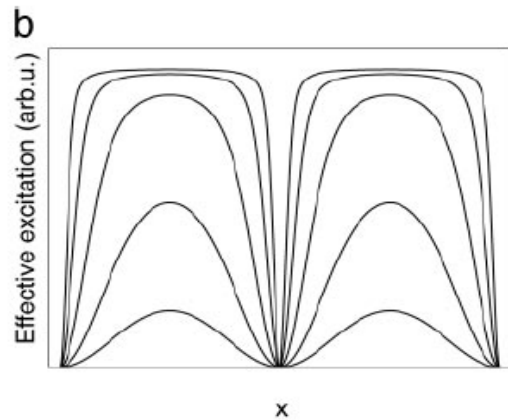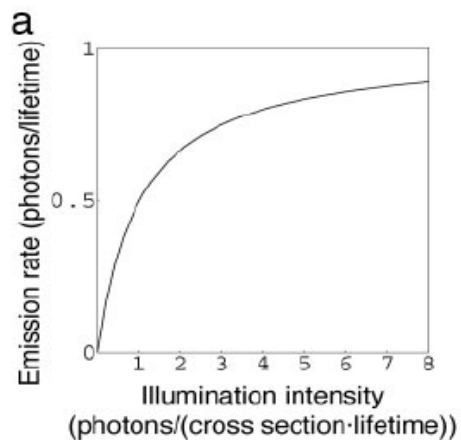
Subdiffraction Multicolor Imaging of the Nuclear Periphery with 3D Structured Illumination Microscopy

Lothar Schermelleh,[1]* Peter M. Carlton,[2]* Sebastian Haase,[2,4] Lin Shao,[2] Lukman Winoto,[2] Peter Kner,[2] Brian Burke,[3] M. Cristina Cardoso,[4] David A. Agard,[2] Mats G. L. Gustafsson,[5] Heinrich Leonhardt,[1]*† John W. Sedat[2]*†

Fig. 1. Subdiffraction resolution imaging with 3D-SIM. (**A** and **B**) Cross section through a DAPI-stained C2C12 cell nucleus acquired with conventional wide-field illumination (A) and with structured illumination (B), showing the striped interference pattern (inset). The renderings to the right illustrate the respective support of detection in frequency space. The axes k_x, k_y, and k_z indicate spatial frequencies along the x, y, and z directions. The surfaces of the renderings represent the corresponding resolution limit. The depression of the frequency support ("missing cone") in z direction in (A) indicates the restriction in axial resolution of conventional wide-field microscopy. With 3D-SIM, the axial support is extended but remains within the resolution limit. (**C**) Five phases of the sine wave pattern are recorded at each z position, allowing the shifted components to be separated and returned to their proper location in frequency space. Three image stacks are recorded with the diffraction grating sequentially rotated into three positions 60° apart, resulting in nearly rotationally symmetric support over a larger region of frequency space. (**D**) The same cross section of the reconstructed 3D-SIM image shows enhanced image details compared with the original image (insets). The increase in resolution is shown in frequency space on the right, with the coverage extending two times farther from the origin. Scale bars indicate 5 μm.

	Widefield raw	Widefield+deconvolution	3D-SIM

A Mid section — DAPI

B Apical section

C Orthogonal
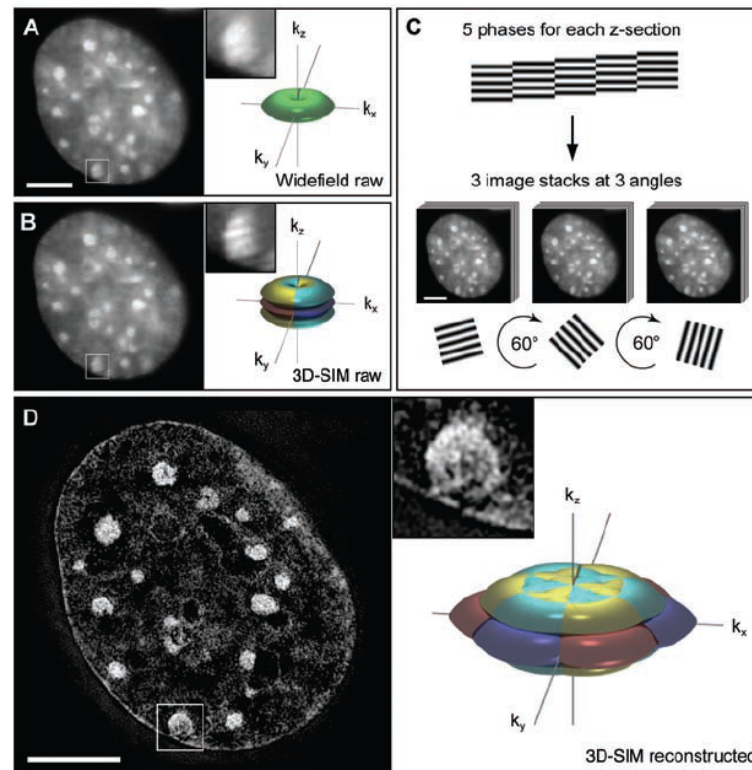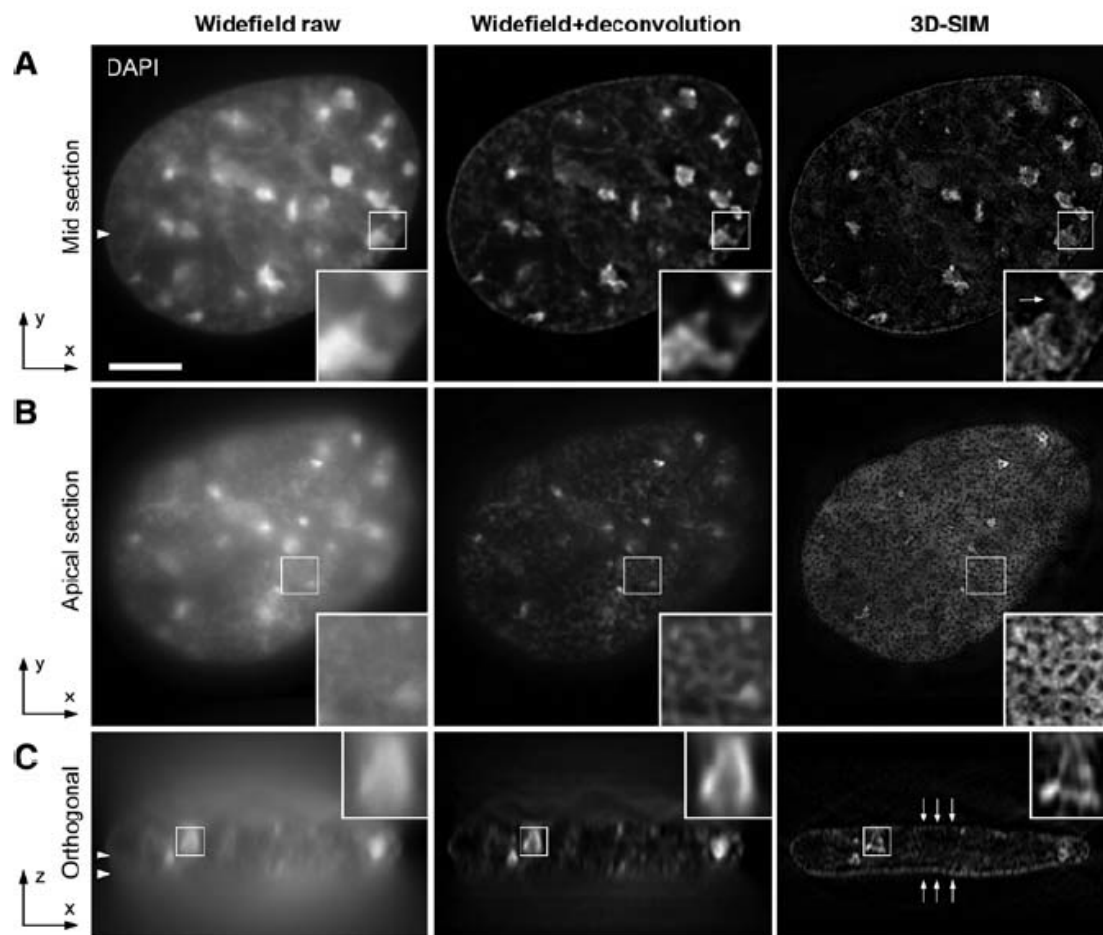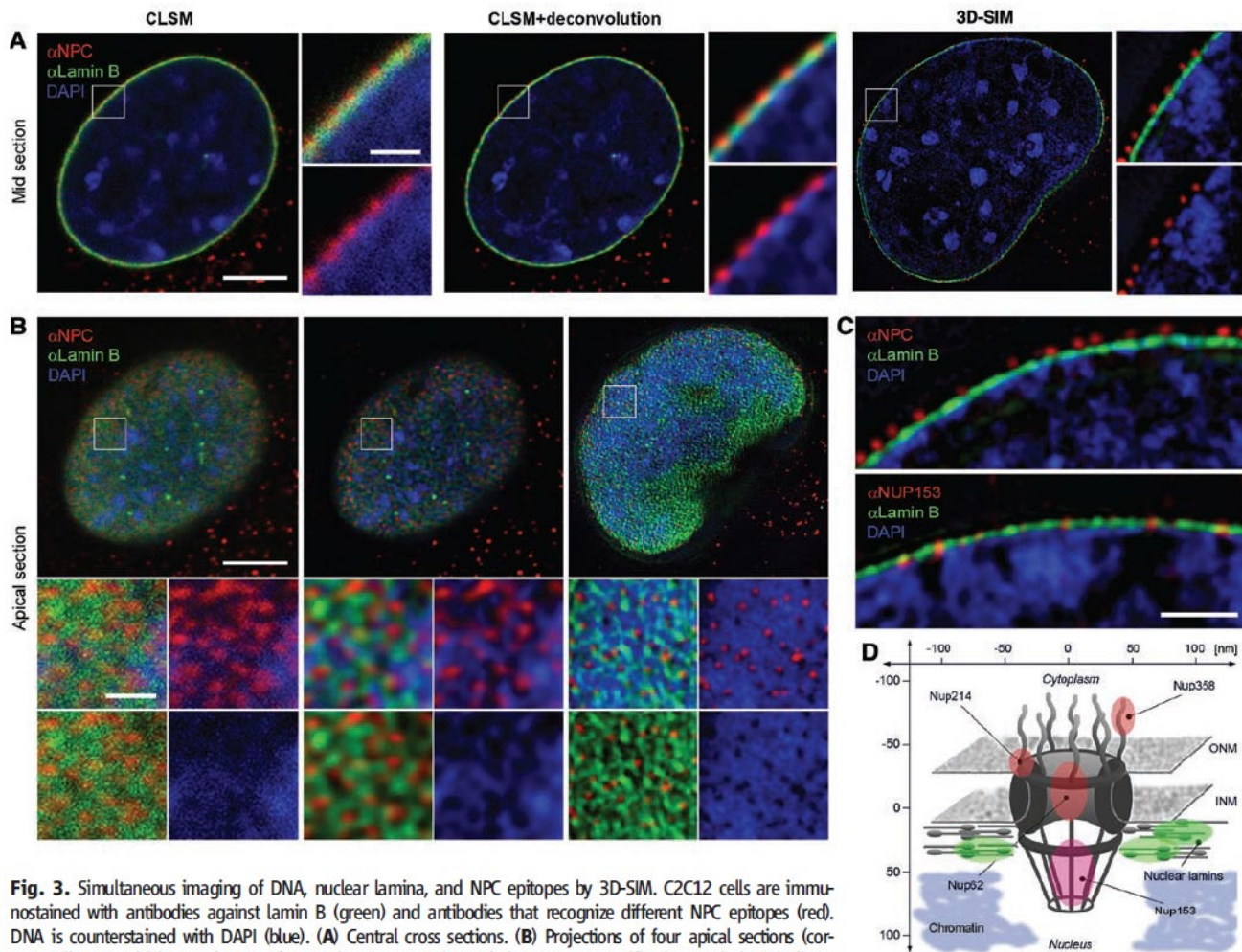
Fig. 3. Simultaneous imaging of DNA, nuclear lamina, and NPC epitopes by 3D-SIM. C2C12 cells are immunostained with antibodies against lamin B (green) and antibodies that recognize different NPC epitopes (red). DNA is counterstained with DAPI (blue). (**A**) Central cross sections. (**B**) Projections of four apical sections (corresponding to a thickness of 0.5 μm). Boxed regions are shown below at 4× magnification; scale bars indicate 5 μm and 1 μm, respectively. (A) CLSM and deconvolution still show partially overlapping signals. In contrast, with 3D-SIM the spatial separation of NPC, lamina, and chromatin and chromatin-free channels underneath nuclear pores are clearly visible. (B) Top view on the nuclear envelope. Whereas CLSM fails to resolve close nuclear pores, 3D-SIM shows clearly separated NPC signals at voids of peripheral chromatin and surrounded by an irregular network of nuclear lamina. (**C**) Mid sections comparing stainings with an antibody that mainly reacts with Nup214, Nup358, and Nup62 (αNPC) and one specifically recognizing Nup153 (αNup153). The αNPC signal is above the lamina (140 ± 8 nm), whereas the αNup153 pore signal is at the same level as the lamina (−15 ± 20 nm). Scale bars 1 μm. (**D**) Schematic outline of the NPC, showing the relative position of Nup proteins and surrounding structures. ONM, outer nuclear membrane; INM, inner nuclear membrane.

Super-resolution video microscopy of live cells by structured illumination

Peter Kner[1,2,7,8], Bryant B Chhun[1,8], Eric R Griffis[3,4], Lukman Winoto[5] & Mats G L Gustafsson[5,6]

Structured-illumination microscopy can double the resolution of the widefield fluorescence microscope but has previously been too slow for dynamic live imaging. Here we demonstrate a high-speed structured-illumination microscope that is capable of 100-nm resolution at frame rates up to 11 Hz for several hundred time points. We demonstrate the microscope by video imaging of tubulin and kinesin dynamics in living *Drosophila melanogaster* S2 cells in the total internal reflection mode.
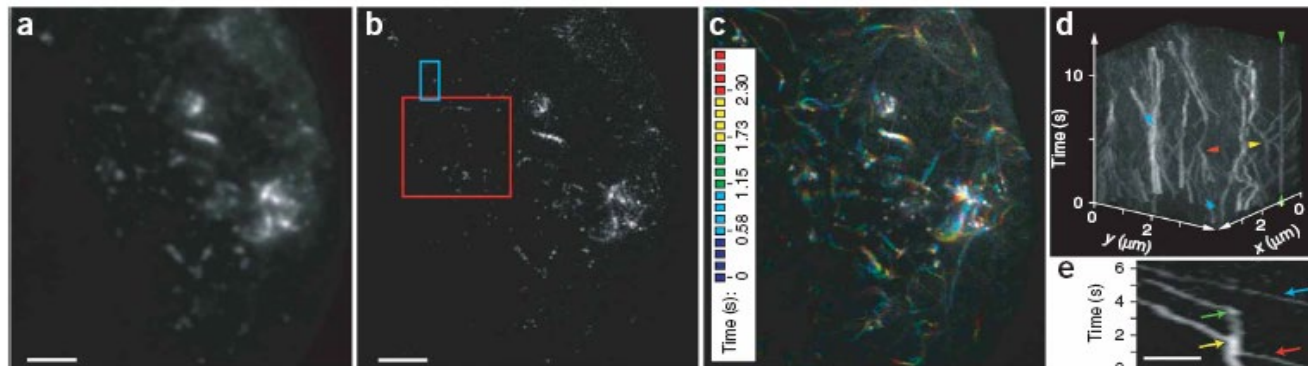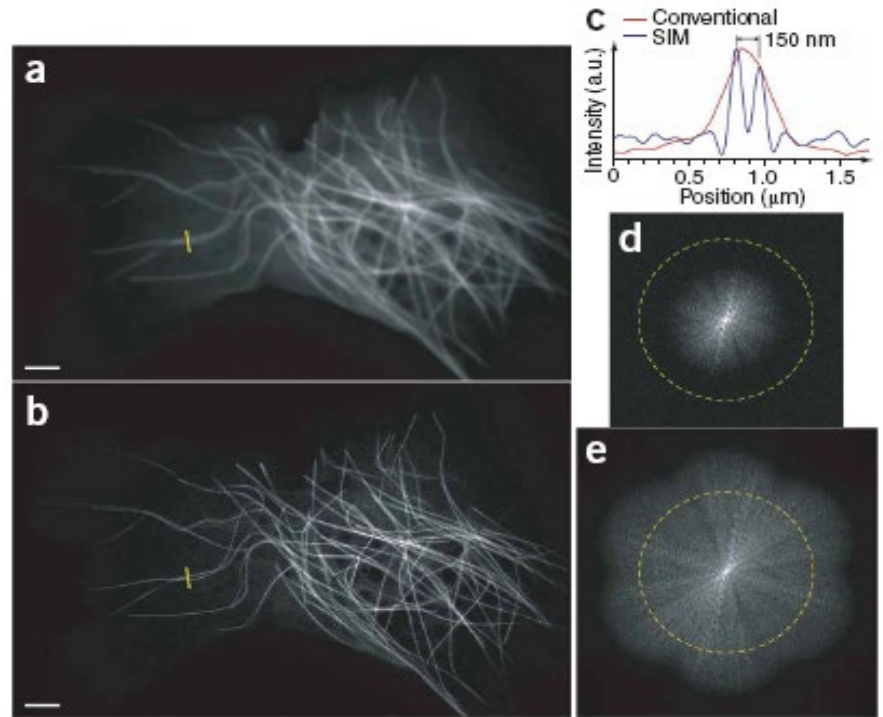
Light sheet fluorescence microscopy
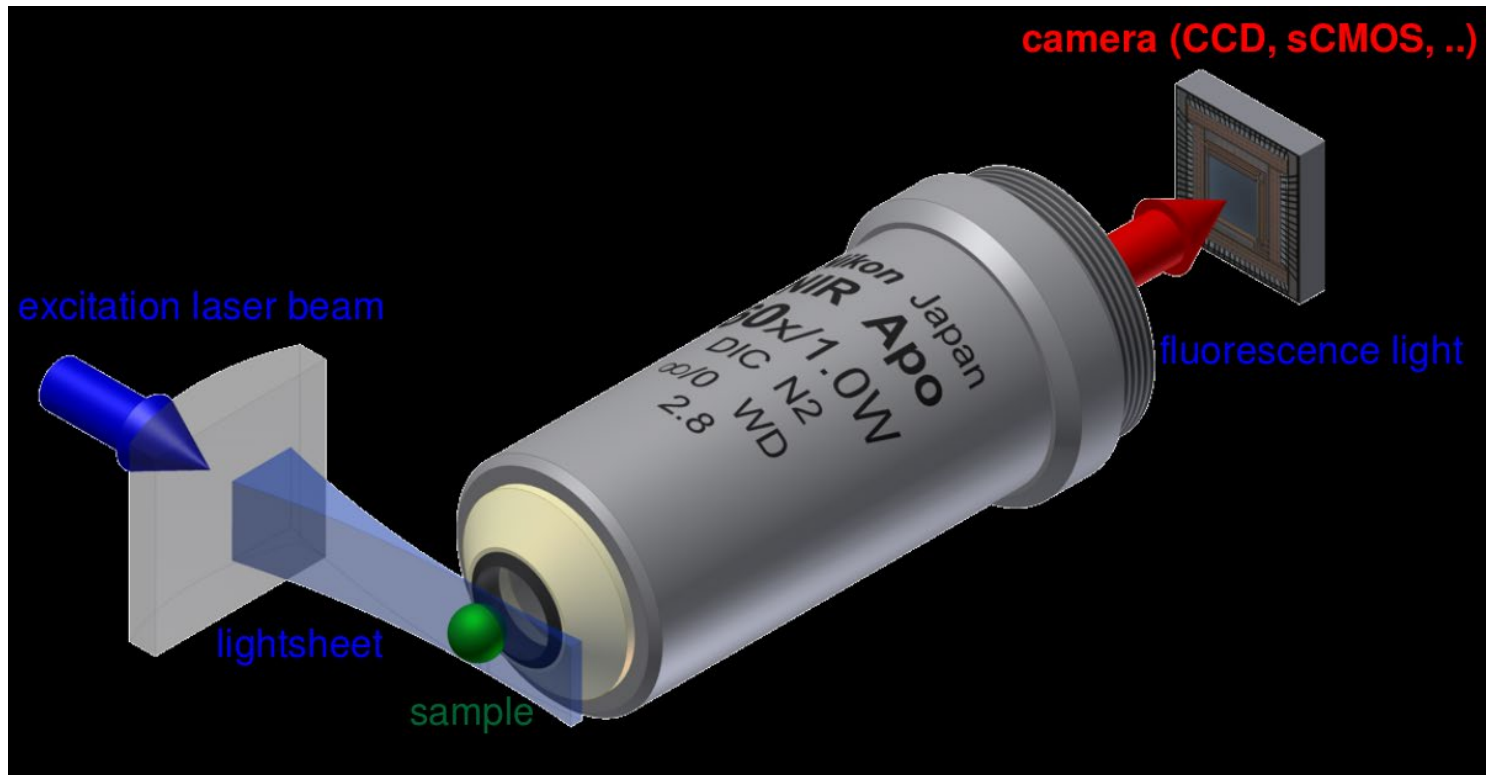
Rapid three-dimensional isotropic imaging of living cells using Bessel beam plane illumination

Thomas A Planchon[1,6], Liang Gao[1,6], Daniel E Milkie[2], Michael W Davidson[3], James A Galbraith[4], Catherine G Galbraith[5] & Eric Betzig[1]

Figure 2 | Modes of Bessel beam plane illumination microscopy. (a) Wide-field illumination geometry (left) and maximum-intensity projection (MIP) in the *x–z* plane (right; *z*, detection axis) from a 3D image stack of a fixed human osteosarcoma cell (U2OS) transfected with plasmids encoding mEmerald fused to human pyruvate dehydrogenase alpha 1 (PDHA1). **(b)** Bessel sheet mode geometry (left), showing fluorescence excitation from Bessel side lobes (light green) as well as the central peak (dark green), and *x–z* plane MIP (right) from same cell as in **a**. **(c,d)** Bessel SI mode geometry, showing periodic Bessel beam excitation pattern (left) and *x–z* plane MIPs with single-harmonic **(c)** and multiharmonic **(d)** excitation (right). **(e)** Two-photon excitation (TPE) Bessel sheet mode geometry (left), showing infrared excitation (red) of fluorescence in the central peak (green), with negligible fluorescence in side lobes and *x–z* plane MIP from a cell (right) similar to those in **a–d**. **(f)** Volume rendering in the multiharmonic SI mode (9 phases, 2.4 μm period) of mEmerald-tagged microtubule associated protein 4 (MAP4) in a live U2OS cell. **(g)** Volume rendering in the TPE sheet mode of mEmerald-labeled mitochondria in a live pig kidney epithelial cell (LLC-PK1 cell line). Insets in **f** and **g** show MIPs along orthogonal axes of the cubical volumes shown. Scale bars, 10 μm except 3 μm in insets.
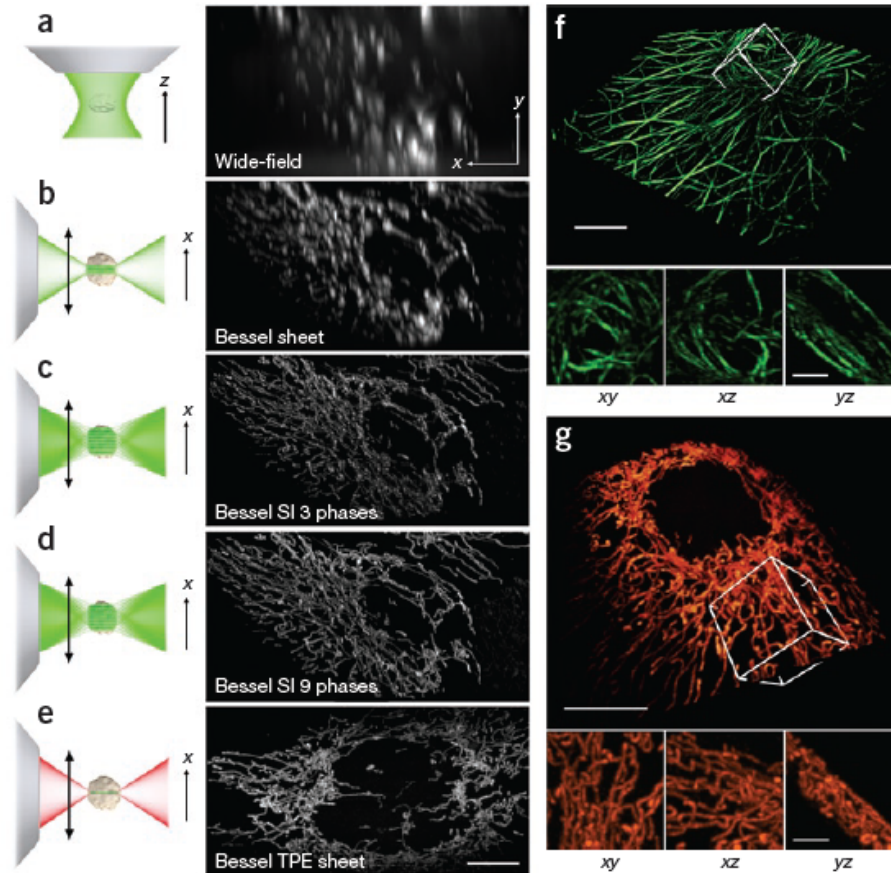
Figure 4 | Three-dimensional isotropic imaging of live-cell dynamics. (**a**) Images of ER in a live U2OS cell, visualized in the Bessel multiharmonic 9 phase SI mode, over 45 image volumes: representation of a subset of the 321 image planes (brown lines) comprising each volume (top); images from three indicated image planes; and image volumes after 10 and 30 min of observation. (**b**) Filopodia at the apical surface of a live HeLa cell, visualized in the Bessel TPE sheet mode over three consecutive image volumes from 100 such volumes taken at 6-s intervals. Filaments that wave (magenta and yellow arrowheads), extend outward (cyan arrowhead) or retract inward (green arrowhead) are marked. (**c**) African green monkey kidney cell (COS-7) transfected with plasmids encoding mEmerald–c-Src, demonstrating retrograde flow of membrane ruffles (left) and vacuole formation by macropinocytosis (right; arrowheads) in an exemplary plane in a translucent cell view (top). All data were extracted from 73 image stacks taken at 12-s intervals. Scale bars, 5 μm (**a**,**b**) and 10 μm (**c**).
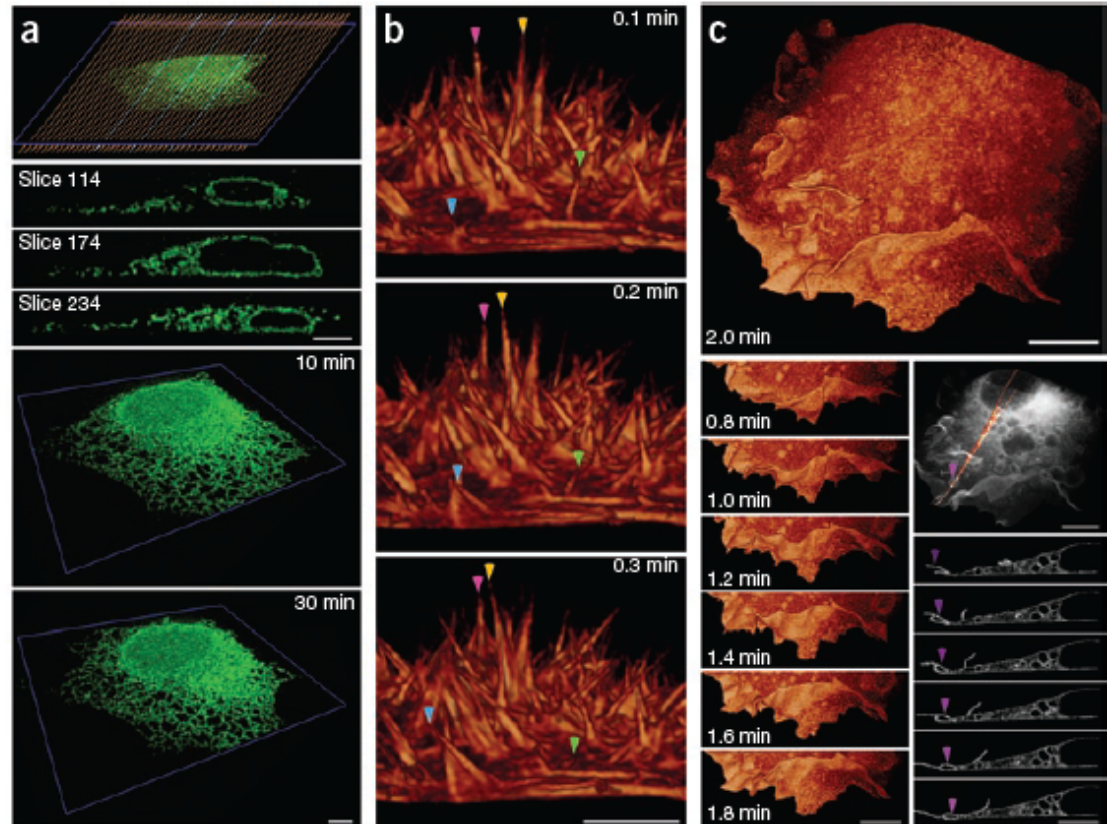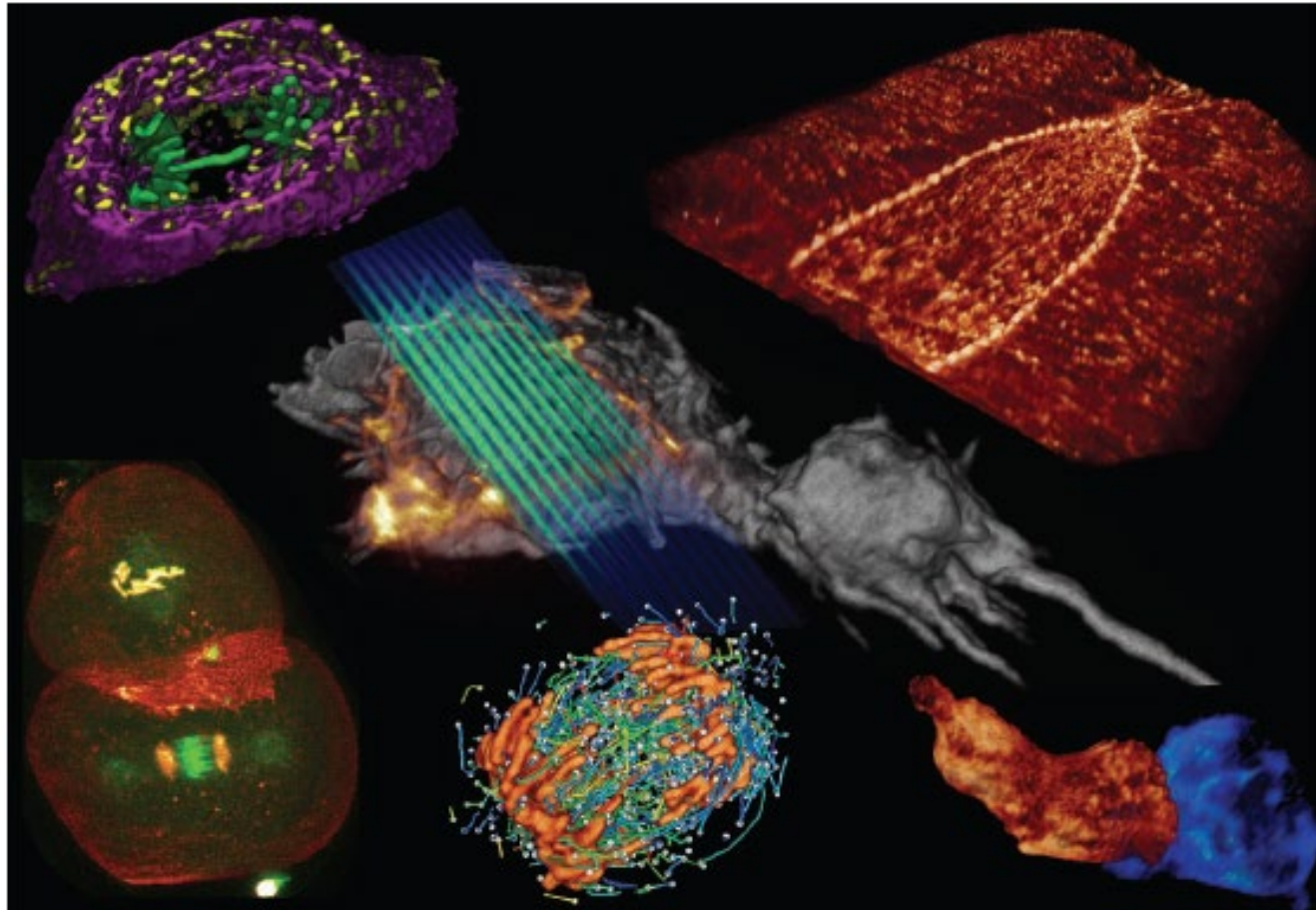
Lattice light-sheet microscopy. An ultrathin structured light sheet (blue-green, center) excites fluorescence (orange) in successive planes as it sweeps through a specimen (gray) to generate a 3D image. The speed, noninvasiveness, and high spatial resolution of this approach make it a promising tool for in vivo 3D imaging of fast dynamic processes in cells and embryos, as shown here in five surrounding examples.

Fig. 1. Methods of light-sheet microscopy. (**A**) The traditional approach, where a Gaussian beam is swept across a plane to create the light sheet. a.u., arbitrary units. (**B**) A Bessel beam of comparable length produces a swept sheet with a much narrower core but flanked by sidebands arising from concentric side lobes of the beam. (**C** and **D**) Bound optical lattices (compare with movie S1) create periodic patterns of high modulation depth across the plane, greatly reducing the peak intensity and, as we have found, the phototoxicity in live cell imaging. The square lattice in (C) optimizes the confinement of the excitation to the central plane, and the hexagonal lattice in (D) optimizes the axial resolution as defined by the overall PSF of the microscope. The columns in (A) to (D) show the intensity pattern at the rear pupil plane of the excitation objective; the cross-sectional intensity of the pattern in the *xz* plane at the focus of the excitation objective (scale bar, 1.0 μm); the cross-sectional intensity of the light sheet created by dithering the focal pattern along the *x* axis (scale bar, 1.0 μm); and the *xz* cross section of the overall PSF of the microscope (scale bar, 200 nm). (**E**) Model showing the core of our microscope, with orthogonal excitation (left) and detection (right) objectives dipped in a media-filled bath (compare with fig. S4). (**F**) Higher magnification view, showing the excitation (yellow) and detection (red) light cones, which meet at a common focus within a specimen that is either mounted or cultured onto a cover glass within the media. The *x*, *y*, and *z* directions are indicated. The *s*-axis defines the direction the specimen moves from image plane to image plane. (**G**) Representation of a lattice light sheet (blue-green) intersecting a cell (gray) to produce fluorescence (orange) in a single plane. The cell is swept through the light sheet to generate a 3D image (compare with movie S2).

Optical Clearing
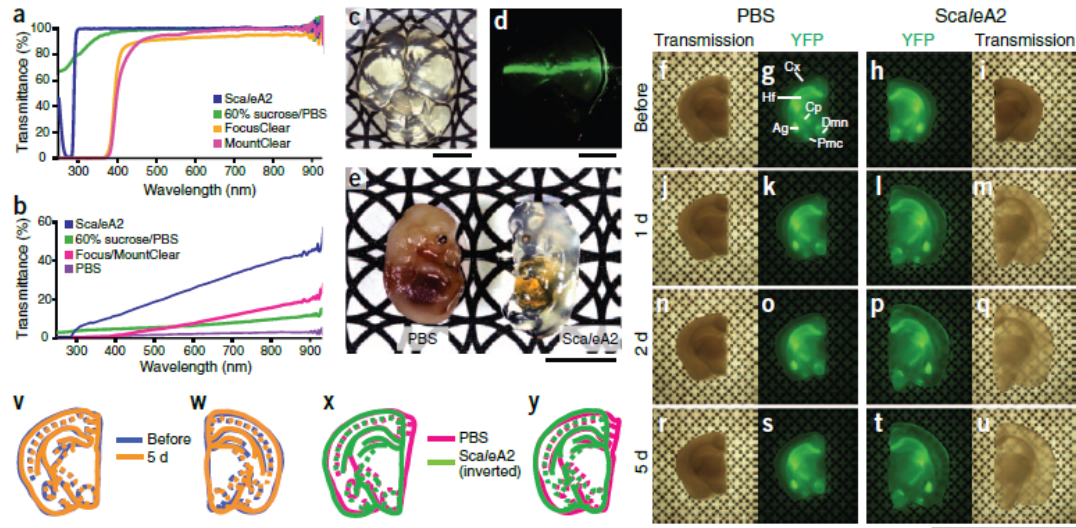
Whole-Brain Imaging with Single-Cell Resolution Using Chemical Cocktails and Computational Analysis
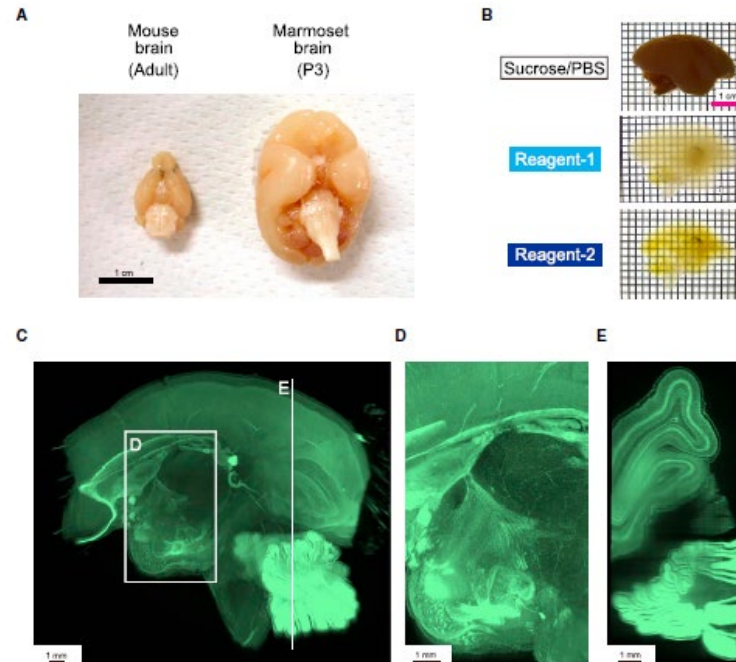
Whole-body and Whole-Organ Clearing and Imaging Techniques with Single-Cell Resolution: Toward Organism-Level Systems Biology in Mammals

Figure 1. Steps for Organism-Level Systems Biology
Overview of the proposed research scheme, aiming at organism-level systems biology in mammal by comprehensive cell detection and analysis of whole-organ/body. This is achieved by optical tissue clearing and imaging (or alternatively by sectioning tomography without clearing) of properly labeled specimens. Data are analyzed to extract biological information, for which high-spec PC equipment is generally needed.

Whole-Body Imaging with Single-Cell Resolution by Tissue Decolorization
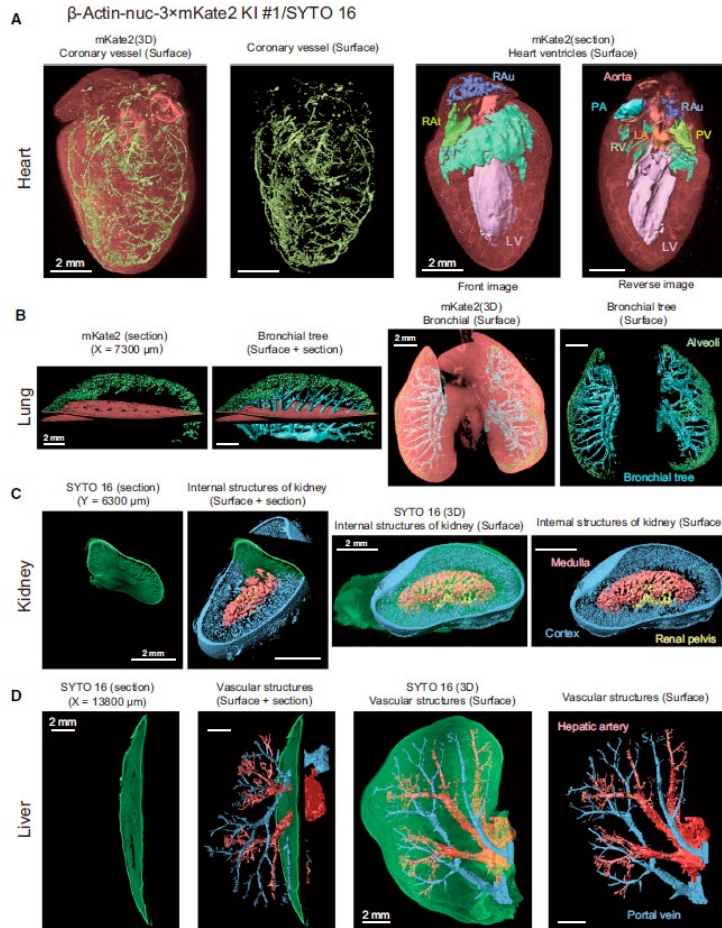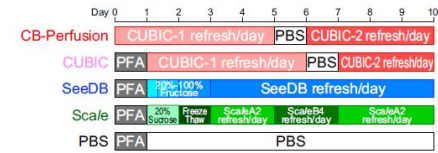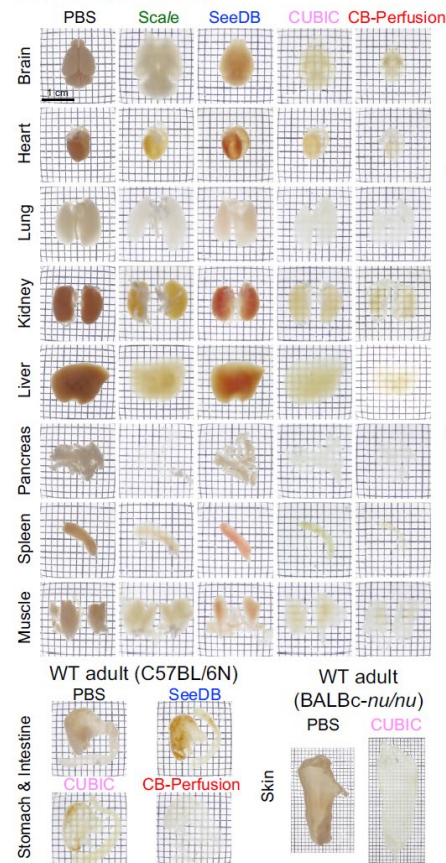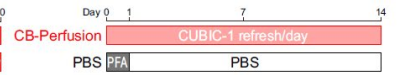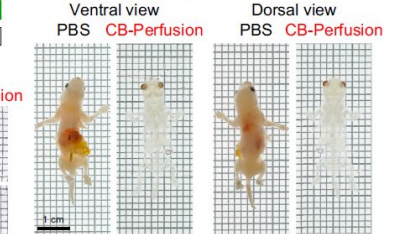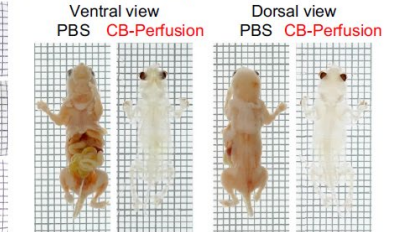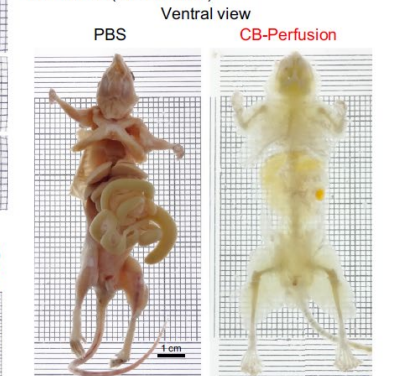
Structural and molecular interrogation of intact biological systems
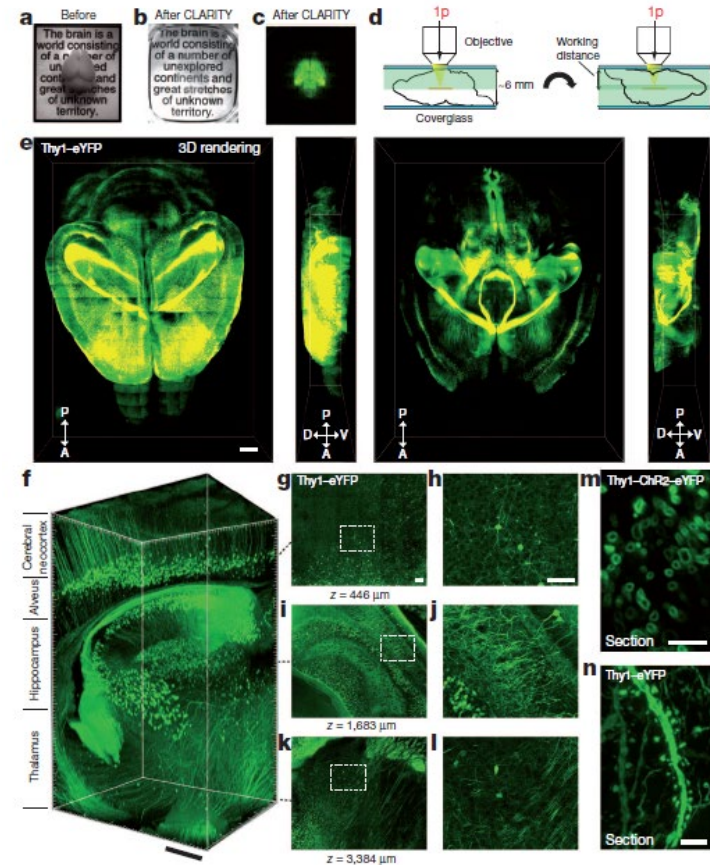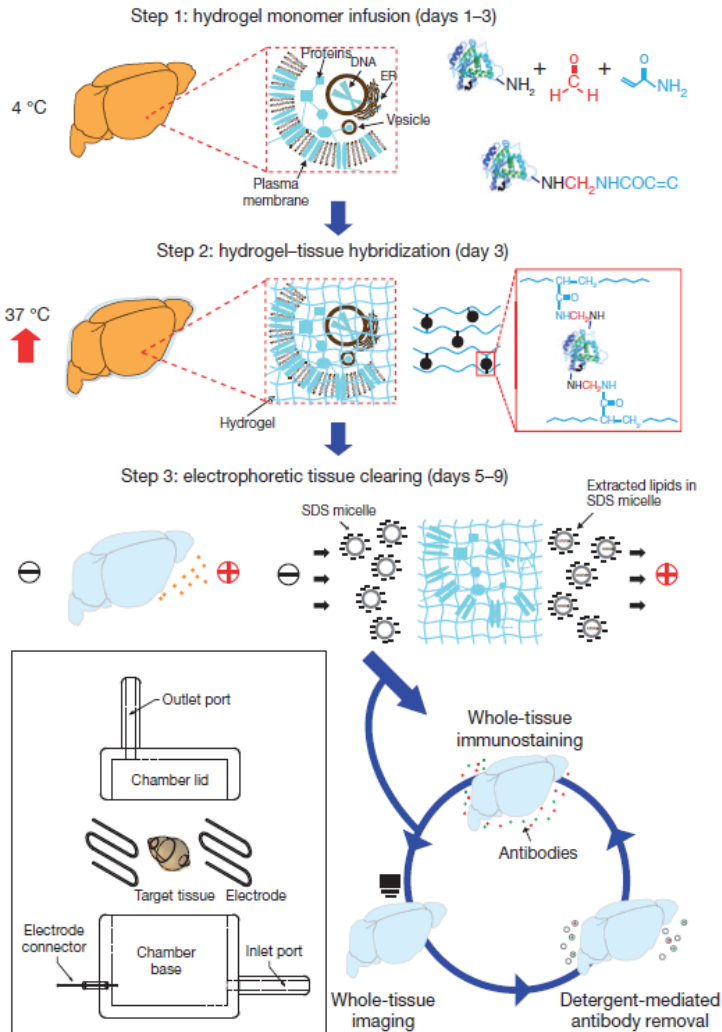
Expansion microscopy

Fei Chen,[1*] Paul W. Tillberg,[2*] Edward S. Boyden[1,3,4,5,6]†
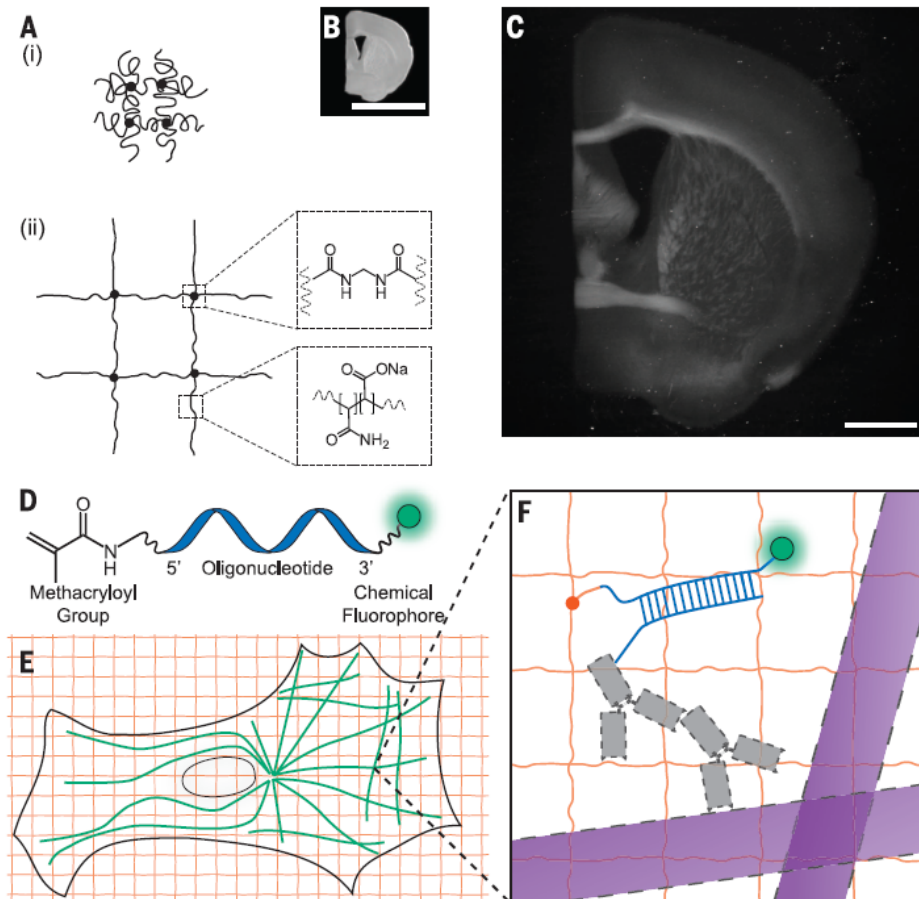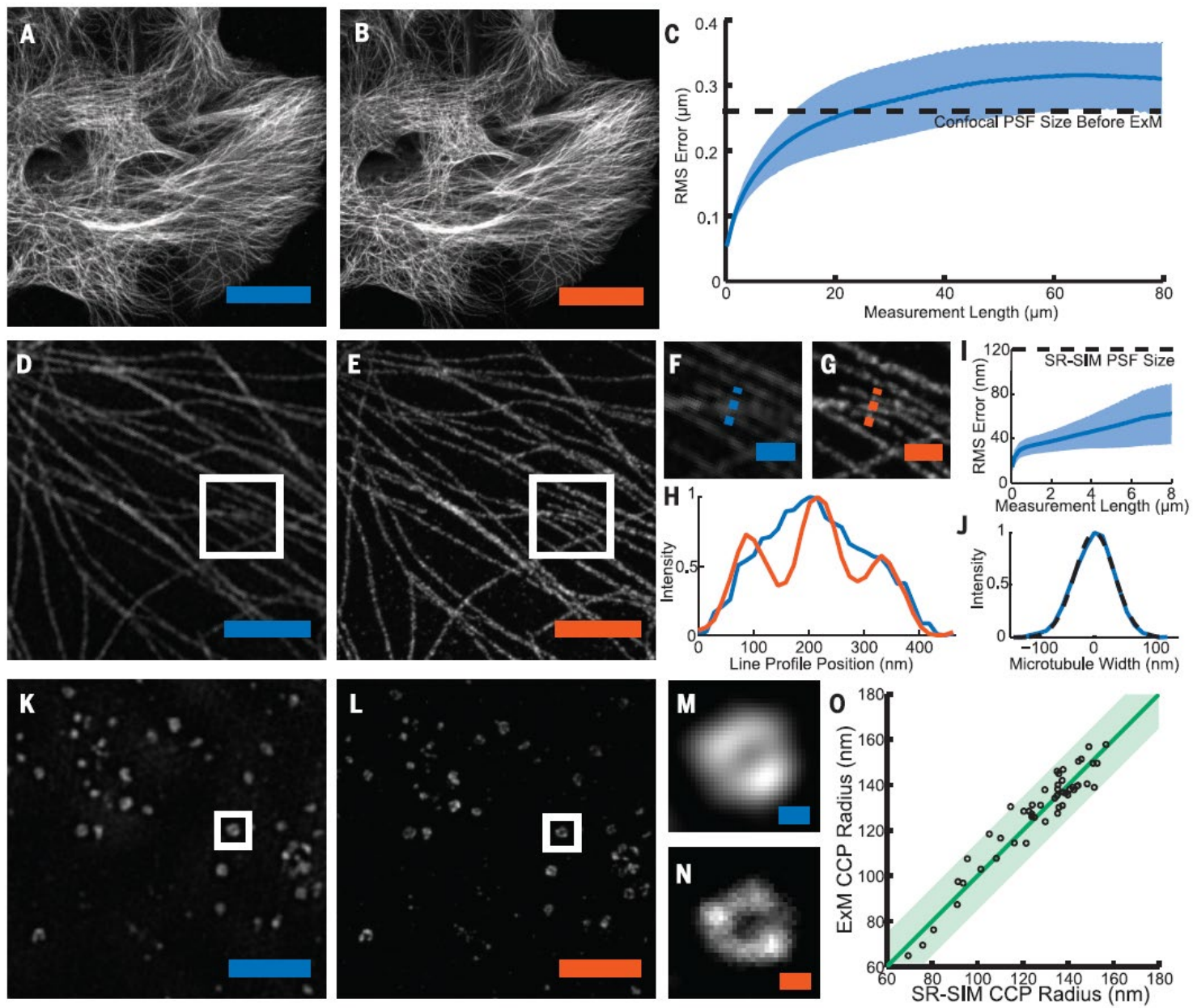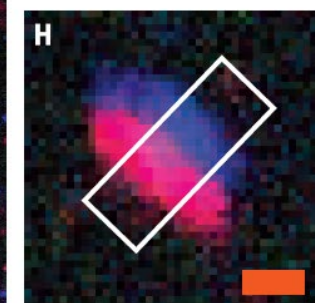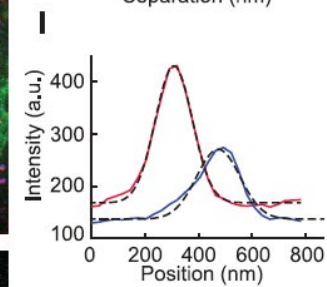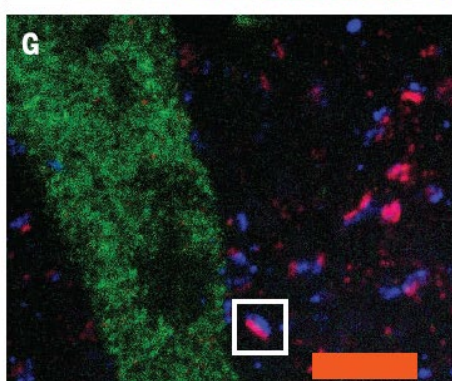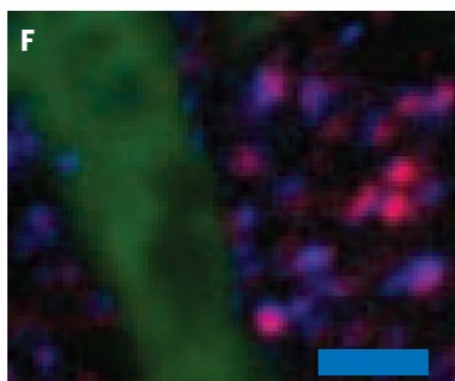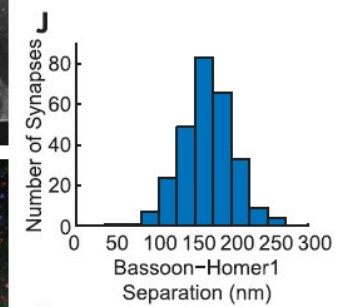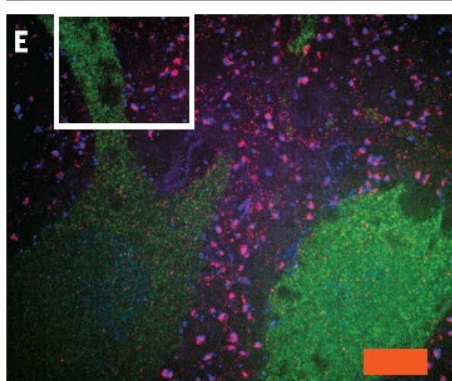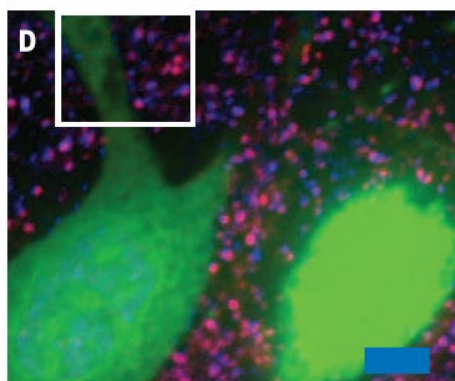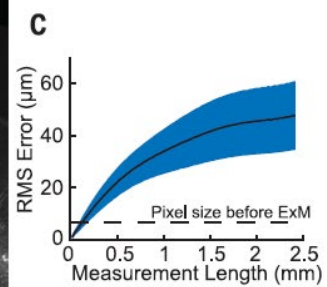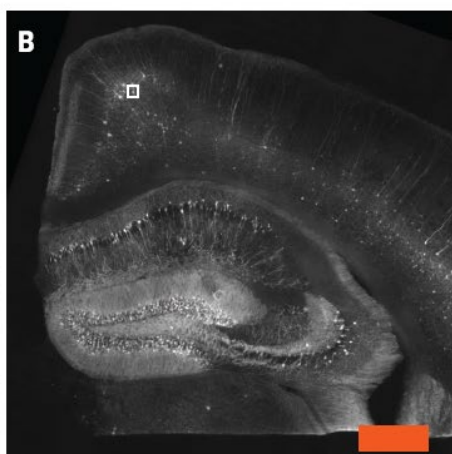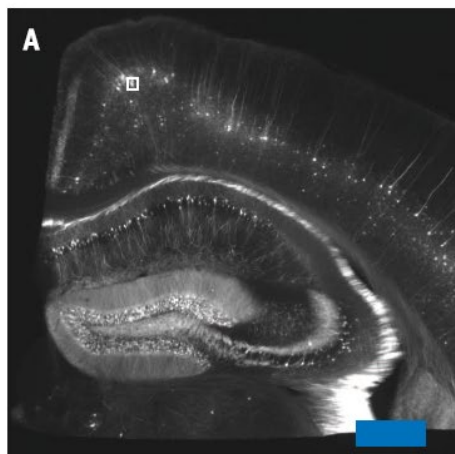
IMAGING TECHNIQUES

Cortical column and whole-brain imaging with molecular contrast and nanoscale resolution

A DC3 PNs

Cell 1
Cell 2
Cell 3

CA

DC3 PN Boutons

Confocal ExLLSM

LH

B
Volume (μm³)

Cell1
Cell2
Cell3

CA   LH

C
DC3 PNs (*D1*)
DC3 PNs (*D2*)
DC3 PNs (*D3*)
DC3 PNs (*D4*)
DC3 PNs (*D5*)
nc82 (*D2*)

CA

D # of Boutons in CA

Cell1
Cell2
Cell3

n = 10   n = 12   n = 10   n = 9   n = 7

D1   *D2*   *D3*   *D4*   *D5*

E
Volume (μm³)

Cell1
Cell2
Cell3

D1   *D2*   *D3*   *D4*   *D5*

F

FB

PPM3 cluster
DANs

NO   EB

G
PPM3-EB   PPM3-FB3

2 cells   2 cells

PPM3-FB2-NO   PPM3-FB3-NO-a and b

2 cells   2 cells

A DAN-assoc nc82

Local Density (puncta/µm³)

All nc82

B

C

D
DAN-assoc nc82
nonDAN-assoc nc82

Domain Density (puncta/µm³)

% DAN assoc

ME (L), ME (R), LOP (L), LOP (R), LO (L), LO (R), OTU (L), OTU (R), VLPR (L), VLPR (R), LH (L), LH (R), CA (L), CA (R), MB α2 α'2 (L), MB α2 α'2 (R), MB α3 (L), MB α3 (R), MB α'3 (L), MB α'3 (R), MB γ1 (L), MB γ1 (R), ATL (L), ATL (R), PB, EB, FB, NO (L), NO (R), LAL (L), LAL (R), SP (L), SP (R)

E DANs + DAN-assoc nc82

CA (R)   PB   CA (L)

PB

ME (R)   LOP (R)   LO (R)

FB

LO (L)   LOP (L)   ME (L)

NO (R)   NO (L)   EB

EB

Spatial Biology

Spatial Biology is an interdisciplinary research field that focuses on the study of biological systems in relation to their spatial organization and distribution at various scales, ranging from molecular to cellular, tissue, and organism levels. This field combines advanced imaging techniques, computational methods, and molecular biology approaches to investigate the spatial arrangement of biomolecules, cells, and tissues, and how these spatial relationships influence biological functions, processes, and interactions.

GPT4-4

Directions of Spatial Biology

Advanced Imaging Techniques: Techniques such as super-resolution microscopy, cryo-electron microscopy, and light-sheet microscopy will be further refined and expanded, allowing for greater resolution, sensitivity, and speed in imaging cellular structures and molecular interactions.

Integration of Omics Data: Combining spatial biology with other omics data types, such as genomics, transcriptomics, proteomics, and metabolomics, will enable a more comprehensive understanding of the spatial organization of biological systems and their functional consequences.

Spatial Analysis and Computational Methods : advanced computational methods and tools for data analysis, visualization, and interpretation. Machine learning and artificial intelligence algorithms will play a crucial role in processing and understanding these complex data sets.

Single-Cell Spatial Analysis

Organoid and 3D Culture Systems

In Vivo Imaging and Therapeutics:

Applications of Spatial Biology

Drug Discovery: Spatial biology can be used to identify drug targets and understand their spatial organization, expression, and function within cells and tissues. This can facilitate the development of drugs that target specific cellular components, pathways, or interactions, leading to more effective and targeted therapies.

Diagnostics: Spatial biology can help identify disease-specific spatial patterns or biomarkers, which can be used for the early detection, diagnosis, and monitoring of diseases such as cancer, neurological disorders, and infectious diseases.

Personalized Medicine: Understanding the spatial organization of cells and tissues in individual patients can lead to the development of personalized treatment strategies tailored to their unique biological context. Spatial biology can inform decisions regarding drug selection, dosage, and administration, as well as the identification of patient subpopulations that may respond differently to specific therapies.

Tissue Engineering and Regenerative Medicine: Spatial biology provides insights into tissue organization, development, and repair, which can be applied to tissue engineering and regenerative medicine. This information can guide the design of artificial tissues and organs, as well as the development of strategies to promote tissue regeneration and repair following injury or disease.

Spatial transcriptomics: paving the way for tissue-level systems biology

Andreas E Moor and Shalev Itzkovitz

Current Opinion in Biotechnology
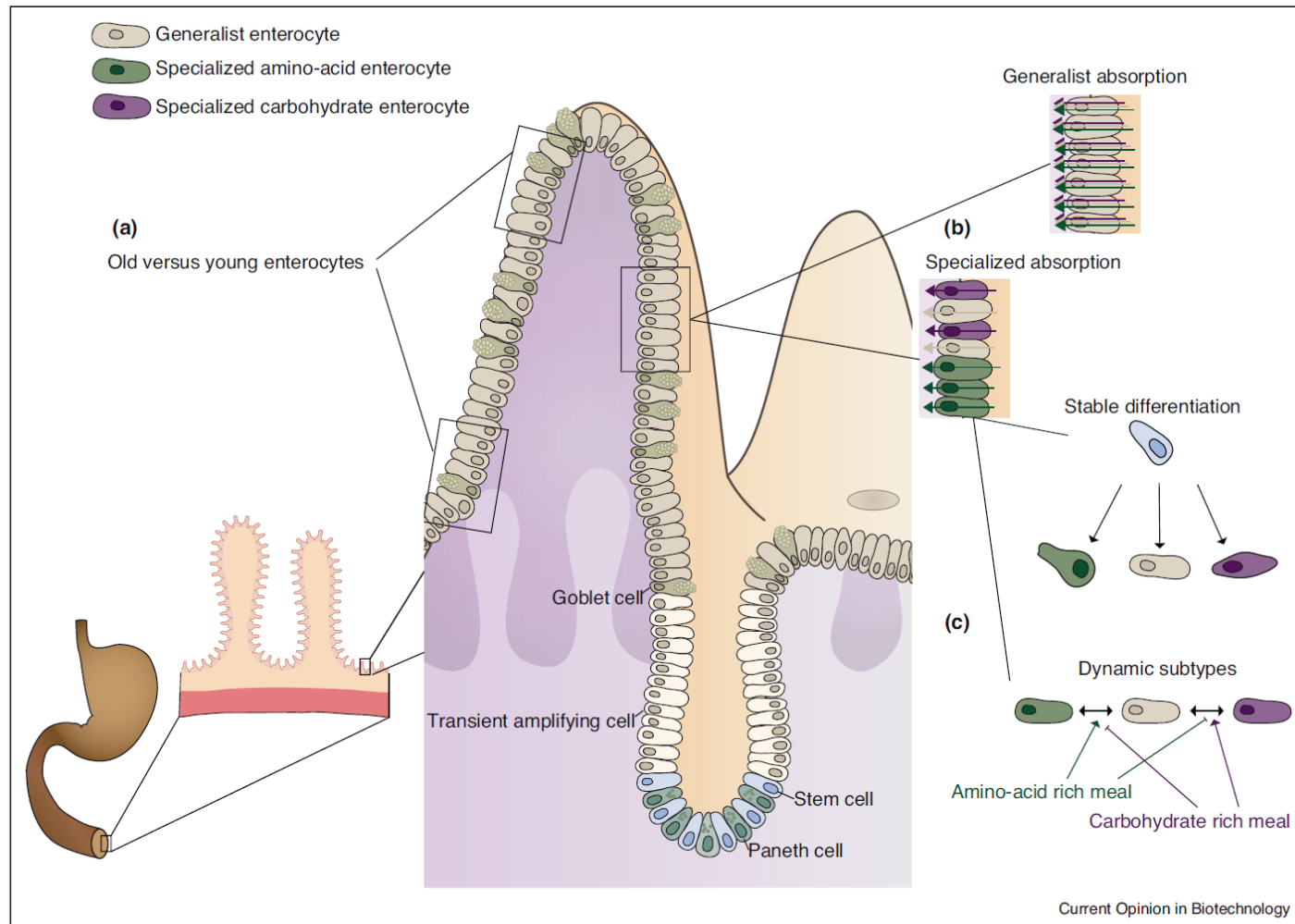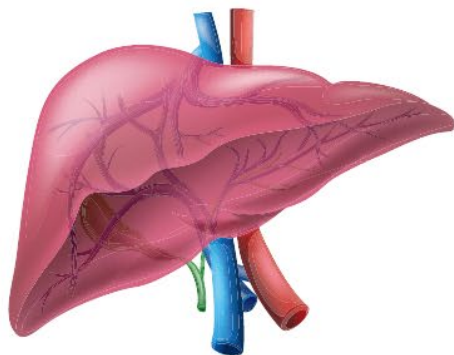
Liver lobule

Spatial divison of labor

Layer 3

Layer 2

Layer 1

Portal artery

Portal vein

Bile duct

Central vein

(a) smFISH-based methods

(1)

(2)

(3)

(4)

— encoding probe
🔴 readout probe (active)
⚫ readout probe (inactivated)
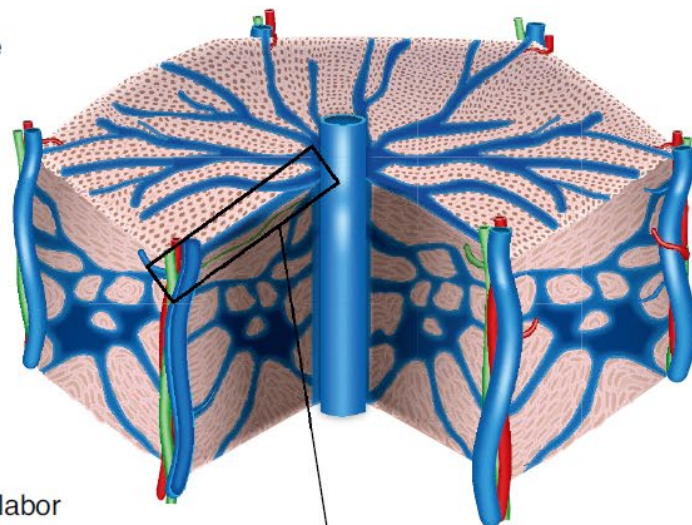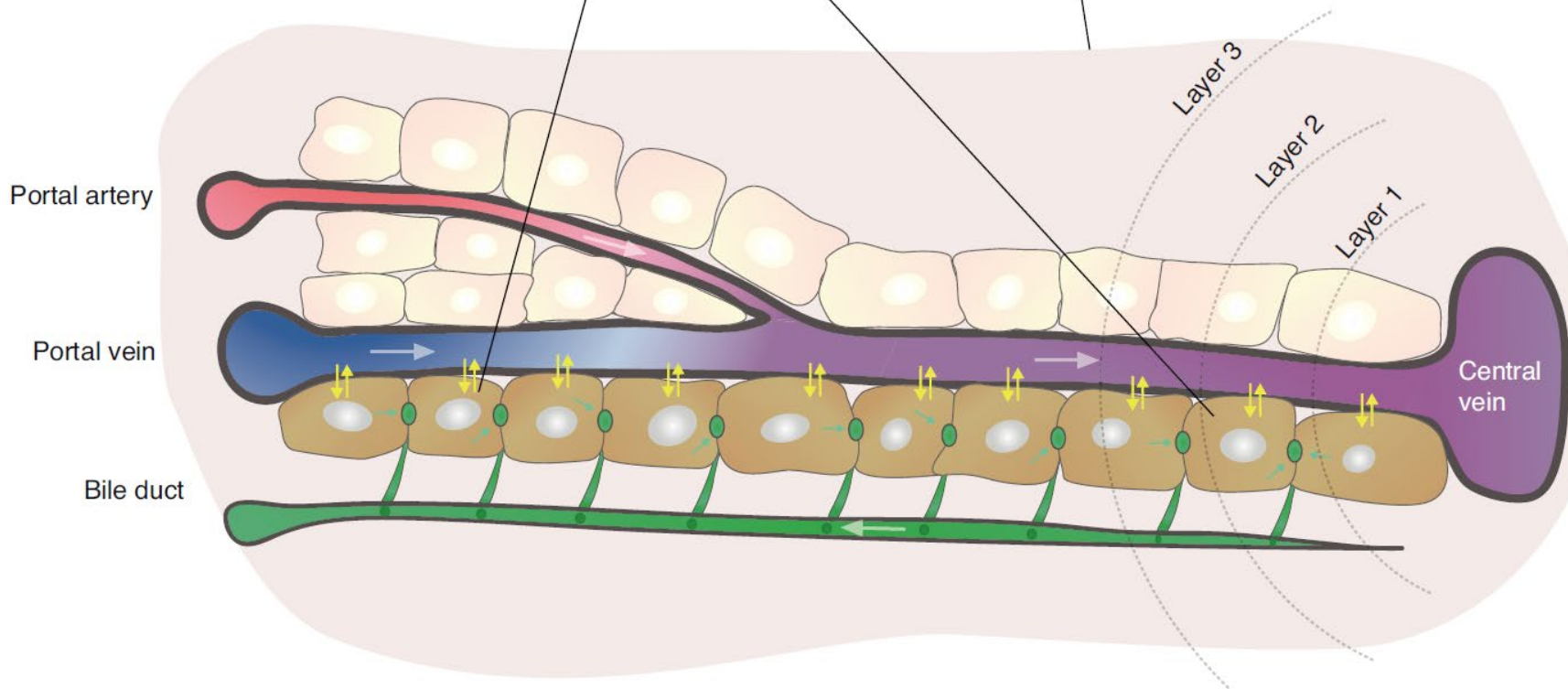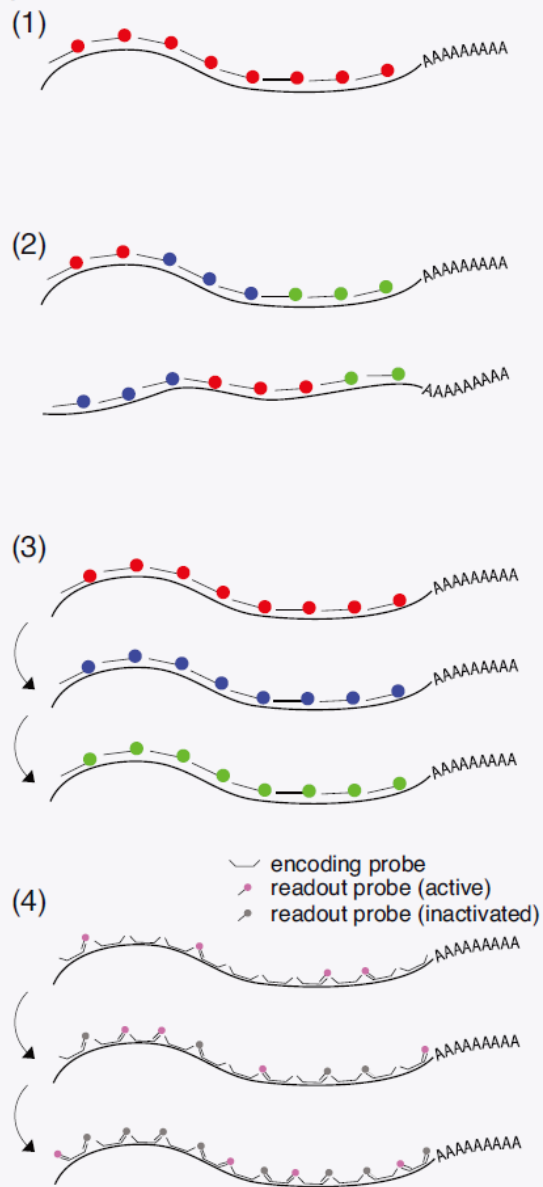
(b) sequencing-based methods

(1) mRNA 1
mRNA 2

(2) cDNA1
cDNA2

(3) cycle 1 cycle 2 cycle 3 cycle 4 cycle n

A A C T C
G T A G G

AACTC
GTAGG

(c)

(1)

(2)

(3)
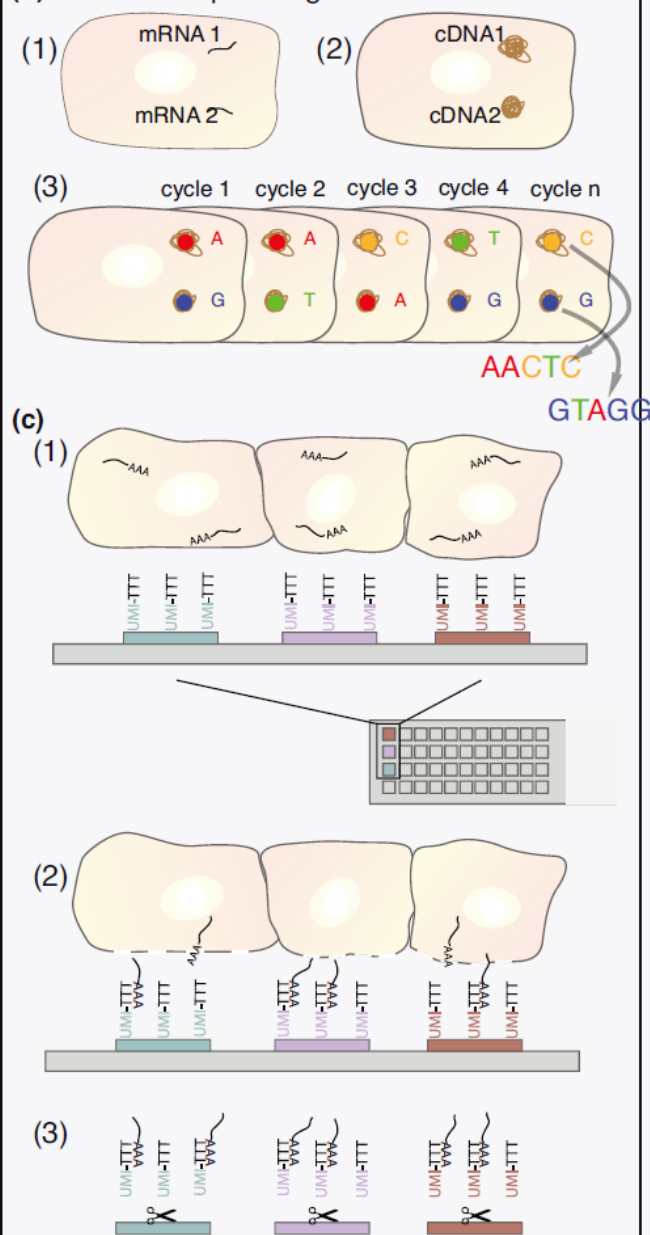
(d) tissue reference map-based methods

(1)

(2)

(3)

(4)

Current Opinion in Biotechnology
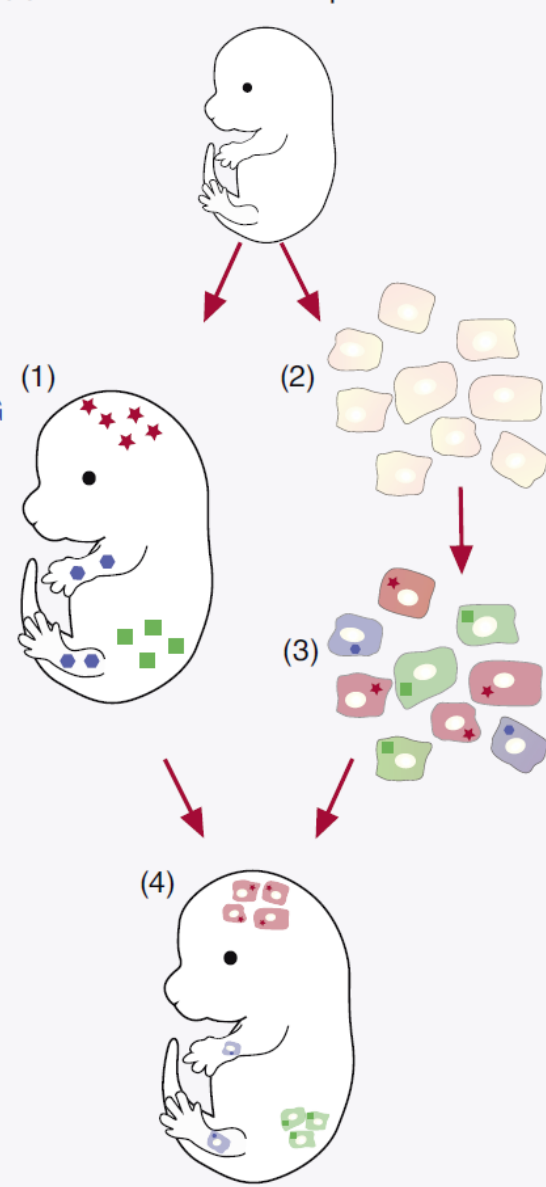
mRNA

mRNA exists in a variation of sizes, quantified by their number of nucleotides. For example, the GFP protein has a size between 300 and 1,000 nucleotides. Conversely, mRNA molecules such as the COVID-19 mRNA vaccine and Cas-9 have sizes between 2,000 and 4,000 nucleotides.
Average length 1200-1500 NTs

```
  1 tacacacgaa taaaagataa caaagatgag taaaggagaa gaactttttca ctggagttgt
 61 cccaattctt gttgaattag atggcgatgt taatgggcaa aaattctctg tcagtggaga
121 gggtgaaggt gatgcaacat acggaaaact tacccttaaa tttatttgca ctactgggaa
181 gctacctgtt ccatggccaa cacttgtcac tactttctct tatggtgttc aatgcttttc
241 aagataccca gatcatatga aacagcatga cttttttcaag agtgccatgc ccgaaggtta
301 tgtacaggaa agaactatat tttacaaaga tgacgggaac tacaagacac gtgctgaagt
361 caagtttgaa ggtgataccc ttgttaatag aatcgagtta aaaggtattg attttaaaga
421 agatggaaac attcttggac acaaaatgga atacaactat aactcacata atgtatacat
481 catggcagac aaaccaaaga atggaatcaa agttaacttc aaaattagac acaacattaa
541 agatggaagc gttcaattag cagaccatta tcaacaaaat actccaattg gcgatggccc
601 tgtccttttta ccagacaacc attacctgtc cacacaatct gccctttcca aagatcccaa
661 cgaaaagaga gatcacatga tccttcttga gtttgtaaca gctgctggga ttacacatgg
721 catggatgaa ctatacaaat aaatgtccag acttccaatt gacactaaag tgtccgaaca
781 attactaaat tctcagggtt cctggttaaa ttcaggctga gactttattt atatatttat
841 agattcatta aaatttttatg aataatttat tgatgttatt aatagggggct atttttcttat
901 taaataggct actggagtgt at
```

GFP
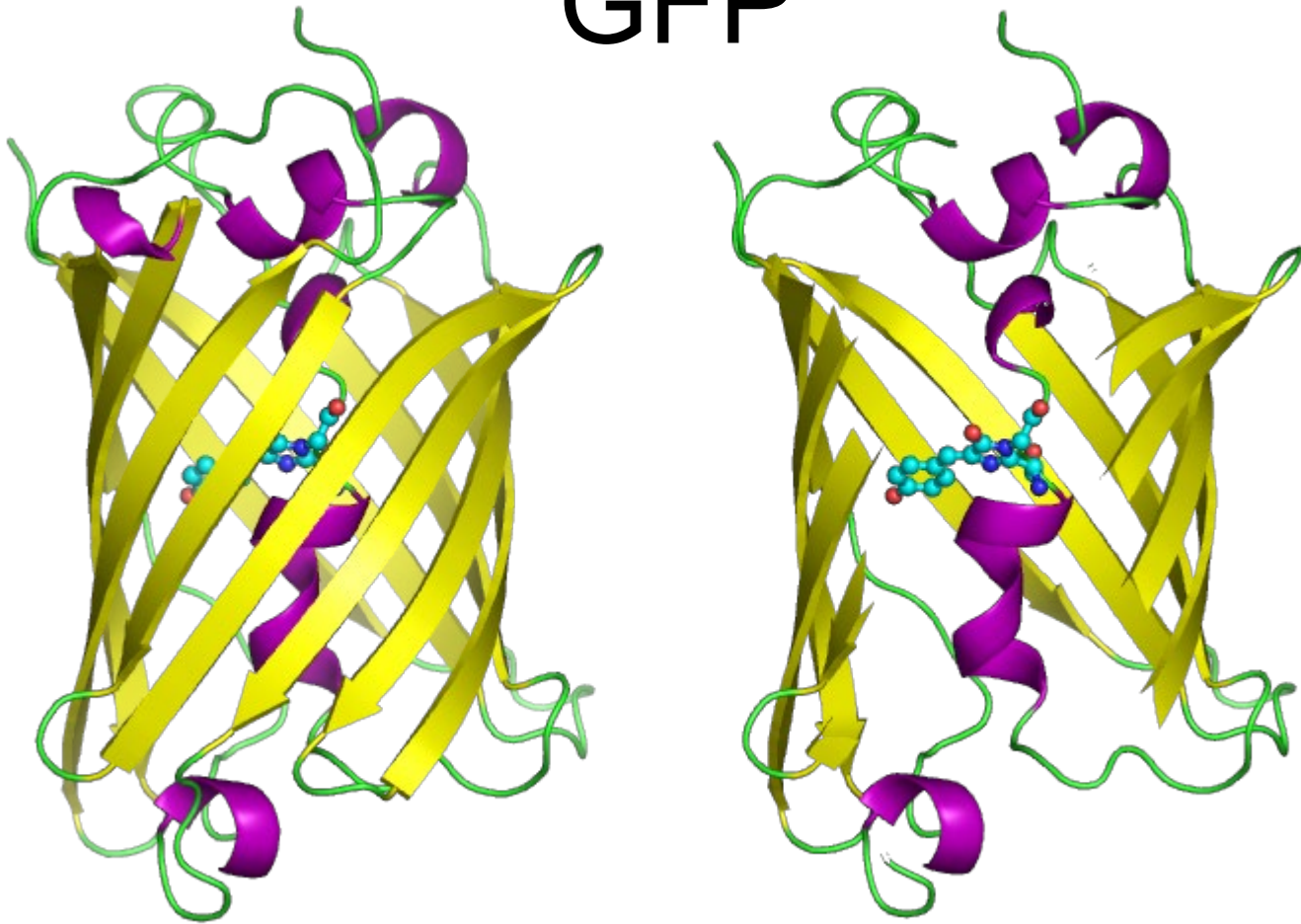
MSKGEELFTGVVPILVELDGDVNGQKFSVSGEGEGDATYGKLTL
KFICTTGKLPVPWPTLVTTFSYGVQCFSRYPDHMKQHDFFKSAMPEGYVQERTIFYKD
DGNYKTRAEVKFEGDTLVNRIELKGIDFKEDGNILGHKMEYNYNSHNVYIMADKPKNG
IKVNFKIRHNIKDGSVQLADHYQQNTPIGDGPVLLPDNHYLSTQSALSKDPNEKRDHM
ILLEFVTAAGITHGMDELYK

FLUORESCENCE IN SITU HYBRIDIZATION (FISH)

Fluorescence in situ hybridization (abbreviated FISH) is a laboratory technique used to detect and locate a specific DNA sequence on a chromosome. In this technique, the full set of chromosomes from an individual is affixed to a glass slide and then exposed to a "probe"—a small piece of purified DNA tagged with a fluorescent dye. The fluorescently labeled probe finds and then binds to its matching sequence within the set of chromosomes. With the use of a special microscope, the chromosome and sub-chromosomal location where the fluorescent probe bound can be seen
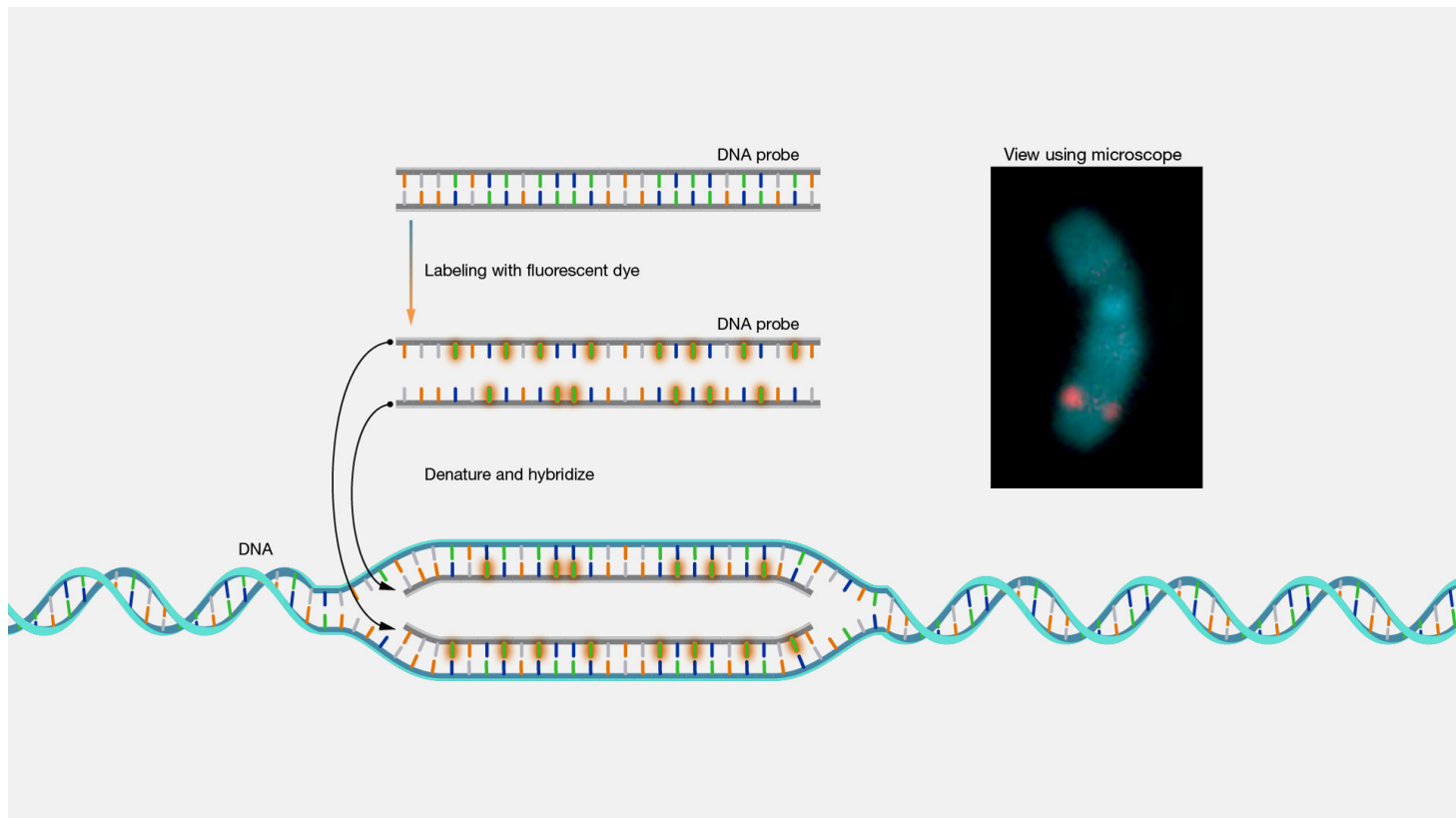
Spatially resolved transcriptomics and beyond

NATURE REVIEWS | GENETICS

a

Legend:
- Fluorescent dye
- smFISH signal
- Primary probe pair
- Pre-amplifier
- Amplifier
- SNV

b
50 nt
20 nt

c
Spatial barcoding

Spectral barcoding

Sequential barcoding

Transcript A   Transcript B

Probe removal and rehybridization

Probe removal and rehybridization

d

e
15–30 nt
28 nt   15–30 nt
50 nt

a

RNA-seq

3D reconstruction

b

UUUUU
AA–AA

AAAAA AAAAA
UUUUU AA–AA
AAAAA
UUUUU

RNA-seq

TIVA tag (before photoactivation)

UUUUU
TIVA tag (after photoactivation)

Cy3–Cy5 FRET pair

CPP (cell entry molecule)

Cy3 fluorescence

Biotin

Streptavidin

c

mRNA

cDNA

SNV identification   Target mRNA visualization

RCP

SBL

G   T   C   A

d

mRNA

Reverse transcription and cDNA crosslinking

NNNNNN

NH
NH

cDNA circularization

Pre-extended primer

NH
NH

RCA

NH
NH

NH₂
NH₂
NH₂

	smFISH	Padlock probes and RCA	Branched FISH	LCM	Microtomy sequencing	TIVA	ISS	FISSEQ	Imaging mass cytometry
Sample	Fixed cells and tissues; purified RNA	Fixed cells and tissues; purified DNA or RNA	Fixed cells and tissues; possibly purified DNA or RNA	Fixed tissues	Fixed and fresh tissues	Live cells	Fixed cells and tissues	Fixed cells and tissues	Fixed tissues
Target	RNA	DNA; RNA	RNA	RNA; DNA; proteins	RNA; possibly DNA and proteins	RNA	RNA	RNA	Proteins
Type	Targeted	Targeted	Targeted	Targeted or non-targeted	Non-targeted	Non-targeted	Targeted	Non-targeted	Targeted
Variable measured	Abundance; SNVs; fusion transcripts; splice variants; subcellular localization	Abundance; SNVs; fusion transcripts; splice variants; subcellular localization	Abundance; subcellular localization	Abundance; possibly SNVs, fusion transcripts and splice variants	Abundance; possibly SNVs, fusion transcripts and splice variants	Abundance; possibly SNVs, fusion transcripts and splice variants	Abundance; possibly SNVs, fusion transcripts and splice variants	Abundance; possibly SNVs, fusion transcripts and splice variants	Abundance; protein modifications
Single-cell?	Yes	Yes	Yes	Yes	No	Yes	Yes	Yes	Yes
Spatial resolution	Subcellular	Subcellular	Subcellular (except the nucleus)	Anatomical or cellular	Anatomical	Cellular	Cellular	Cellular	Subcellular
Morphology assessment	Yes	Yes	Yes	Yes	No	Yes	Yes	Yes	Yes
Throughput (number of cells)	Low to medium	Low to medium	Low to medium	Medium	High	Low	Low to medium	Low to medium	Very high
Throughput (number of genes or proteins)	Low to medium	Low to medium	Medium	High	High	High	Low	High	Low
Estimated efficiency	~90%	~30%	NA	NA	~5–10%	NA	NA	NA	NA
Readout	Microscopy; flow cytometry	Microscopy; flow cytometry	Microscopy; flow cytometry	Microarray; RNA-seq; MS	RNA-seq; possibly MS	RNA-seq	Microscopy	Microscopy	MS
Technical difficulty	Easy	Easy	Easy	Moderately easy	Moderately easy	Moderately difficult	Difficult	Difficult	Difficult

Spatially resolved, highly multiplexed RNA profiling in single cells

Kok Hao Chen,[1]* Alistair N. Boettiger,[1]* Jeffrey R. Moffitt,[1]*
Siyuan Wang,[1] Xiaowei Zhuang[1,2]†
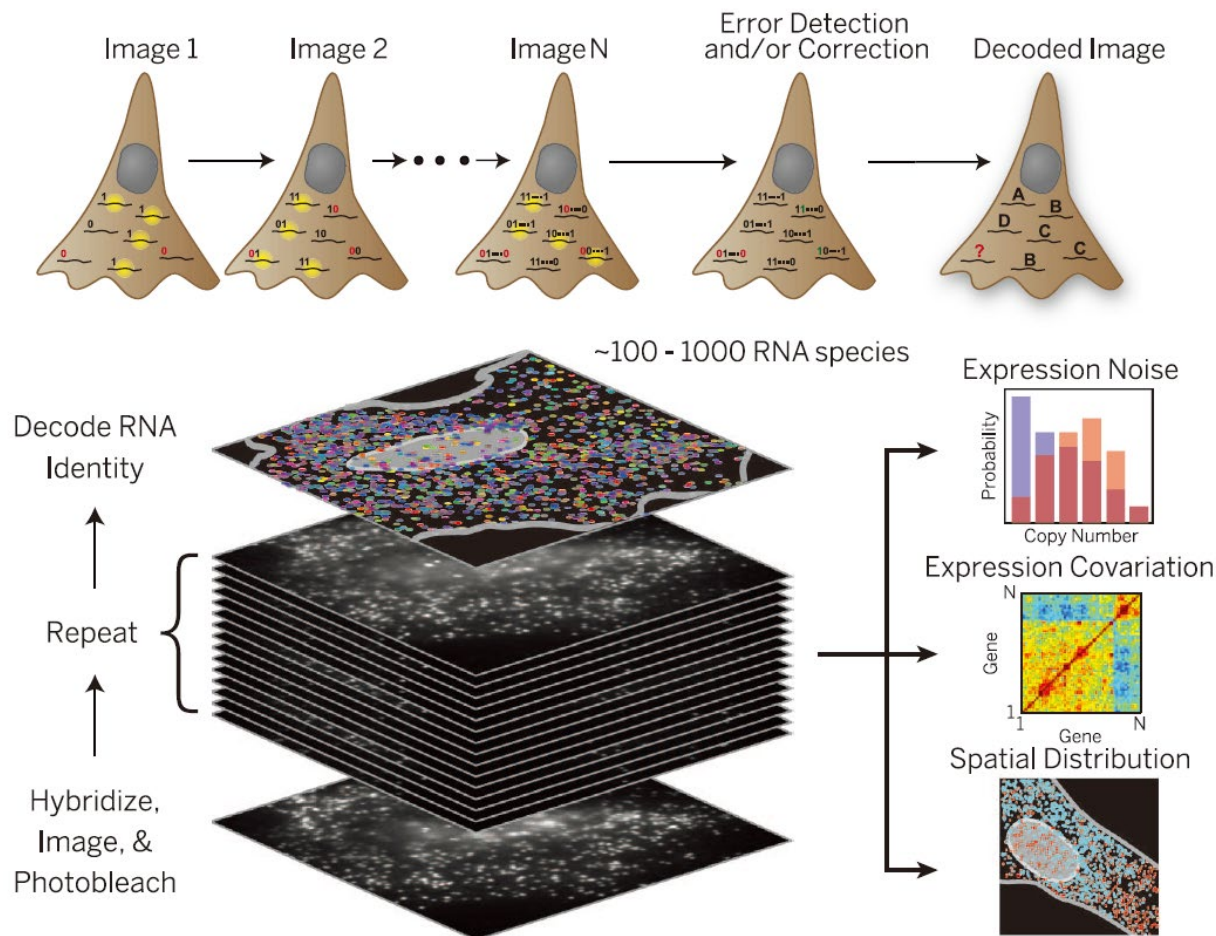
30 nucleotides long, which includes a 20-nucleotide sequence complementary to the target RNA, a 6- to 10-nucleotide readout sequence for the fluorescent readout probe, and a spacer region.

A Image 1 → Image 2 → Image 3 → ● ● ● → Image *N* → Decoded Image

B Number of RNA species vs Number of bits (*N*)

C Calling rate vs Number of bits (*N*)

D Misidentification rate vs Number of bits (*N*)

E

Encoding probes
Readout sequence 1 / Readout sequence 2
Targeting sequence

Encoding probes
Readout sequence 4 / Readout sequence N
Targeting sequence

RNA Species

x96   x96

Encoding hyb

Readout hyb 1

Readout hyb 2

Readout hyb 3

Readout hyb 4

Readout hyb N

Decode

Modified Hamming Distance 4 code
1 1 0 1 ● ● ● 1
0 0 0 0 ● ● ● 1
0 1 1 0 ● ● ● 0
1 0 0 0 ● ● ● 0
0 0 1 0 ● ● ● 1

around 16-48 probes were used per mRNA molecule, depending on the length and sequence of the mRNA. The study used a set of 130 probes targeting 130 different mRNAs in single cells.

In the original MERFISH paper, the authors used a pool of 130 probes, each targeting one of 130 different mRNAs in single cells. For each mRNA species, they designed a set of 16-48 oligonucleotide probes. The exact number of probes for each mRNA varied depending on the length and sequence of the mRNA.

Thus, the total number of probes used in the experiment is the sum of all the individual probe sets for the 130 mRNAs. While the exact total number of probes is not provided in the paper, considering an average of 32 probes per mRNA (midpoint of the 16-48 range), the total number of probes would be approximately:

32 probes/mRNA * 130 mRNA species ≈ 4,160 probes

In the original MERFISH paper, the authors used 16 distinct readout sequences and two spectrally distinct dyes. The 16 readout sequences corresponded to 16 different binary bits in the error-robust barcodes assigned to each mRNA species. Each of these readout sequences was conjugated to a fluorophore in one of two colors.

The authors performed eight sequential imaging rounds, hybridizing and imaging a combination of eight readout probes per round (one for each bit position in the binary barcode). In each imaging round, a subset of the 16 readout sequences was labeled with one of the two colors, resulting in 2^{16} or 65,536 potential binary barcodes.

A hyb 1 | bleach 1 | hyb 2 | hyb 16

10μm

B

10μm

1μm

5 3 6

2 7 4

1

C hyb1 | hyb2 | hyb3 | hyb4

1μm

hyb5 | hyb6 | hyb7 | hyb8

hyb9 | hyb 10 | hyb 11 | hyb 12

hyb 13 | hyb 14 | hyb 15 | hyb 16

A

THBS1 FBN2 FLNA TLN1

10μm

B

-0.2 ▬ 0.2

I

II

C

Group I
Group II

10μm

D

Average gene

Group I

Group II

0.85 0.9 0.95 1 1.05 1.1 1.15
Relative distance to cell edge

Average gene

Group I

Group II

0.8 0.9 1 1.1 1.2
Relative distance to nucleus

E

Group I   Group II

basement membrane

extracellular region

perivitelline space

cortical actin cytoskeleton

actin filament binding

cell–cell adherens junction

0   2   0   2
Enrichment (log$_2$)

Fig. 5. Simultaneous measurements of 1001 RNA species in single cells by using MERFISH with a 14-bit MHD2 code. (A) The localizations of all detected single molecules in a cell colored based on their
~~measured binary words. (Inset) The composite, false colored fluorescent image of the 14 hybridization~~

Molecular, spatial, and functional single-cell profiling of the hypothalamic preoptic region

Jeffrey R. Moffitt*, Dhananjay Bambah-Mukku*, Stephen W. Eichhorn†, Eric Vaughn†,
Karthik Shekhar, Julio D. Perez, Nimrod D. Rubinstein, Junjie Hao, Aviv Regev,
Catherine Dulac‡§, Xiaowei Zhuang‡§
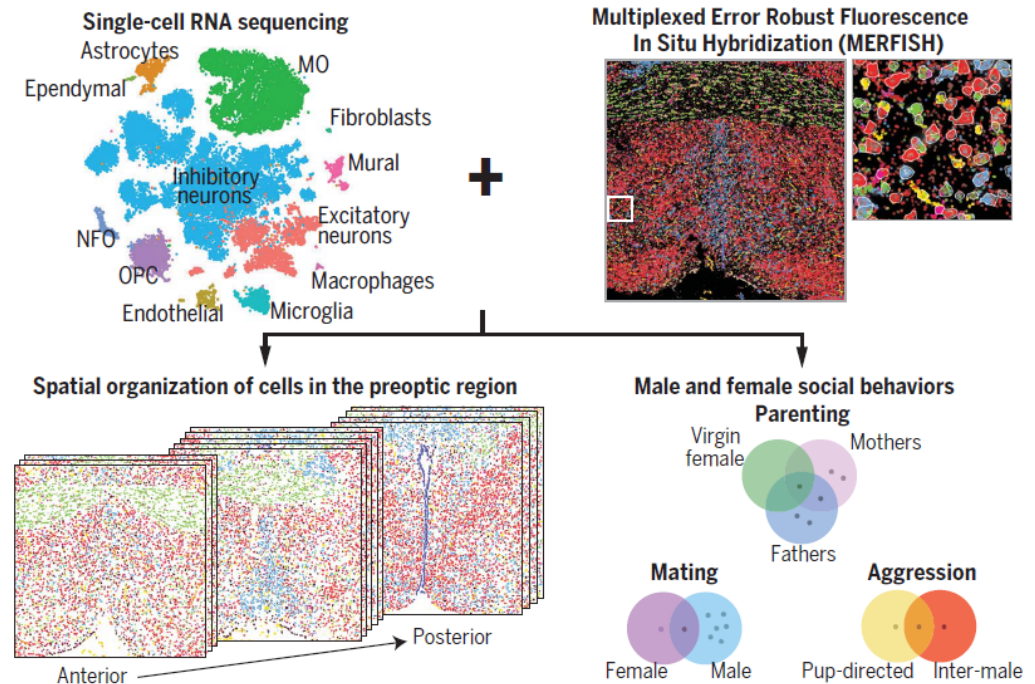
In situ single-cell profiling reveals the molecular and cellular organization of the hypothalamic preoptic region. The combination of MERFISH with scRNA-seq to profile the gene expression of 1 million cells in situ revealed ~70 neuronal populations in the preoptic region, each with distinct molecular signatures and spatial organizations, providing insights into neuromodulatory signaling pathways. Further combination with activity marker imaging led to the identification of discrete neuronal types activated by key social behaviors, including parenting, aggression, and mating.

A

Identification of cells and RNAs

Segmentation co-stains
Somal boundaries

Non-combinatorial sequential FISH
20 genes

Combinatorial smFISH
135 barcoded genes

Gad1 Ttyh2 Aqp4 Myh11
Slc17a6 Pdgfra Selplg Fn1

500 μm

polyA

50 μm

B

Inhibitory neurons Excitatory neurons Mature oligodendrocyte (OD) Immature OD Astrocytes Microglia Ependymal Mural

Genes

Gad1
Slc17a6
Ttyh2
Mbp
Pdgfra
Aqp4
Selplg
Cd24a
Fn1
Myh11

Normalized expression

Cells

C

NFO
Mural Endothelial
Microglia
MO
OPC Inhibitory Ependymal
Excitatory
Astrocyte

tSNE$_2$

tSNE$_1$

D

Correlation

Inhibitory
Excitatory
Mature OD
Immature OD
Astrocyte
Microglia
Ependymal
Endothelial
Mural

MERFISH

Inhibitory Excitatory Mature OD Immature OD Astrocyte Microglia Ependymal Endothelial Mural

scRNAseq

E

Anterior ──────────────────────→ Posterior

0 μm 100 μm 200 μm 300 μm 400 μm 500 μm

All cells

500 μm

400 μm

Inhibitory
Excitatory
Mature OD
Immature OD
Astrocyte
Microglia
Ependymal
Endothelial
Mural

F

0 μm 100 μm 200 μm 300 μm 400 μm 500 μm

500 μm

Inhibitory neurons

0 μm 100 μm 200 μm 300 μm 400 μm 500 μm

Excitatory neurons

MnPO VLPO
Pe PVA
AVPe BNST
VMPO MPN
PaAP

100 μm 400 μm   100 μm 400 μm   100 μm 400 μm   100 μm 400 μm   100 μm 400 μm   100 μm 400 μm

OD Astrocytes Microglia Ependymal Endothelial Mural

Spatial transcriptome profiling by MERFISH reveals subcellular RNA compartmentalization and cell cycle-dependent gene expression

Chenglong Xia[a,b,c,1], Jean Fan[a,b,c,1], George Emanuel[a,b,c,1], Junjie Hao[a,b,c], and Xiaowei Zhuang[a,b,c,2]

[a]Howard Hughes Medical Institute, Harvard University, Cambridge, MA 02138; [b]Department of Chemistry and Chemical Biology, Harvard University, Cambridge, MA 02138; and [c]Department of Physics, Harvard University, Cambridge, MA 02138
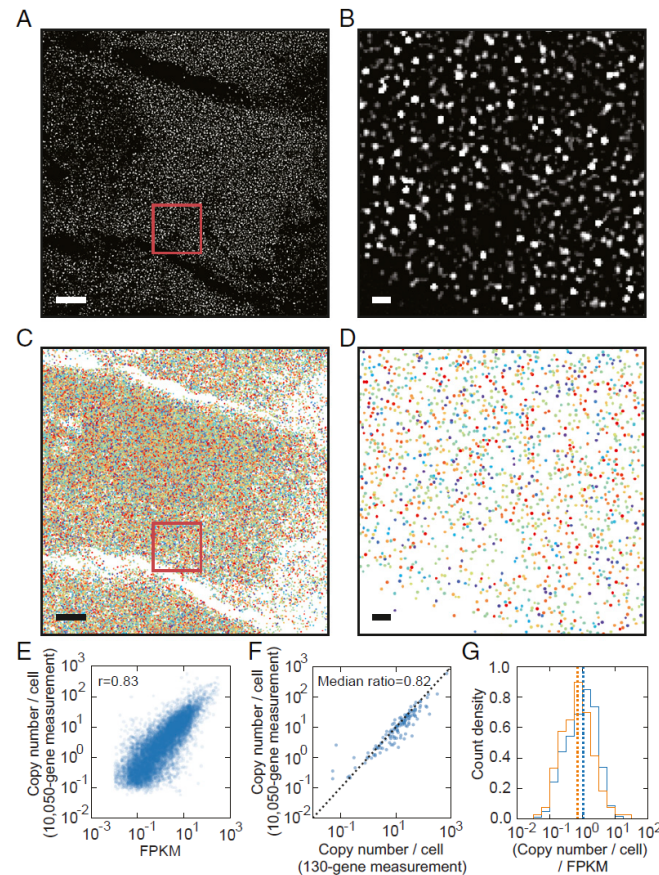
Fig. 1. MERFISH imaging of 10,050 genes in individual U-2 OS cells. (A) A high-pass-filtered, single-z slice, single-bit image of a U-2 OS sample stained with

Multiplexed imaging of high-density libraries of RNAs with MERFISH and expansion microscopy

Transcriptome-scale super-resolved imaging in tissues by RNA seqFISH+

Chee-Huat Linus Eng[1], Michael Lawson[2], Qian Zhu[3], Ruben Dries[3], Noushin Koulena[2], Yodai Takei[2], Jina Yun[2], Christopher Cronin[2], Christoph Karp[2], Guo-Cheng Yuan[3] & Long Cai[2]*

a

b

c

d

647 nm

Sh3bp4
Cuedc2
Kcnd3
Pde8b
Afg3l2
Iqsec2
Fam26e
Shank1
Pcsk4
Ppp2r5d
Cysltr1

561 nm

Tmem109
Dnd1
Sphkap
Gabrq
Tcf7l2
Il27ra
Eps8
Best1
Myo16
Eef1a2
Sh2b3
Tmem196

488 nm

Klhl30
Car10
Slitrk1
Sertm1
Myh10
Fhad1
Peg3
Btbd10
Kcnc2

e

UMAP 2

UMAP 1

GABAergic

Neural stem

Excitatory

Non-neuronal

f

Oligodendrocytes

All RNAs

Kif5a

Astrocytes

All RNAs

Nr4a1

Astrocytes

All RNAs

Gja1

g

Gja1 Eef2

h

Interneuron
Endothelial cells
Astrocytes
Excitatory neuron
Microglia
Astrocytes
Excitatory neuron
Interneuron
Excitatory neuron
Oligodendrocytes
Excitatory neuron
Oligodendrocyte precursor cells

Layer 2/3 ⟶ Layer 6

a

Striatum

Endothelial cells

Astrocytes

Interneuron

Microglia

Ependymal cells

Oligodendrocytes

Choroid plexus

SVZ

b

MCL   IPL   GCL

Astrocytes

Mitral cells

Th^+

Astrocytes

OB

c

GL

Endothelial cells

Tufted cells

Th and *Vgf*

Microglia

Eomes-neuroblast

Th and *Trh*

Olfactory ensheathing cells

OB

d

Th Vgf Trh

Cluster 3

Cluster 1

e

Microglia

Endothelial cell

Tgfb1

Eng
Acvrl1

Tpd52
Mgat1
Hmox1

Gatsl3
Sox13
Kif26a

Ligand   Receptor

f

Cldn5 Selplg   *Tgfb1 Acvrl1*

Microglia

Endothelial

Extended Data Fig. 1 | Clearing and probe-anchoring protocols. a, b, seqFISH+ experiments in NIH/3T3 cells (**a**) and the mouse brain slices (**b**).

Visualization and analysis of gene expression in tissue sections by spatial transcriptomics

A

Surface probe

Cleavage site | Amp and seq handle | Spatial barcode (ID) | UMI | mRNA capture region

Glass slide

Tissue section

ID582 ID583 ID584 ID585 ID586 ID587 ID588 ID589 ID590

B

● *Penk* ● *Doc2g* ● *Kctd12*

Penk *Doc2g* *Kctd12*

E

0 1 2 3 4 5 6
Log2 (norm counts)

MCL | 50-55 µm | 60-150 µm | >150 µm

Doc2g
Slc17a7
Reln
Cdhr1
Sv2b
Shisa3
Plcxd2
Nmb
Uchl1
Rcan2

F

Slc17a7   *Cdhr1*

Sv2b   *Shisa3*

Sampling fraction
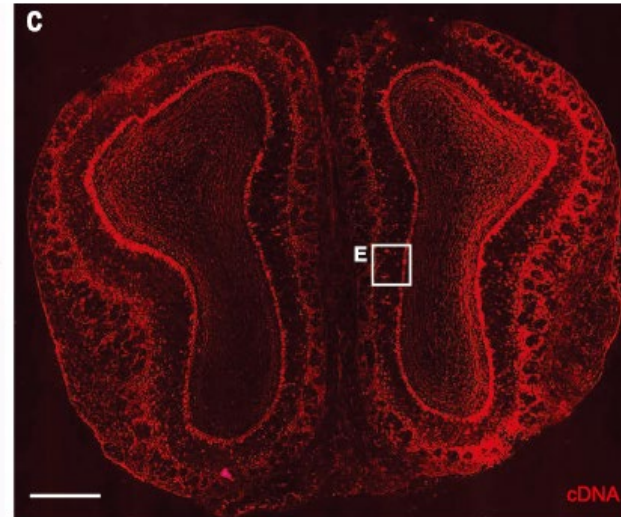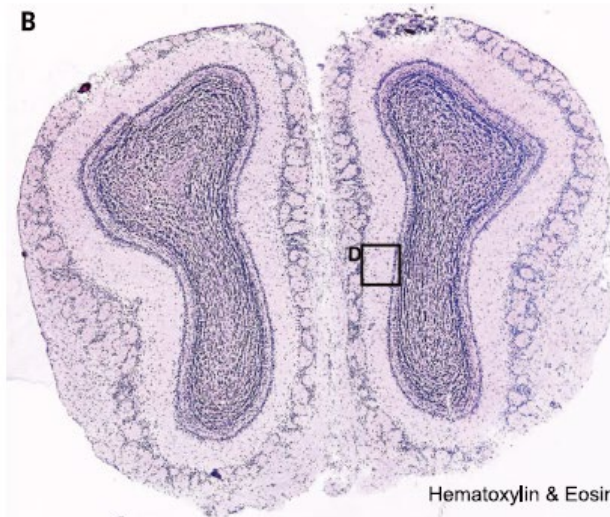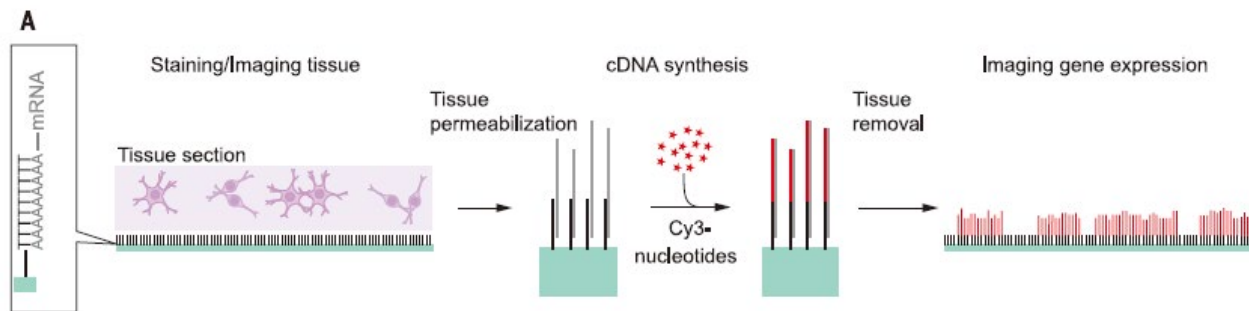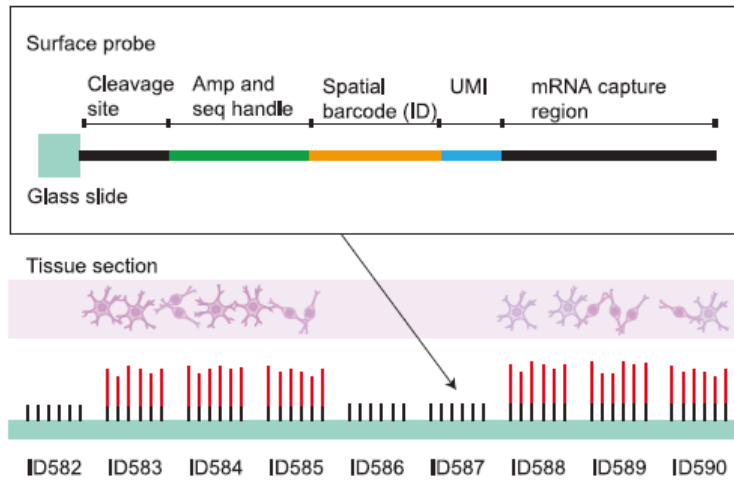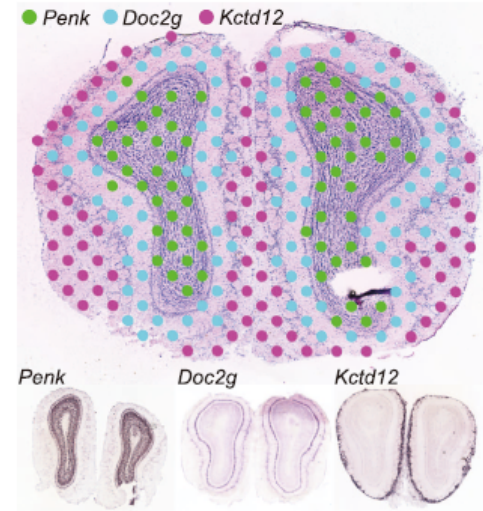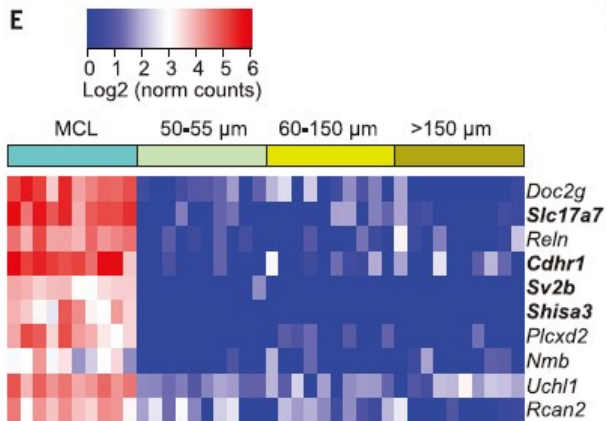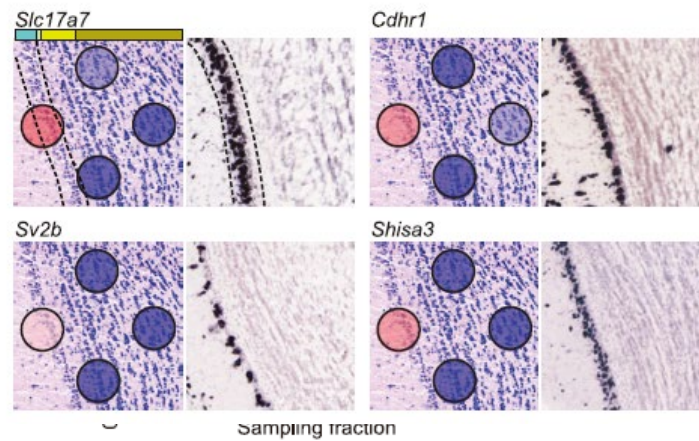
UMI and Barcode

Unique Molecular Identifier (UMI): A UMI is a short, random sequence of nucleotides that is attached to individual mRNA molecules during library preparation for sequencing experiments. The primary purpose of a UMI is to label each original mRNA molecule uniquely, allowing for accurate quantification of gene expression by distinguishing between PCR duplicates and independent molecules originating from the same gene. This helps to correct for PCR bias and improves the overall quality and reliability of the gene expression data.

Barcode: In spatially resolved transcriptomics, a barcode typically refers to a short, known sequence of nucleotides that is used to label transcripts based on their spatial origin within a tissue. Barcodes can be introduced during library preparation or directly on the capture probes or primers used for in situ sequencing or hybridization-based techniques. The primary purpose of a barcode is to enable the assignment of sequenced transcripts back to their original spatial location within the tissue, allowing for the reconstruction of spatial gene expression patterns.

A

α β γ

B Pearson correlation r=0.93

β (log2 (avg norm counts)) vs α (log2 (avg norm counts))

Pcp4, *Actb*, *Nrgn*, *Penk*, *Camk4*, *Rbfox3*, *Pgk1*, *Calb2*, *Rpn2*, *Nrsn1*, *Cck*, *Cdhr1*, *Doc2g*

C Pearson correlation r=0.82

γ (log2 (avg norm counts)) vs α (log2 (avg norm counts))

Nrsn1, *Actb*, *Calb2*, *Cck*, *Cdhr1*, *Doc2g*, *Pgk1*, *Pcp4*, *Rpn2*, *Rbfox3*, *Penk*, *Camk4*, *Nrgn*

D
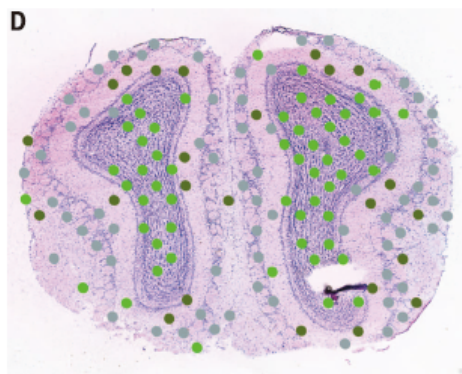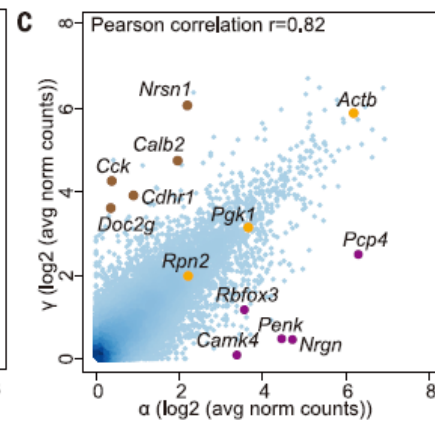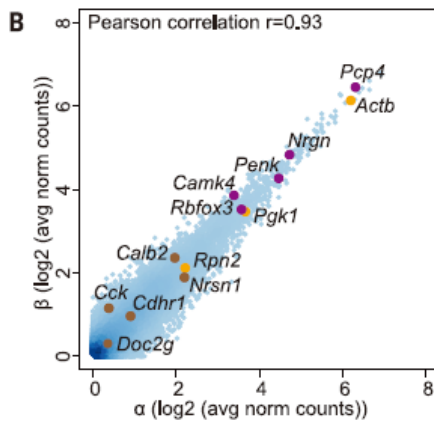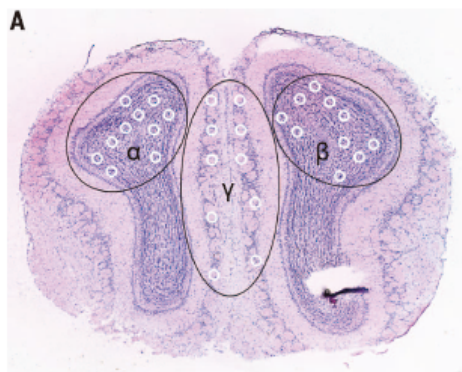
● *Camk4+/Vip–/Th–* ● *Vip+/Camk4–/Th–*
● *Th+/Camk4–/Vip–*

E Pearson correlation r=0.78

Vip+/Camk4–/Th– (log2 (avg norm counts)) vs *Camk4+/Vip–/Th–* (log2 (avg norm counts))

Actb, *Doc2g*, *Cck*, *Pcp4*, *Slc17a7*, *Pgk1*, *Vip*, *Rpn2*, *Shisa3*, *Penk*, *Rbfox3*, *Nrgn*, *Camk4*

F Pearson correlation r=0.76

Th+/Camk4–/Vip– (log2 (avg norm counts)) vs *Camk4+/Vip–/Th–* (log2 (avg norm counts))

Actb, *Nrsn1*, *Calb2*, *Pgk1*, *Pcp4*, *Doc2g*, *Th*, *Eomes*, *Rpn2*, *Penk*, *Rbfox3*, *Nrgn*, *Camk4*
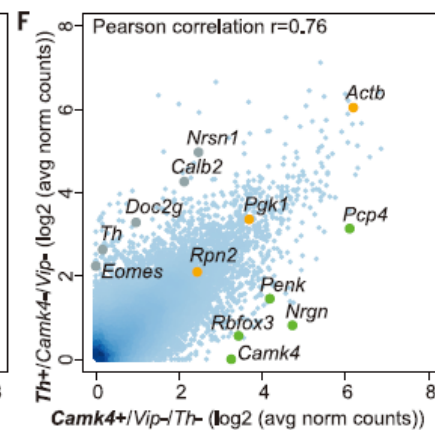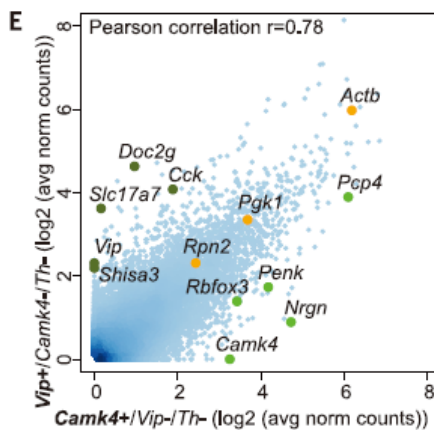
Slide-seq: A scalable technology for measuring genome-wide expression at high spatial resolution

A Bead deposition   *In situ* indexing   10 µm

B   Total time ~ 3 hours

Transfer to tube

Section tissue   RT, tissue digestion   Amplify library

C

- Fibroblast
- Ependymal
- Choroid
- Habenula
- Oligo
- CA1
- DG

Hippocampus

D

Cerebellum   Olfactory bulb

Kidney   Liver

A scRNA-seq → NMF → Cell-type "dictionary" × metagenes → NNLS Slide-seq → Cell-type projections

B Granule   Purkinje   Unipolar Brush

C Cell types per bead   Number of beads

Granule cells
Purkinje neurons
Other inhibitory
Unipolar brush
Golgi
Bergmann
Astrocytes
Oligodendrocytes
Microglia
Endothelial
Choroid plexus
Midbrain

D Ventral / Dorsal / Anterior / Lateral / Anterior / Lateral

E
Dentate
CA3
CA2
CA1
Subiculum
Neurogenesis

CORONAVIRUS

Cryo-EM structure of the 2019-nCoV spike in the prefusion conformation

Daniel Wrapp[1]*, **Nianshuang Wang**[1]*, **Kizzmekia S. Corbett**[2], **Jory A. Goldsmith**[1], **Ching-Lin Hsieh**[1], **Olubukola Abiona**[2], **Barney S. Graham**[2], **Jason S. McLellan**[1]†

A
2019-nCoV S RBD down protomer   2019-nCoV S RBD up protomer   SARS-CoV S RBD up protomer
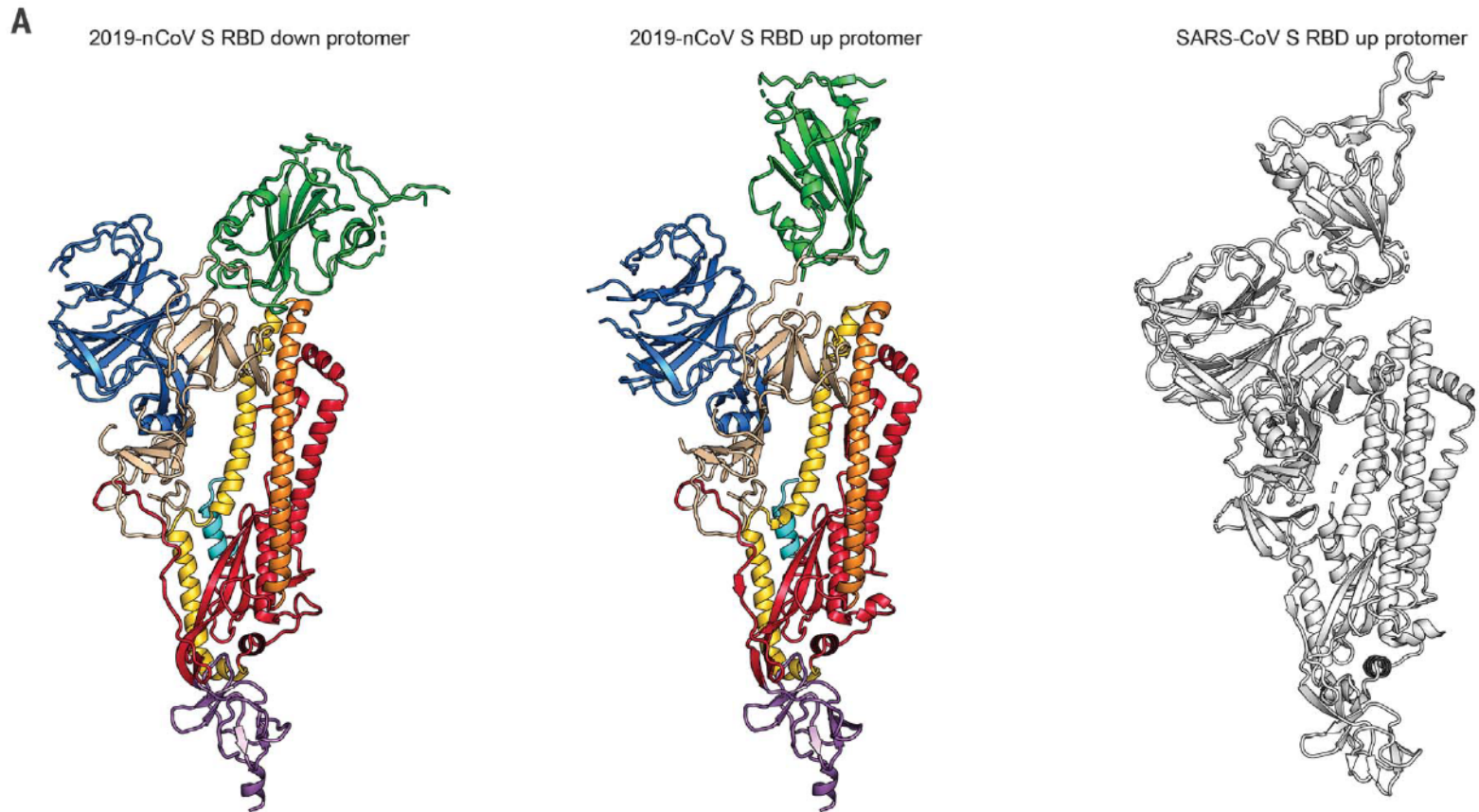
Molecular architecture of the inner ring scaffold of the human nuclear pore complex

Fig. 1. Composite structure of the human NPC. (**A**) Overview of the composite structure of the entire NPC, in which previous structural assignments in the outer rings (9, 13) are represented together with the assignments in the IR that were undertaken in this study (details are shown in fig. S2). Unassigned density is shown in cyan; the nuclear ring is facing up. (**B**) Zoomed-in view of the IR region framed in (A). High-resolution structures (colored ribbons) are shown in the context of the tomographic map (transparent isosurface). (**C**) Conceptual outline of the NPC architecture. Inner (gray) and outer (orange) copies of the Y complex (top and bottom) and the IR core module (middle) are shown in comparison. The configurations of the outer and inner copies of the IR core module are shown enlarged on the right. FG repeat domains can readily reach out into the central channel (F, phenylalanine; G, glycine).
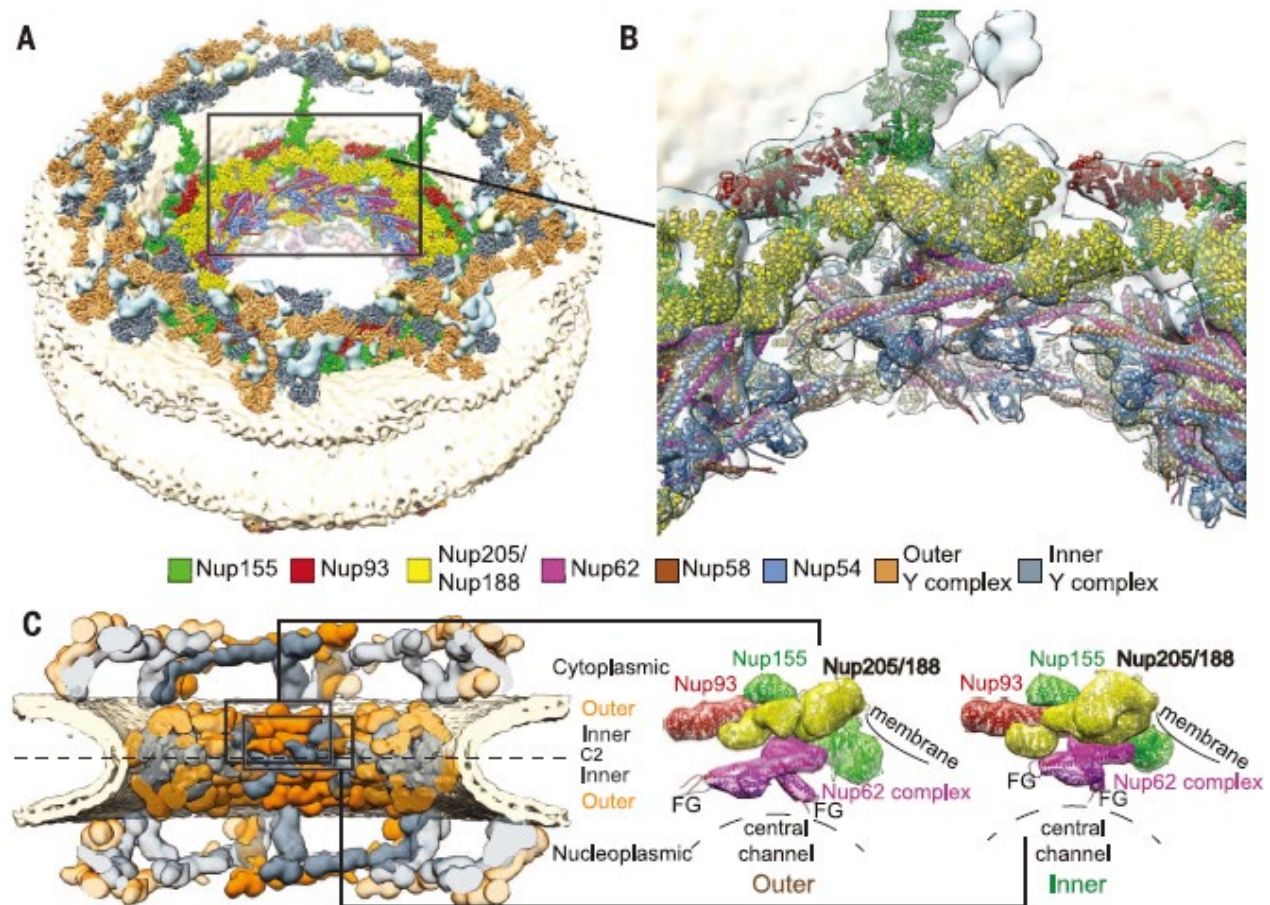
Cryo-electron tomography: The challenge of doing structural biology in situ

Vladan Lučić, Alexander Rigort, and Wolfgang Baumeister

Max-Planck-Institute of Biochemistry, Am Klopferspitz 18, 82152 Martinsried, Germany
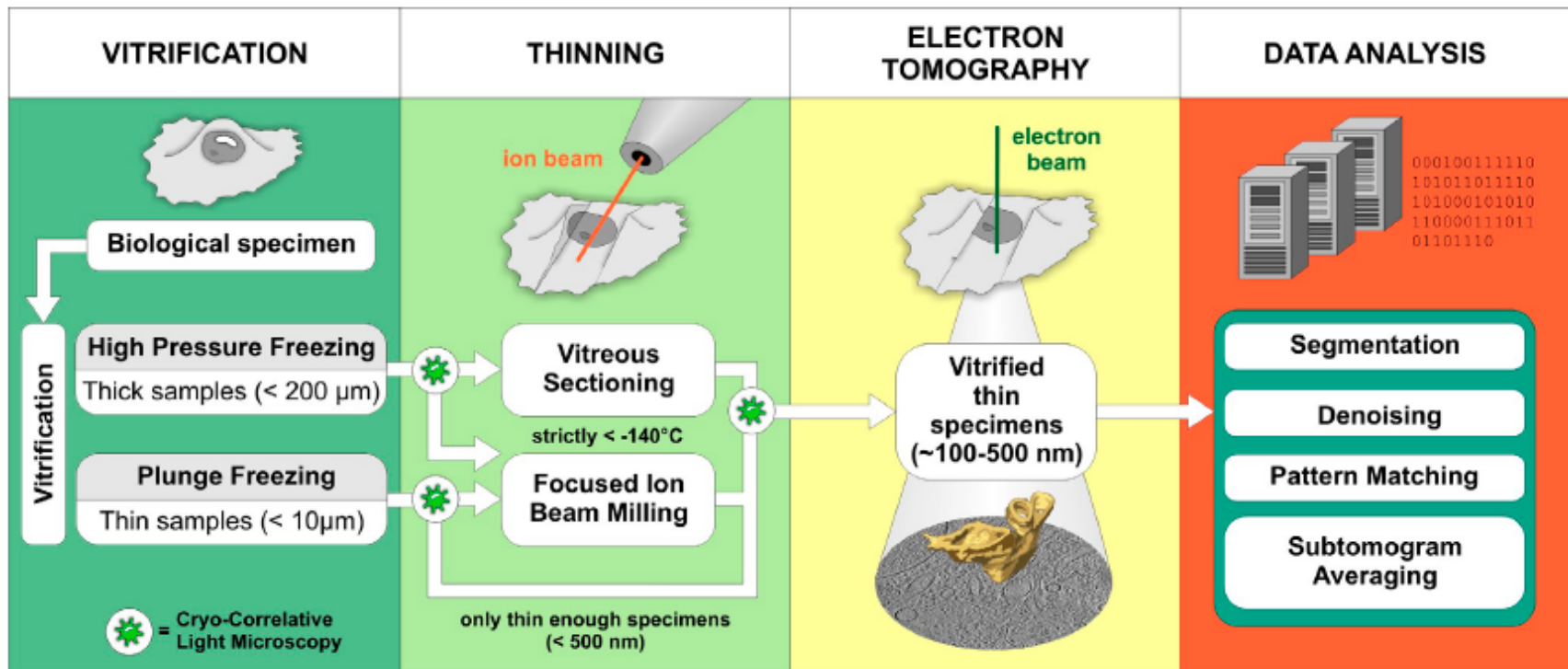
Box 1.   Principles of electron tomography

Electron Imaging

TEM

Phase Plate

Object Plane

Diffraction Plane

Direct Detection

e-

Image Plane

Electron Gun

Illumination System

Computer-controlled Stage

SPECIMEN

Objective Lens

Imaging System

Energy Filter & Camera

Tomography

Electron Beam Directions

OBJECT

Projections
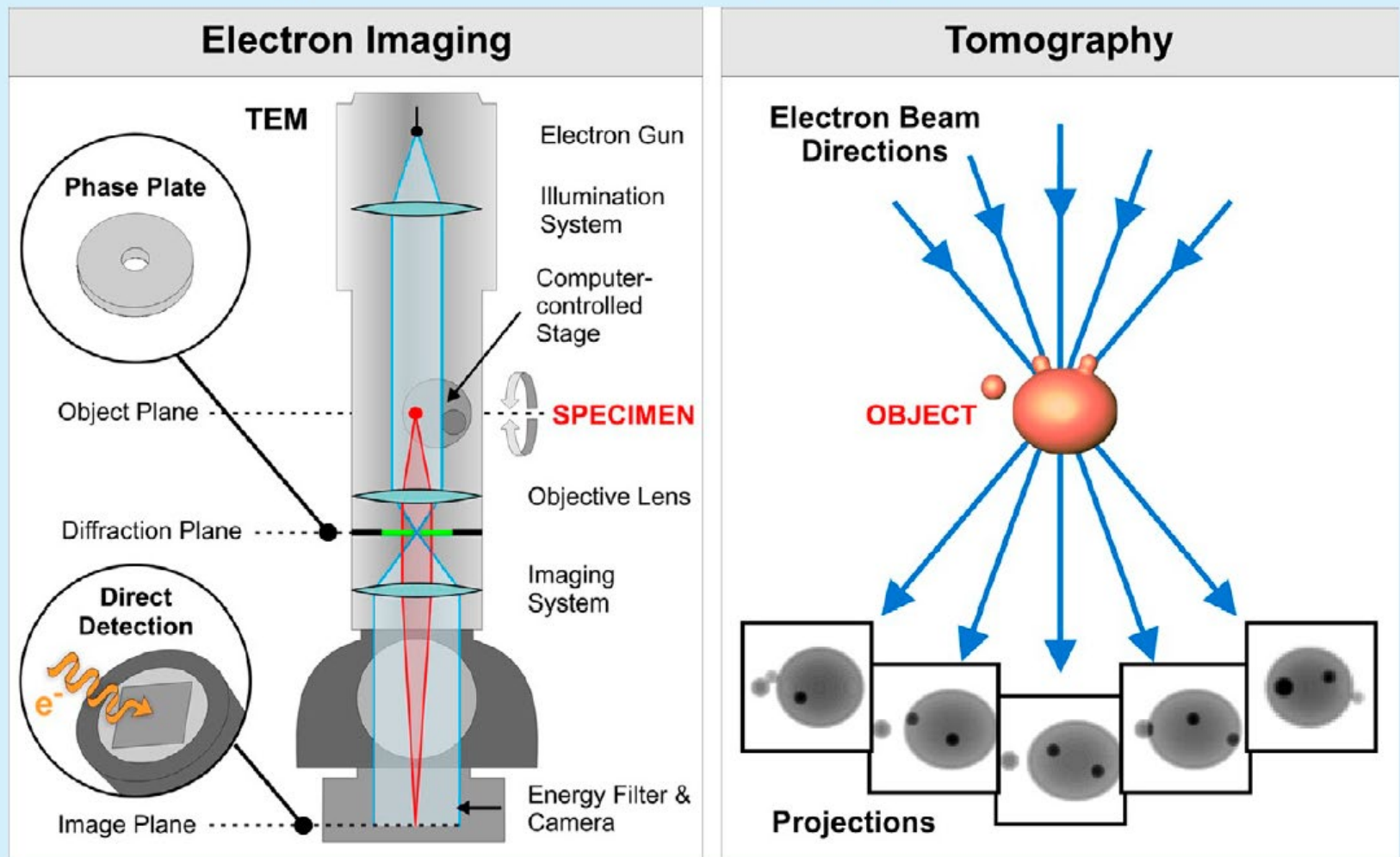
Box 2.   Current technical developments
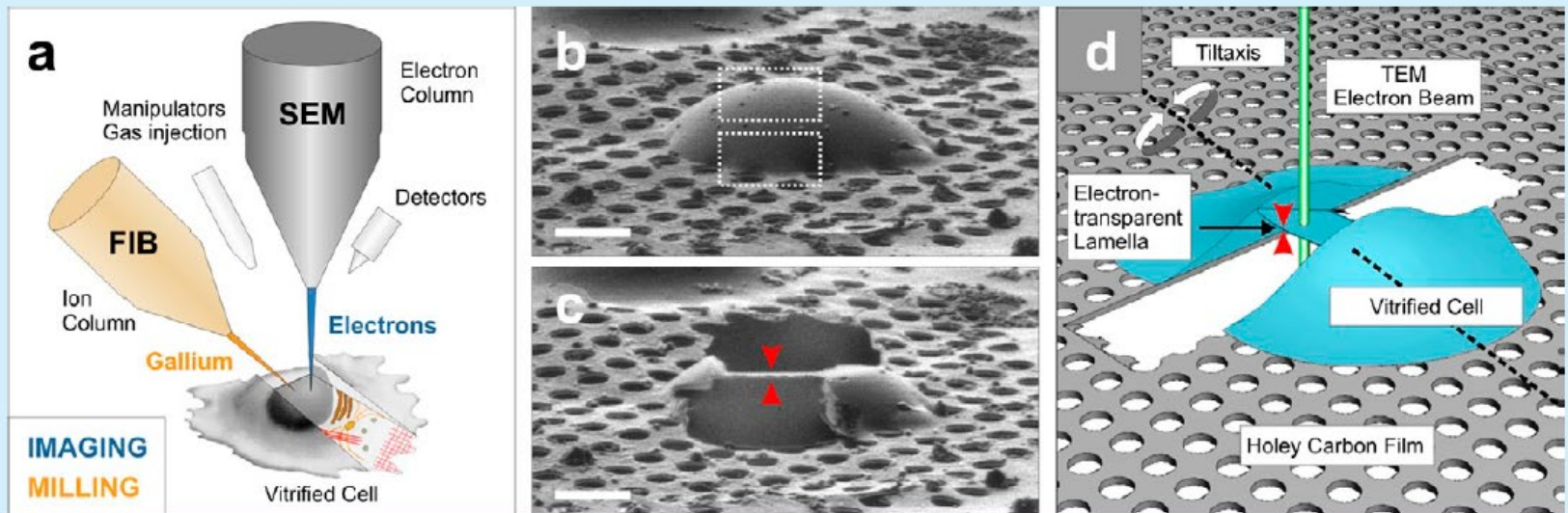
Figure 2. **Cryo-ET of intact cells.** (a) Intact *E. coli*. Top: tomographic slice. Bottom: isosurface representation with positions of template-matched ribosome pairs: om, outer membrane; im, inner membrane; inset shows one ribosome pair (100S). Bar, 200 nm. Modified from Ortiz et al. (2010). (b) *Plasmodium* organelles and the associated cytoskeleton. Top: tomographic slice. Bottom: surface rendering showing plasma membrane (pm, blue), inner membrane complex (imc, yellow), density between pm and imc (red), microtubules (mt, green), apical polar ring (p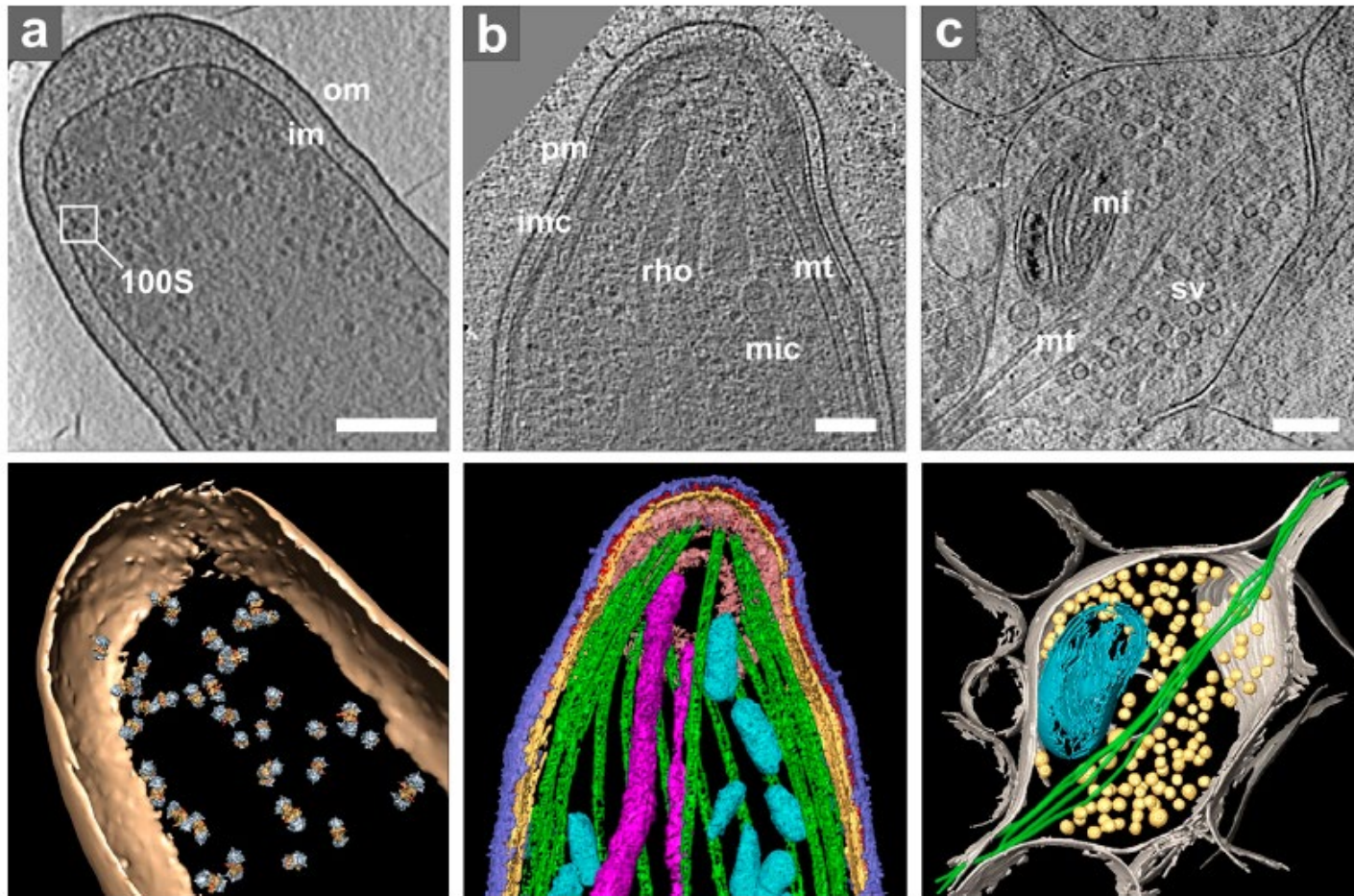ink), rhoptries (rho, violet), and micronemes (mic, cyan). Bar, 100 nm. Reproduced from Kudryashev et al. (2010b). (c) Presynaptic terminal visualized in vitrified dissociated neuronal culture at 15 days in vitro and thinned by FIB milling. Top: tomographic slice (courtesy of Y. Fukuda). Bottom: 3D visualization: plasma membrane (gray), microtubules (mt, green), mitochondrion (mi, cyan), and synaptic vesicles (sv, yellow). Bar, 200 nm.
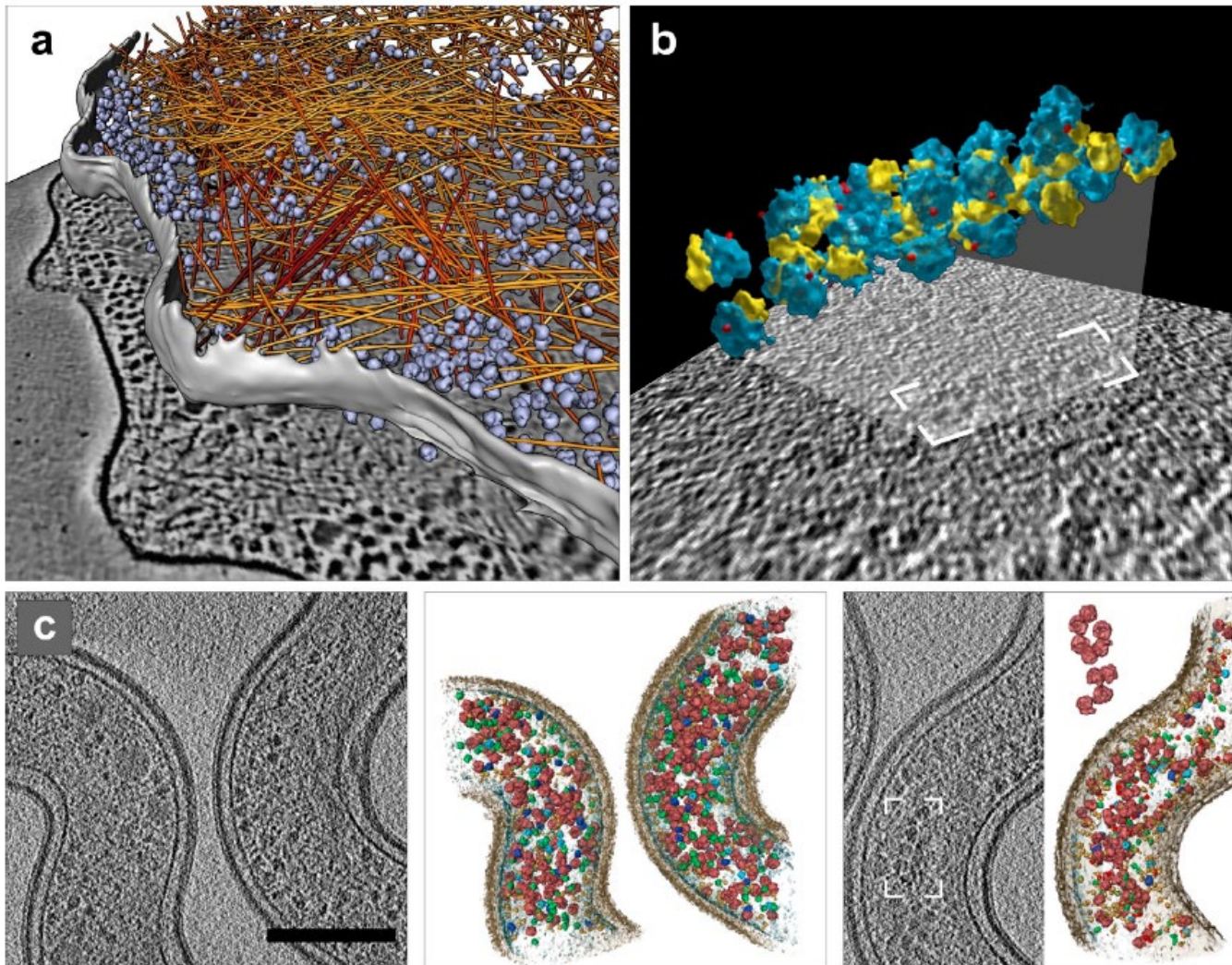
Figure 4. **Image processing: segmentation and template matching.** (a) Automated segmentation of actin filaments in *Dictyostelium discoideum*: actin filaments (yellow to red); ribosomes (blue). Reproduced with permission from Rigort et al. (2012b); copyright Elsevier, Inc. (b) Polyribosomes from intact human glioma cells identified by template matching. Modified with permission from Brandt et al. (2010); copyright Elsevier, Inc. (c) Protein identification using multiple template matching in intact *Leptospira interrogans*. Tomographic slices and 3D visualization of identified proteins of nonstimulated (left) and antibiotics-treated cells (right), ribosomes (red), GroEL (light blue), GroEL/ES (dark blue), and RNA polymerase II (green). Bar, 200 nm. Reprinted by permission from Macmillan Publishers Ltd: *Nature Methods* (Beck et al., 2009); copyright 2009.
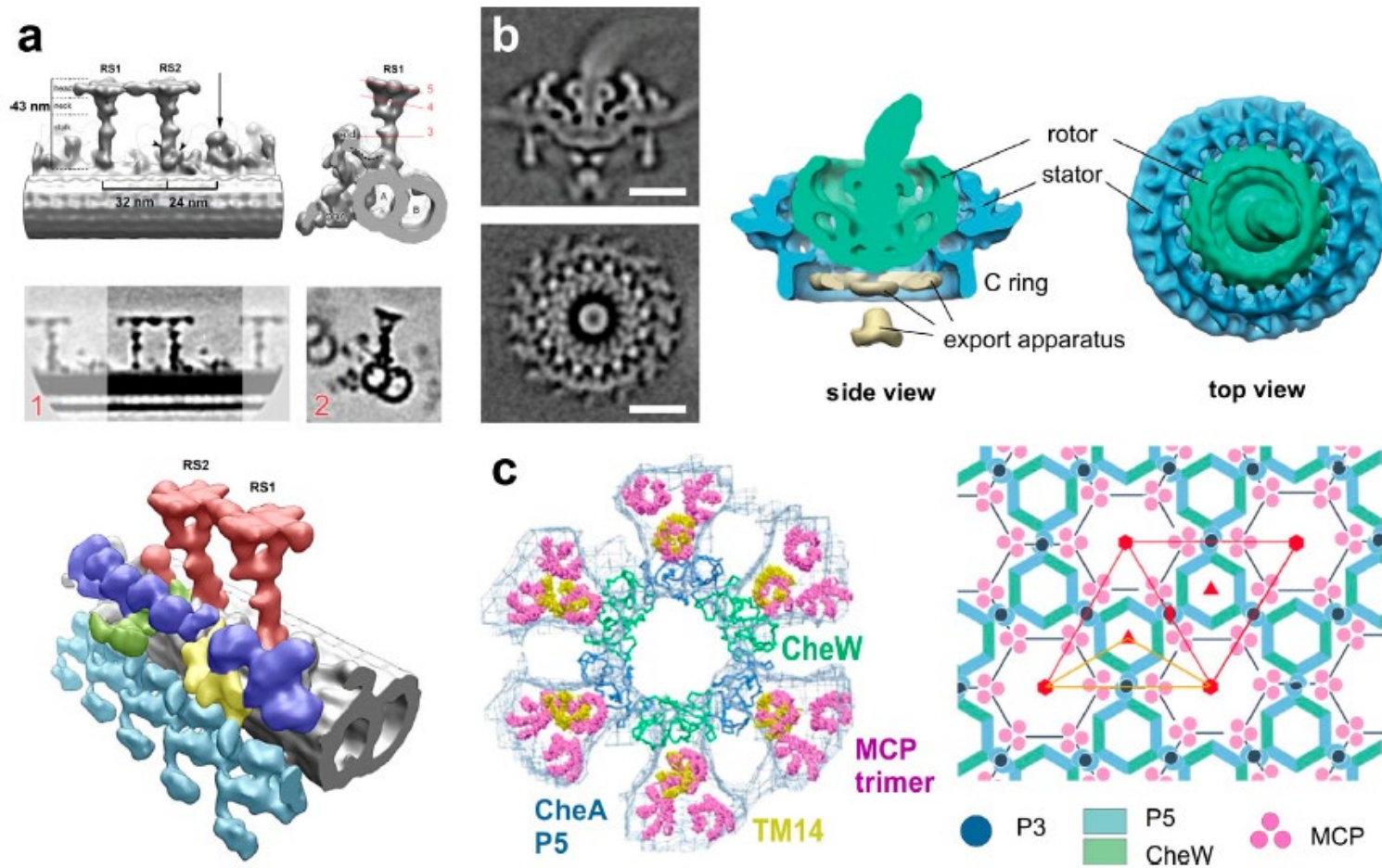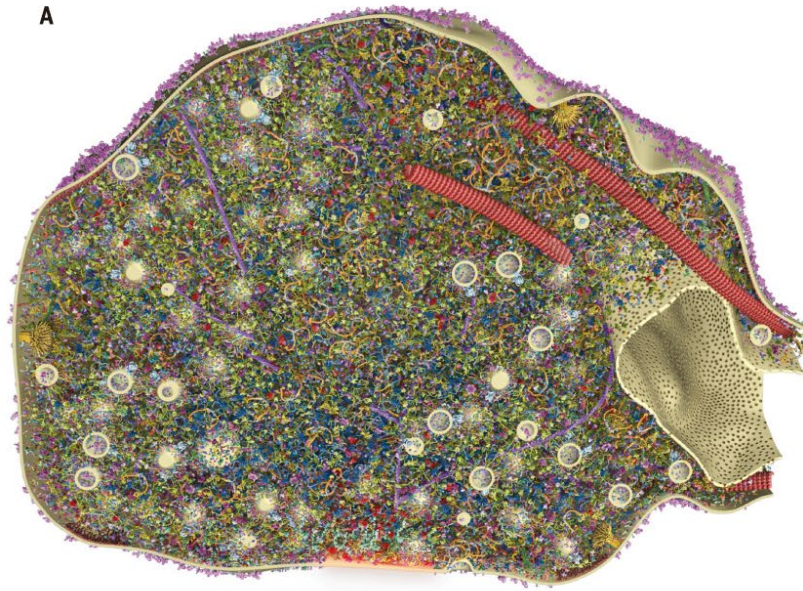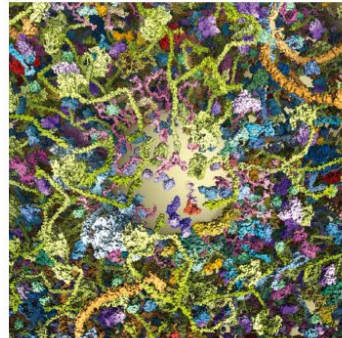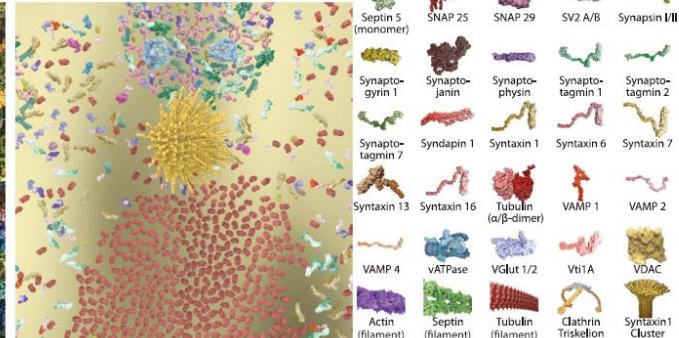
Figure 5. **Image processing: subtomogram averaging.** (a) Isolated *C. reinhardtii* axoneme. Top row: surface renderings of the density map obtained by averaging radial spokes (RS). Middle row: tomographic slices of the above density map. Bottom: surface renderings of the overall 3D structure: microtubule doublet (gray), outer dynein arms (turquoise), inner dynein arms (IDA, blue), the intermediate and light chains of IDAs (yellow), the dynein regulatory complex (green), and the radial spokes (red). RS1, radial spoke 1; RS2, radial spoke 2. Image copyright Pigino et al. (2011). (b) Flagellar motor of intact *Borrelia*. Left: tomographic slices of the averaged density map. Right: 3D isosurface views of the motor. Bars, 25 nm. Reproduced from Liu et al. (2009) with permission from the American Society for Microbiology. (c) Bacterial chemosensory receptors. Left: superposition of one ring of the crystal structure (P5 blue, CheW green) with its six receptor dimers (TM14, yellow) on the EM map (blue mesh) with its previously fit 18 receptor dimers (pink). Right: the arrangement of the receptor array produces P6 point symmetry (red; the asymmetric unit yellow). Image copyright Briegel et al. (2012).

Composition of isolated synaptic boutons reveals the amounts of vesicle trafficking proteins
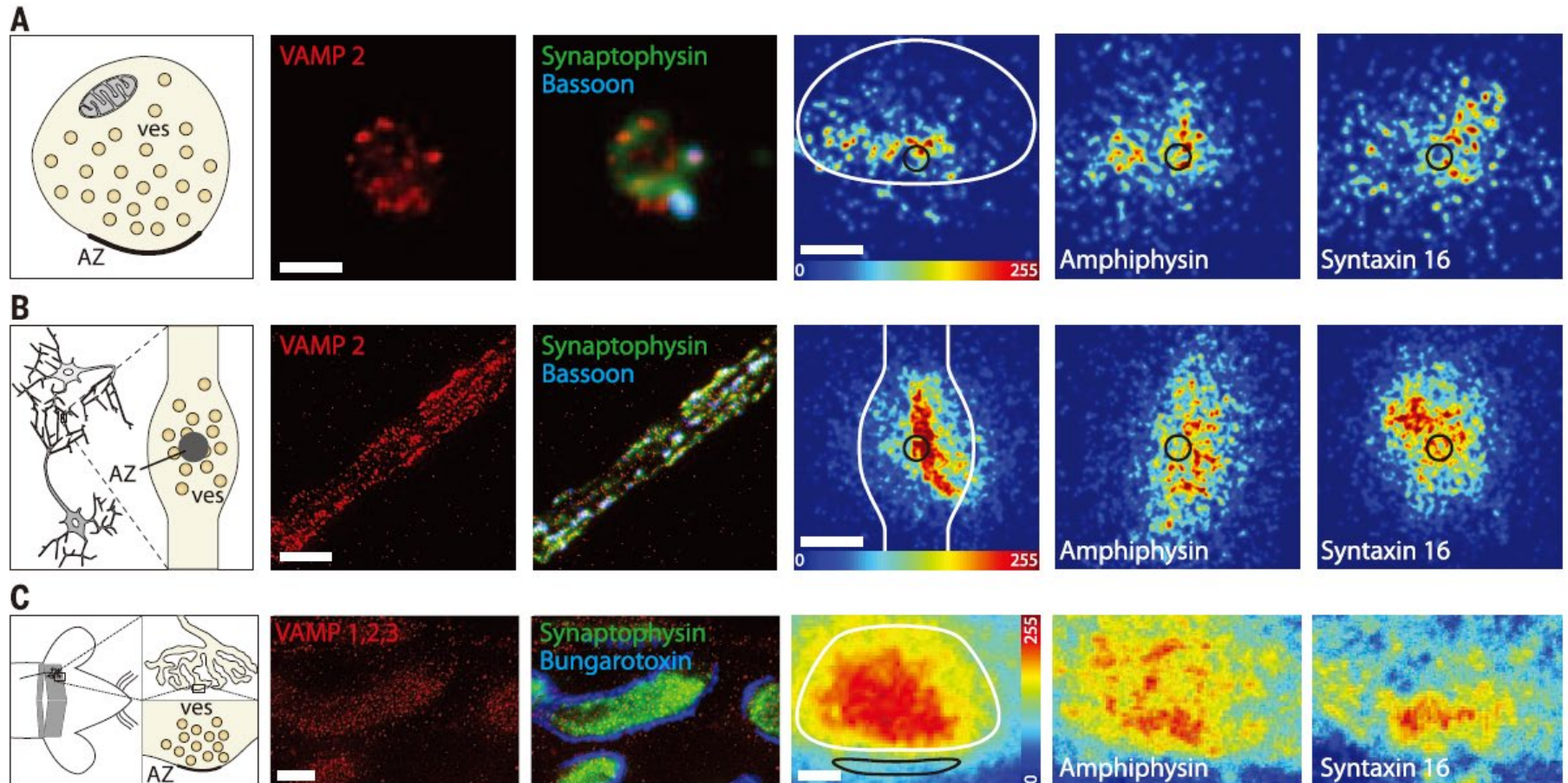
Synaptic vesicle recycling has long served as a model for the general mechanisms of cellular trafficking. We used an integrative approach, combining quantitative immunoblotting and mass spectrometry to determine protein numbers; electron microscopy to measure organelle numbers, sizes, and positions; and super-resolution fluorescence microscopy to localize the proteins. Using these data, we generated a three-dimensional model of an "average" synapse, displaying 300,000 proteins in atomic detail. The copy numbers of proteins involved in the same step of synaptic vesicle recycling correlated closely. In contrast, copy numbers varied over more than three orders of magnitude between steps, from about 150 copies for the endosomal fusion proteins to more than 20,000 for the exocytotic ones.

A

B

C

D

α/β-Synuclein
α-SNAP
Actin (monomer)
Amphiphysin
AP 180

AP 2 (mu2)
APP
β-secretase
Bassoon
Calmodulin

CAPS
Clathrin heavy chain
Clathrin light chain
Complexin 1/2
CSP

Doc2 A/B
Dynamin
Endophilin
Epsin 1
Hsc70

Intersectin 1
Munc13a
Munc18a
NSF
Parvalbumin

Piccolo
PIP-kinase Iγ
Rab3
Rab5
Rab7

Rim 1
SCAMP 1
SGIP1
SGTα
SNAP 23

Septin 5 (monomer)
SNAP 25
SNAP 29
SV2 A/B
Synapsin I/II

Synapto-gyrin 1
Synapto-janin
Synapto-physin
Synapto-tagmin 1
Synapto-tagmin 2

Synapto-tagmin 7
Syndapin 1
Syntaxin 1
Syntaxin 6
Syntaxin 7

Syntaxin 13
Syntaxin 16
Tubulin (α/β-dimer)
VAMP 1
VAMP 2

VAMP 4
vATPase
VGlut 1/2
Vti1A
VDAC

Actin (filament)
Septin (filament)
Tubulin (filament)
Clathrin Triskelion
Syntaxin1 Cluster

SCIENTIFIC REPORTS

3D MALDI Mass Spectrometry Imaging of a Single Cell: Spatial Mapping of Lipids in the Embryonic Development of Zebrafish

Maria Emilia Dueñas [1], Jeffrey J. Essner[3] & Young Jin Lee [1,2]